

---

# A TWO-SCALE SOLVER FOR LINEAR ELASTICITY PROBLEMS IN THE CONTEXT OF PARALLEL MESSAGE PASSING

---

A PREPRINT

**Alexis Salzman\***

Nantes université, Ecole centrale de Nantes,  
GeM Institute, UMR CNRS 6180,  
1 rue de la Noë, 44321, Nantes, France

**Nicolas Moës**

Nantes université, Ecole centrale de Nantes,  
GeM Institute, UMR CNRS 6180  
1 rue de la Noë, 44321, Nantes, France

Institut Universitaire de France (IUF)  
1 rue Descartes, 75231 Paris, France

January 20, 2023

## ABSTRACT

This paper pushes further the intrinsic capabilities of the GFEM<sup>gl</sup> global-local approach introduced initially in [7]. We develop a distributed computing approach using MPI (Message Passing Interface) both for the global and local problems. Regarding local problems, a specific scheduling strategy is introduced. Then, to measure correctly the convergence of the iterative process, we introduce a reference solution that revisits the product of classical and enriched functions. As a consequence, we are able to propose a purely matrix-based implementation of the global-local problem. The distributed approach is then compared to other parallel solvers either direct or iterative with domain decomposition. The comparison addresses the scalability as well as the elapsed time. Numerical examples deal with linear elastic problems: a polynomial exact solution problem, a complex micro-structure, and, finally, a pull-out test (with different crack extent).

## 1 Introduction

Computational methods are addressing more and more complex problems. This paper is concerned with elasticity problems having roughly two-scales. A global scale at the structural level and a local scale representing a micro-structure, a crack or a reinforcement for example. Note that the local scale appears over the whole domain in the case of a micro-structure and only in narrow zones for cracks and reinforcements. A direct finite element approach for these problems is to create a unique mesh and solve. This approach does not take advantage of the two-scale nature. This leads to difficulties: the matrix can have a huge size and can be badly conditioned. Iterative domain decomposition resolution is one way to face huge matrix size (see [30]) but does not solve the conditioning issue unless a specific preconditioner is used. A direct solver can cope with poor conditioning, but matrix size is still an issue.

In order to take into account the two-scale nature of a problem, the first existing global to local method (see for example [23]) use the raw global scale field as a boundary condition for local problems (refined encapsulated meshes), which provide the desired accuracy to the simulation. But since the raw global field does not take into account the local behavior, it does not provide a good boundary condition to the local problems. The GFEM<sup>gl</sup> method, first introduced in [7], adds the idea of local to global interaction via enrichment functions. More precisely, local problems, which can overlap, yield solutions used to build enrichment functions. These functions are used through the partition of unity method to compute at global scale an improved solution. The overlapping aspect of the local problems and their intermixing use in the enriched global problem permit to partially address the boundary condition error of the raw global problem field. In [6] this problem of boundary condition has been addressed by increasing the size of the local problems (the boundary condition at the local scale is pushed far enough) or by increasing the polynomial interpolation order of the global scale problem. But it is in [24] that a more practical and robust solution to this boundary problem

---

\*E-mail address of the corresponding author : alexis.salzman@ec-nantes.fr

has been proposed by introducing iterations between scales. From the raw results, boundary conditions are imposed on the local problems, whose solutions are used as enrichment functions for a new enriched global problem, whose solution is again used as boundary conditions for local problems and finally their solutions reused for a last new enriched global problem.

Later in [26] the idea arises that in evolutionary phenomena such as crack propagation, this GFEM<sup>gl</sup> scale loop can be intertwined with a propagation loop. But it was only in [14] that the two-scale looping strategy was further investigated for a larger number of scale iterations as a remedy for the boundary problem, in a context of a crack propagation step with a single local problem. This work shows that in a few iterations, the GFEM<sup>gl</sup> method provides a significant error reduction at both scales. But, as in many other publication, the way this error is obtained is problematic because it is a relative error based on a known solution for this problem (analytical or numerical fine reference). Another approach to deal with this boundary problem has been studied in more detail in [20] by examining how boundary conditions are imposed at the local scale: Dirichlet, Neumann and Cauchy boundary conditions have been compared, the last one providing a better convergence rate in the treated case (fracture mechanics problems). But in [27] it turned out that the Dirichlet boundary condition was the best in the given context.

The question of how the local problem solution is used to construct an enrichment function is another topic widely studied in the literature. In [4] the SGFEM technique proposes to remove from the fine scale field (obtained here with more conventional analytic functions) its piecewise linear interpolant on the coarse<sup>2</sup>-scale field. This operation ensures a matrix conditioning number for the enriched system equivalent to that of the non enriched system. In [13, 12] the SGFEM technique, mentioned to potentially boost the GFEM<sup>gl</sup> method, was adapted to fracture mechanics with an analytical enrichment function improving both matrix conditioning and result quality.

The GFEM<sup>gl</sup> method has also been successfully evaluated in a nonlinear context [17, 29], in other mechanical domains [28, 11] and even integrated in a commercial software [22]. But since its inception until today, it is its intrinsic parallel capacities that have been put forward by its creators. In [18], since the local problems (one per patch) are independent of each other, they can be solved (with a direct solver) in parallel (in multithreaded paradigm, each thread computes a set of patches). In [27], the authors successfully reused this parallel implementation and addressed, among many aspects, the issue of memory consumption related to local problems. Especially when the scale loop is used to cope with the boundary condition issue, storing the factorization of local problems reduces the cost of iterations, at the price of a significant increase in the memory footprint. In [21] the local problems themselves have been treated with a parallel solver keeping the idea of computing each of them in parallel. This dual level of parallelism was also studied at the same time in [31] (in a message passing context).

In [18, 27, 21] the local problems called "sub-local" domains were constructed from one or a few non-overlapping master local domains, in order to apply the same discretization for all these "sub-local" domains. This artifact greatly simplify the integration process of the enriched macro-scale problem since all its enrichment function share the same discretization in this case, thus the same integration points.

In this paper, the proposed two-scale method retains the idea of a loop between scales to deal with boundary condition problems, but adds the calculation of a new error criterion to terminate this loop at a given accuracy. This criterion is based on the notion of reference solution which introduces a new way to formulate the enrichment function and to create the global problem. Otherwise, to avoid any limitation imposed by computer memory, the proposed two-scale method uses the parallel message passing interface (MPI) paradigm to access distributed memory resources. All the meshes are distributed over the processors, which induces an original scheduling algorithm, described in section 5.2, to optimize the load balancing of the processors at the fine scale. The distributed nature of the mesh at the global scale also leads to a parallel resolution at this scale. Compared to the "sub-local" domain approach, the proposed two-scale method uses the more systematic approach of a local problem per patch while keeping the notion of a single discretization at the fine scale in order to simplify the parallel implementation, the definition of the enrichment functions and the construction of the problem at the global scale. And finally, the chosen boundary conditions imposed on these local problems are of Dirichlet type.

The paper is organized as follows. The next section recalls the classical global-local formulation. Then in section 3, we introduce a reference solution and reformulate the two-scale approach using a pure matrix format. Section 4 studies the issue of scale difference between the global and local level and its impact on performance. Section 5 deals with the parallel global-local approach in which both the global and local problems are distributed. Section 6 deals with the three numerical experiments and the paper ends with conclusion and possible future works.

<sup>2</sup>In this article, the terms "fine" or "micro" are sometimes used instead of the original "local" designation in the GFEM<sup>gl</sup> method. And "coarse" or "macro" are sometimes used instead of "global".

## 2 GFEM<sup>gl</sup> ingredients

### 2.1 Continuous mechanical problem

In this work, we will only consider mechanical elasticity but other fields of application are possible. In the domain of interest  $\Omega$ , a region of  $\mathbb{R}^3$ , the strong form of the equilibrium equation of the mechanical problem is defined as follows:

$$\nabla \cdot \boldsymbol{\sigma} + \mathbf{f} = 0 \quad (1)$$

with  $\mathbf{f}$  being a prescribed volume loading and the stress tensor is  $\boldsymbol{\sigma} = \mathbf{C} : \boldsymbol{\varepsilon}$ ,  $\mathbf{C}$  being the Hook's tensor and  $\boldsymbol{\varepsilon}$  being the strain tensor. The Neumann and Dirichlet conditions applied on the  $\partial\Omega$  boundary of the  $\Omega$  domain are:

$$\boldsymbol{\sigma} \cdot \mathbf{n} = \mathbf{t} \text{ on } \partial\Omega^N, \mathbf{u} = \bar{\mathbf{u}} \text{ on } \partial\Omega^D, \partial\Omega^N \cap \partial\Omega^D = \emptyset \quad (2)$$

where  $\mathbf{t}$  is the prescribed tensile load on the  $\partial\Omega^N$  part of  $\partial\Omega$ ,  $\mathbf{n}$  the outgoing normal vector of  $\Omega$ ,  $\bar{\mathbf{u}}$  the prescribed displacements on the  $\partial\Omega^D$  part of  $\partial\Omega$  and  $\mathbf{u}$  the displacement field. Let  $\mathcal{M}^C$  be the continuous space of the problem defined on  $\Omega$  and compatible with the Dirichlet boundary conditions ( $\mathcal{M}_0^C$  being  $\mathcal{M}^C$  with null Dirichlet boundary conditions). The solution  $\mathbf{u}^C \in \mathcal{M}^C$  of the continuous problem defined by (1) and (2) in their weak form, is given by solving:

$$\forall \mathbf{v}^* \in \mathcal{M}_0^C, A(\mathbf{u}^C, \mathbf{v}^*)_\Omega = B(\mathbf{v}^*)_\Omega, \mathbf{u}^C = \bar{\mathbf{u}} \text{ on } \partial\Omega^D \quad (3)$$

where the bi-linear and linear forms are:

$$\begin{aligned} A(\mathbf{u}, \mathbf{v})_\Omega &= \int_\Omega \boldsymbol{\varepsilon}(\mathbf{u}) : \mathbf{C} : \boldsymbol{\varepsilon}(\mathbf{v}) dV \\ B(\mathbf{v})_\Omega &= \int_{\partial\Omega^N} \mathbf{t} \cdot \mathbf{v} dS - \int_\Omega \mathbf{f} \cdot \mathbf{v} dV \end{aligned} \quad \text{with } \mathbf{u} \in \mathcal{M}^C \text{ and } \mathbf{v} \in \mathcal{M}_0^C \quad (4)$$

and the strain is given by the kinematic equation  $\boldsymbol{\varepsilon}(\mathbf{u}) = \frac{1}{2} (\nabla \mathbf{u} + (\nabla \mathbf{u})^t)$ .

### 2.2 Global problem

To solve (3), the two-scale approach discretizes the continuous problem into two steps. It starts by discretizing  $\Omega$  with a mesh composed of macro (or global or coarse) elements capable of representing the general behavior of the problem. On this global mesh, where  $I^g$  denotes its set of nodes (the superscript g stands for "global scale"), we consider the standard first-order finite element approximation functions  $N^i : \mathbf{x} \in \mathbb{R}^3 \rightarrow N^i(\mathbf{x}) \in [0, 1] \subset \mathbb{R}$ ,  $i \in I^g$ , associated to a coarse scale node  $\mathbf{x}^i$ , with a support given by the union of all finite elements sharing the node  $\mathbf{x}^i$  (this group of macro-elements is called "patch" hereafter). These  $N^i$  are used to linearly interpolate the degrees of freedom (dof), also called values in this work, which represent the classical values of the discretized displacement field at the mesh nodes.

Some nodes of this global mesh are then enriched when their support covers certain local behaviors that must be finely described. Let  $I_e^g \subseteq I^g$  be the set of enriched global nodes ( $\text{card}(I_e^g) \leq \text{card}(I^g)$ ) and the subscript e stands for "enriched". For each node  $p \in I_e^g$  a two-scale enrichment function  $\mathbf{F}^p(\mathbf{x})$  (described in the next section) enriches the classical basis ( $N^i$ ) of the discretization space. The kinematic equation used to describe the discrete global field  $\mathbf{U}$  at a point  $\mathbf{x}$  is then:

$$\mathbf{U}(\mathbf{x}) = \sum_{i \in I^g} N^i(\mathbf{x}) \mathbf{U}^i + \sum_{p \in I_e^g} N^p(\mathbf{x}) \mathbf{E}^p * \mathbf{F}^p(\mathbf{x}) \quad (5)$$

where:

- $\mathbf{U}^i$  is the vector of classical values for the node  $\mathbf{x}^i$
- $\mathbf{E}^i$  is the vector of enriched values for the node  $\mathbf{x}^i$
- $*$  operator is the component by component multiplication of two vectors

Thus (3) becomes to find  $\mathbf{U}^G \in \mathcal{M}^G \subset \mathcal{M}^C$  such that:

$$\forall \mathbf{v}^* \in \mathcal{M}_0^G, A(\mathbf{U}^G, \mathbf{v}^*)_\Omega = B(\mathbf{v}^*)_\Omega, \mathbf{U}^G = \bar{\mathbf{u}} \text{ on } \partial\Omega^D \quad (6)$$

with  $\mathcal{M}^G = \left\{ \mathbf{U}(\mathbf{x}) : \mathbf{U}(\mathbf{x}) = \sum_{i \in I^g} N^i(\mathbf{x}) \mathbf{U}^i + \sum_{p \in I_e^g} N^p(\mathbf{x}) \mathbf{E}^p * \mathbf{F}^p(\mathbf{x}), \mathbf{U}(\mathbf{x}) = \bar{\mathbf{u}}(\mathbf{x}) \text{ for } \mathbf{x} \in \partial\Omega^D \right\}$ . The integration of (6)

using appropriate Gauss quadrature points (see [18] for example) leads to the resolution of a linear system computed with a direct solver. This system is constructed by eliminating the rows of the elementary matrices related to the Dirichlet values and moving the coupling term (columns related to the Dirichlet values) to the right side.

### 2.3 Local problems and enrichment functions

For a node  $p \in I_e^g$ , the two-scale enrichment function  $\mathbf{F}^p(\mathbf{x})$  is constructed numerically using the solution of a micro (or local or fine) problem. This local problem follows the same equations as (1) and (2), and is discretized by a micro-mesh corresponding to the refinement (in a nested manner) of the macro elements of the  $p$  patch. This is the second discretization step of the two-scale method. Considering  $\omega_p$  the region corresponding to the patch  $p$ , the solution of the local problem  $p$  is obtained by finding  $\mathbf{u}^{Q^p} \in \mathcal{M}^{Q^p} \subset \mathcal{M}^C$  such that:

$$\forall \mathbf{v}^* \in \mathcal{M}_0^{Q^p}, A(\mathbf{u}^{Q^p}, \mathbf{v}^*)_{\omega_p} = B(\mathbf{v}^*)_{\omega_p}, \mathbf{u}^{Q^p} = \mathbf{U}^G \text{ on } \partial\omega_p \quad (7)$$

where:

- $\mathbf{U}^G$  is the solution of (6)
- $\mathcal{M}^{Q^p} = \left\{ \mathbf{u}(\mathbf{x}) : \mathbf{u}(\mathbf{x}) = \sum_{m \in I_p^l} n^m(\mathbf{x}) \mathbf{u}^{m^p}, \mathbf{u}(\mathbf{x}) = \mathbf{U}^G(\mathbf{x}) \text{ for } \mathbf{x} \in \partial\omega_p \right\}$
- $I_p^l$  is the set of nodes associated with the fine mesh discretization of  $\omega_p$  (superscript l stands for "local scale")
- $n^m : \mathbf{x} \in \mathbb{R}^3 \rightarrow n^m(\mathbf{x}) \in [0, 1] \subset \mathbb{R}$  is the first order finite element shape function associated to the fine scale node  $\mathbf{x}^m$
- $\mathbf{u}^{m^p}$  is the vector of classical dofs for the node  $\mathbf{x}^m$  corresponding to the fine scale problem  $p$
- $A(\mathbf{u}, \mathbf{v})_{\omega_p} = \int_{\omega_p} \boldsymbol{\varepsilon}(\mathbf{u}) : \mathbf{C} : \boldsymbol{\varepsilon}(\mathbf{v}) dV$  with  $\mathbf{u} \in \mathcal{M}^{Q^p}$  and  $\mathbf{v} \in \mathcal{M}_0^{Q^p}$
- $B(\mathbf{v})_{\omega_p} = \int_{\partial\omega_p \cap \partial\Omega^N} \mathbf{t} \cdot \mathbf{v} dS - \int_{\omega_p} \mathbf{f} \cdot \mathbf{v} dV$  with  $\mathbf{v} \in \mathcal{M}_0^{Q^p}$

Regarding the boundary condition of the fine-scale problems, different approaches have been tested (in particular in [20]), all of them using the global-scale solution for Dirichlet, Neumann or a mix of both. The idea is to impose the global behavior of the problem on the boundary of the fine-scale problems so that the local behaviors that must be finely described can be revealed by the solutions of the fine-scale problems. In this work, the global-scale solution is only imposed by the Dirichlet boundary condition as presented in (7). Note that the boundary conditions at the global scale are inherited at the fine scale. In particular the coarse-scale Dirichlet boundary condition are imposed via  $\mathbf{U}^G$  (since  $\mathbf{U}^G$  is the solution of (6),  $\mathbf{U}^G = \bar{\mathbf{u}}$  on  $\partial\Omega^D$  and  $\mathbf{u}^{Q^p} = \mathbf{U}^G = \bar{\mathbf{u}}$  on  $\partial\omega_p \cap \partial\Omega^D$ ).

The integration of (7) for all  $p$ , using the standard Gauss quadrature points, lead to the construction of  $card(I_e^g)$  linear systems (reduced at assembly by elimination of Dirichlet values). Their resolution can be done in different ways, but, as already indicated in the introduction, in [18] they are solved in parallel using threads. The distribution of patches to threads uses dynamic scheduling: each thread takes a local problem from a list and processes it (with a direct solver) until the list is empty. Kim et al. proved that local problems should be sorted in this list by decreasing cost (calculated a priori with some metric) in order to maintain a good load balance. They also showed that the most expensive local problem limits the number of processes that can be used for a given problem. Beyond this limit, parallel scaling efficiency drops. Section 5 will explain how we go from a multi-thread patch resolution to a full MPI implementation.

When  $\mathbf{u}^{Q^p}$  are available, the two-scale enrichment functions  $\mathbf{F}^p$  can be constructed from them. A first crud approach is to consider that:

$$\forall p \in I_e^g, \forall \mathbf{x} \in \omega_p \mathbf{F}^p(\mathbf{x}) = \mathbf{u}^{Q^p}(\mathbf{x}) \text{ and } \forall \mathbf{x} \notin \omega_p \mathbf{F}^p(\mathbf{x}) = \mathbf{0} \quad (8)$$

This solution can works if the terms of  $N^p(\mathbf{x}) \mathbf{F}^p(\mathbf{x})$  are not too close to  $N^p(\mathbf{x})$ . Otherwise, the created system is badly conditioned because the discretization basis is almost redundant. But in the literature, many authors use the SGFEM technique [4] which removes from  $\mathbf{u}^{Q^p}$  its piecewise linear interpolant over the coarse-scale field:

$$\forall p \in I_e^g, \forall \mathbf{x} \in \omega_p \mathbf{F}^p(\mathbf{x}) = \mathbf{u}^{Q^p}(\mathbf{x}) - \sum_{j \in I_p^g} N^j(\mathbf{x}) \mathbf{u}^{Q^p}(\mathbf{x}^j) \text{ and } \forall \mathbf{x} \notin \omega_p \mathbf{F}^p(\mathbf{x}) = \mathbf{0} \quad (9)$$

where  $I_p^g$  is the set of macro-scale nodes associated with patch  $p$ . Eliminating the projection first removes from the enrichment function the part that can be represented by the coarse-scale discretization and thus improves the matrix conditioning of the coarse-scale problem. Second, it forces the enrichment function to be zero at coarse-scale nodes



location, which helps solve the blending<sup>3</sup> element problem and also greatly simplifies<sup>4</sup> the application of the global Dirichlet boundary conditions, if any, on those enriched nodes. In this work, a rather different approach is proposed, as presented in the section 3.8.

## 2.4 The scale loop

The main idea of the two-scale solver is to iteratively solve the two types of problems: the global problem (6) and the set of micro problems (7) over patches solved independently. The global and fine problems are linked together. The fine problems over the patches deliver the enrichment functions which are used in the global problem. The global problem delivers the boundary conditions for the patches.

The initial step of the two-scale loop is a key element of the method. In general, a global-scale solution is used as the starting point of the loop (it provides a boundary condition for fine scale problems). This solution can be the result of a global-scale problem without enrichment or the result of a previous computation. In particular, when evolutionary phenomena are involved, the two-scale solver can effectively take advantage of using the last solution found (from the previous evolutionary step) as the starting solution of the two-scale loop used for the current evolution step. Some test cases in the section 6 illustrate this point.

In any case, all the fine-scale problems are mainly handled during this initialization phase. The integration of (7) yields a set of linear system which have constant matrices and partially constant right-hand side vectors during iterations. Only the Dirichlet coupling term changes right-hand side vector during the loop as  $U^G$  varies. Thus, the linear systems matrices and constant right-hand side vectors are created only once during the initialization. And by choosing a direct solver to solve systems, we can also compute the matrix factorization only once. If preserved (which has an impact on memory, as shown in [27]), these factorizations can be reused for backward/forward resolution of fine-scale problems in the remaining steps of the two-scale loop.

## 3 The proposed two-scale method: Matrix-based resolution with a reference target

### 3.1 Overview

Based on the ingredients of the section 2, the figure 1 illustrates in 2D, but the same principle applies in 3D, the general concept of the proposed two-scale method with a fictitious problem on a  $\Omega$  region. Figure 1a shows the discretization of the global scale problem with its boundary conditions. The magenta area is a simple visual effect to show the position of the local behavior to be captured. This area is just a visual artifact where the mesh needs to be refined to appropriately simulate a crack, a specific material inclusion, a damaged material, a rivet, ... All macro nodes for which a macro element of their support has been refined are enriched (figure 1b where red and green dots form the  $I_e^S$  set introduced in the section 2.2). Their enrichment functions are obtained from the solutions of the fine-scale problems associated with their patches (figure 1f where global and local boundary condition are imposed,  $u_d^p$  being introduced in the section 3.5 and defined precisely in F). The union of all the elements of the enriched patches (yellow + orange in the figure 1c) is called the super-patch, noted SP thereafter. Conversely, the set of macro-element that are not part of the SP (shaded in the figure 1c) will be noted as NSP in what follows. One of the goals of the super-patch is to impose a single fine mesh discretization for all fine-scale problems. More precisely, the idea is to impose a fine discretization for all patches covering the local behavior to be captured. Thus their union (in orange on the figure 1c) is the starting mesh of the adaptation strategy described in C (see this appendix for details on how the elements are cut/split/refined) which guarantees that all the elements of this area are at least split once and that the local behavior is well refined (figure 1d). Using only orange elements prevents the refinement of any other element, in order to respect the "one hanging node per edge" rule (avoiding the enrichment of more nodes). The yellow part of the SP is then the set of macro elements not refined and therefore used without modification at the fine-scale level. Thus, in the SP, at the boundary between two macro-elements, the micro-meshes are either compatible or leave hanging nodes (visible in figure 1e and presented in section 3.2). This unified discretization imposed in the SP, allows to process all quantities related to fine-scale grid (integration at Gauss point, level set, damage, mapping, ... ) only once. In this work, the union of the SP refined mesh and the NSP macro-elements (which naturally connect to the yellow fine scale grid elements) is called the reference mesh (figure 1e). It represented a new vision of what the GFEM<sup>gl</sup> method intends to discretize at the local and global level alternatively. The section 3.2 will detail the problem associated with this mesh.

<sup>3</sup>Blending appears in a coarse level element when all its classical dofs are not enriched.

<sup>4</sup>With a non-zero enrichment function, imposing a Dirichlet condition on an enriched node adds the complexity of setting up an equation linking the classical and enriched dofs.

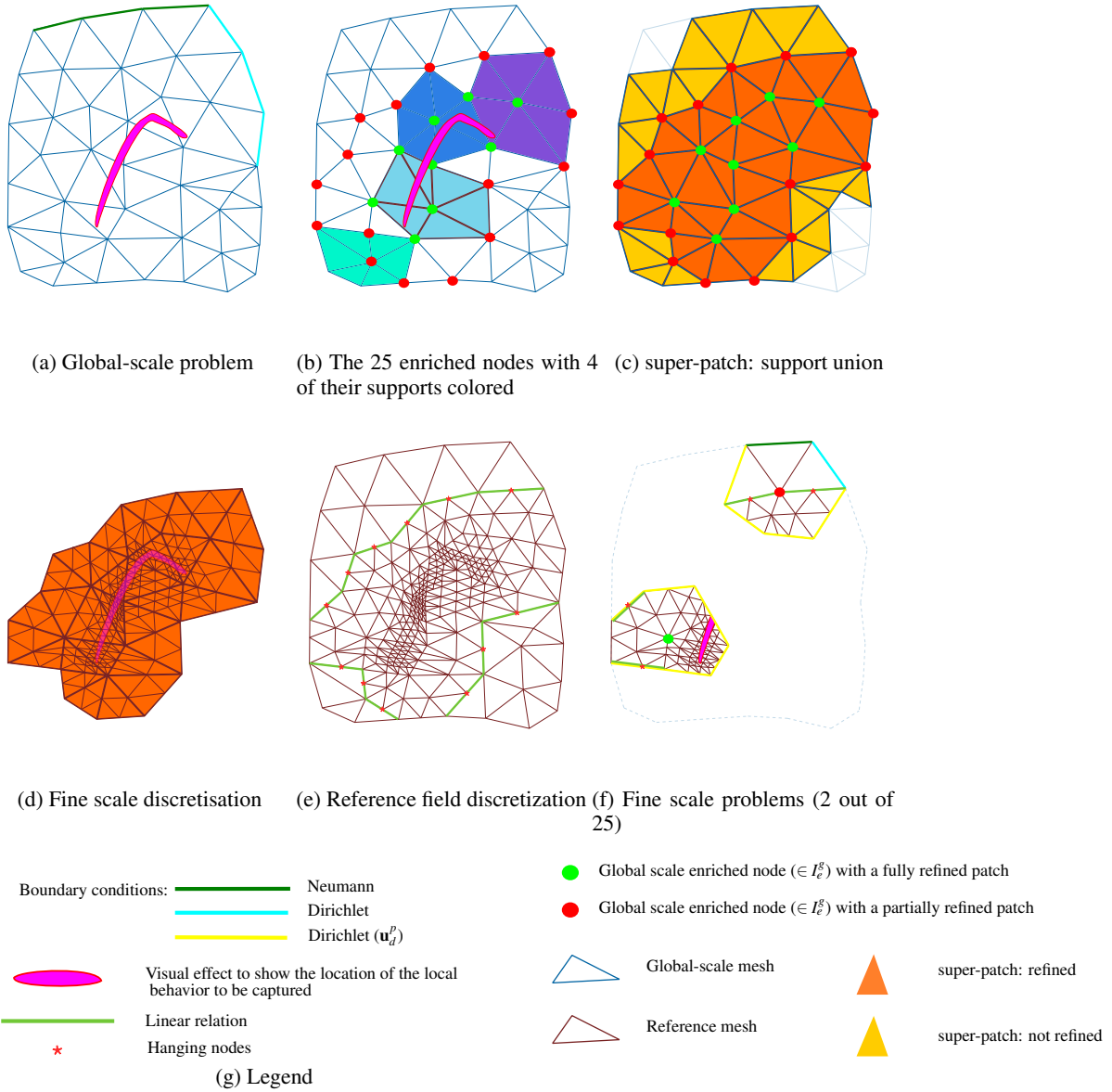


Figure 1: Two-scale method presented in a fictitious 2D problem (for sake of visibility fine-scale mesh is not refined as it should)

A rich naming convention is implemented in B to clarify the different discretizations and the status of the values involved in the different problems solved by the two-scale solver. Thus, all subscribe letters appearing in the matrix or vector in the following algorithms or discussions come from the table 1.

The general scheme of this new two-scale version is given by the algorithm 1. After an initialization step, the alternate resolution between scales starts with the MICRO-SCALE\_RESOLUTION procedure (algorithm F.5) which computes the solutions of fine-scale problems. These solutions are used by the UPDATE\_MACRO.PRB procedure (algorithm F.3) to update the linear system at the global-scale ( $\mathbf{A}_{gg}$  and  $\mathbf{B}_g$ ). Then, a conventional solver ( $\dagger$  in the algorithm 1 described in section 5.1) solves the problem at the global-scale. The global scale solution ( $\mathbf{U}_g$ ) is then transferred to the fine scale by the UPDATE\_MICRO.DOFS procedure (algorithm F.4). Compare to the classical GFEM<sup>gl</sup> version, the scale loop is now controlled by the computation of a *resi* criterion (COMPUTE\_RESIDUAL procedure described by the algorithm F.6) which stops the iterations when it is lower than a threshold ( $\epsilon$ ) given by the user. This convergence check is an important contribution because it allows to evaluate the two-scale solver and to easily compare different

**Algorithm 1** Two-scale algorithm: general procedure. Procedures INIT, UPDATE\_MACRO\_PRB, UPDATE\_MICRO\_DOFS, MICRO-SCALE\_RESOLUTION and COMPUTE\_RESIDUAL are respectively depicted in algorithm F.2, F.3, F.4, F.5 and F.6 of F. The  $\varepsilon$  value is the user-defined target accuracy that the criterion given in the equation (14) must meet to end the scaling loop. See A for notation convention : subscripted letters, superscript patches,  $\triangleright$ , ...

---

```

Create  $\mathbf{U}_g^0$  macro-scale dofs  $\triangleright$ 
 $(\mathbf{A}_{gg}^{ini}, \mathbf{B}_g^{ini}, \mathbf{A}_{FF}, \mathbf{B}_F, \|\mathbf{B}_r\|, \mathbf{A}_{qq}^{patches}, \mathbf{B}_q^{patches}, \mathbf{D}_{qd}^{patches}) \leftarrow \text{INIT}$   $\triangleright$ 
Retrieve macro-scale classical dofs to initialize  $\mathbf{U}_g$  (enriched dof set to zero)
 $\mathbf{u}_F \leftarrow \text{UPDATE\_MICRO\_DOFS}(\mathbf{U}_g)$ 
repeat
   $\mathbf{u}_q^{patches} \leftarrow \text{MICRO-SCALE\_RESOLUTION}(\mathbf{u}_F, \mathbf{A}_{qq}^{patches}, \mathbf{B}_q^{patches}, \mathbf{D}_{qd}^{patches})$   $\triangleright$ 
   $(\mathbf{A}_{gg}, \mathbf{B}_g) \leftarrow \text{UPDATE\_MACRO\_PRB}(\mathbf{A}_{gg}^{ini}, \mathbf{B}_g^{ini}, \mathbf{u}_q^{patches})$ 
   $\mathbf{U}_g \leftarrow \mathbf{A}_{gg}^{-1} \cdot \mathbf{B}_g$   $\dagger$   $\triangleright$ 
   $\mathbf{u}_F \leftarrow \text{UPDATE\_MICRO\_DOFS}(\mathbf{U}_g)$ 
   $resi \leftarrow \text{COMPUTE\_RESIDUAL}(\mathbf{u}_F, \mathbf{A}_{FF}, \mathbf{B}_F, \|\mathbf{B}_r\|)$   $\triangleright$ 
until  $resi < \varepsilon$ 

```

---

version of it. This criterion is introduced in section 3.2 and its computation is given in section 3.7. The following subsections present in more detail the algorithm 1 and the associated procedures without focusing too much on the parallelism which will be discussed in section 5 (only the presence of the symbol  $\triangleright$ , on the right of a line of the algorithm, indicates that a certain communication between the processes exists for this step.).

### 3.2 The reference field and its associated criterion

The reference field  $\mathbf{u}^R$  is the solution of the problem defined by (1) and (2), and discretized by the reference mesh (figure 1e). Solving this reference problem is to find  $\mathbf{u}^R \in \mathcal{M}^R \subset \mathcal{M}^C$  such that:

$$\forall \mathbf{v}^* \in \mathcal{M}_0^R, A(\mathbf{u}^R, \mathbf{v}^*)_{\Omega} = B(\mathbf{v}^*)_{\Omega}, \mathbf{u}^R = \bar{\mathbf{u}} \text{ on } \partial\Omega^D, \quad (10)$$

where:

- $\mathcal{M}^R = \left\{ \mathbf{u}(\mathbf{x}) : \mathbf{u}(\mathbf{x}) = \sum_{k \in I^l} N^k(\mathbf{x}) \mathbf{u}^k, \mathbf{u}(\mathbf{x}) = \bar{\mathbf{u}}(\mathbf{x}) \text{ for } \mathbf{x} \in \partial\Omega^D \right\}$
- $I^l$  is the set of nodes associated with the reference mesh, discretization of  $\Omega$
- $N^k$  is either  $n^k$  or  $N^k$  corresponding respectively to the shape functions defined in 7 or in 6 depending on whether  $\mathbf{x}$  is in a micro or macro element.
- $\mathbf{u}^k$  is the vector of classical dofs for the node  $\mathbf{x}^k$

This solution  $\mathbf{u}^R$  represents the continuous field solution  $\mathbf{u}^C$  only polluted by the discretization error. The standard Gauss quadrature integration of (10) gives the following linear system without Dirichlet elimination:

$$\mathbf{A}_{RR} \cdot \mathbf{u}_R^R = \mathbf{B}_R \text{ with } \mathbf{u}_R^R \text{ the vector of } \text{card}(R) \text{ values defining } \mathbf{u}^R \quad (11)$$

As already mentioned in the section 3.1, in the reference mesh there are hanging nodes between the refined and unrefined areas (visible in figure 1e) that need to be fixed to avoid discontinuity of the  $\mathbf{u}^R$  field. A simple approach is to eliminate them from the system (11) by using a linear relationship to fix their value using the following formula:

$$\text{For an hanging node } \mathbf{x}^j, \mathbf{u}^j = \sum_{i \in I_j} N^i(\mathbf{x}^j) \mathbf{u}^i \quad (12)$$

where:

- $\mathbf{u}^j$  is the vector of fixed values (L-set) for the node  $\mathbf{x}^j$
- $\mathbf{u}^i$  is the vector of free values (f-set) for the node  $\mathbf{x}^i$
- $I_j$  is the set of nodes corresponding to the vertices of the edge or face on which hanging node  $\mathbf{x}^j$  is located. Thus  $\text{card}(I_j) \in \{2, 3\}$ .

- $N^i(\mathbf{x})$  is the standard first-order finite element approximation function associated with the  $\mathbf{x}^i$  node, related to the coarse element support that holds the edge or face where hanging node is present.

Eliminating the linear relations (12) and the Dirichlet boundary condition of (11) leads to the system:

$$\mathbf{A}_{rr} \cdot \mathbf{u}_r^R = \mathbf{B}_r \quad (13)$$

The solution given by a direct solver of this system is  $\mathbf{u}_r^R$  the vector of  $card(r)$  dofs defining  $\mathbf{u}^R$ . But in this work, this system is never solved directly. Instead, the proposed two-scale solver, at each scale iteration, computes a solution  $\mathbf{u}^{ts}$  ( $\mathbf{u}^{ts} \in \mathcal{M}^R$ ) such that it quickly converges to the reference solution  $\mathbf{u}^R$ .

In this work, a *resi* criterion is proposed to control this convergence. The *resi* criterion is taken as the relative residual error of system (13):

$$resi = \frac{\|\mathbf{A}_{rr} \cdot \mathbf{u}_r^{ts} - \mathbf{B}_r\|}{\|\mathbf{B}_r\|} \quad (14)$$

where  $\|\cdot\|$  is the L2-norm and  $\mathbf{u}_r^{ts}$  is the vector of  $card(r)$  dofs corresponding to the  $\mathbf{u}^{ts}$  solution obtained by the two-scale solver. For simplicity, in what follows,  $\mathbf{u}_r$  will represent the  $\mathbf{u}_r^{ts}$  vector of the field  $\mathbf{u}^{ts}$  where superscripts *ts* is made implicit. The question of computing (14) is exposed in the following section.

To relate this criterion to an energy error, an energy norm is defined as follows using (4):

$$\|\mathbf{u}\|_{E_\Omega} = \sqrt{A(\mathbf{u}, \mathbf{u})_\Omega} = \sqrt{\int_\Omega \boldsymbol{\varepsilon}(\mathbf{u}) : \mathbf{C} : \boldsymbol{\varepsilon}(\mathbf{u}) d\Omega} \quad (15)$$

The error introduced by the two-scale solver (mainly on the boundary conditions imposed on the fine scale problems) in the indirect resolution of system 13 compare to its direct resolution can thus be expressed by  $\|\mathbf{u}^{ts} - \mathbf{u}^R\|_{E_\Omega}$ . It is related to *resi* by  $\mathbf{A}_{rr} \cdot \mathbf{u}_r - \mathbf{B}_r$  vector:

$$\|\mathbf{u}^{ts} - \mathbf{u}^R\|_{E_\Omega} = \sqrt{A(\mathbf{u}^{ts} - \mathbf{u}^R, \mathbf{u}^{ts} - \mathbf{u}^R)} = \sqrt{(\mathbf{A}_{rr}(\mathbf{u}_r - \mathbf{u}_r^R)) \cdot (\mathbf{u}_r - \mathbf{u}_r^R)} = \sqrt{(\mathbf{A}_{rr} \cdot \mathbf{u}_r - \mathbf{B}_r) \cdot (\mathbf{u}_r - \mathbf{u}_r^R)} \quad (16)$$

So when  $\mathbf{A}_{rr} \cdot \mathbf{u}_r - \mathbf{B}_r$  vector tends to the zero vector, both *resi* and  $\|\mathbf{u}^{ts} - \mathbf{u}^R\|_{E_\Omega}$  tend to zero.

It is also interesting to compare the two-scale solution to the continuous solution. The associated energy error is  $\|\mathbf{u}^{ts} - \mathbf{u}^C\|_{E_\Omega}$  and can be expressed as:

$$\begin{aligned} \|\mathbf{u}^{ts} - \mathbf{u}^C\|_{E_\Omega}^2 &= \int_\Omega \boldsymbol{\varepsilon}(\mathbf{u}^{ts} - \mathbf{u}^R + \mathbf{u}^R - \mathbf{u}^C) : \mathbf{C} : \boldsymbol{\varepsilon}(\mathbf{u}^{ts} - \mathbf{u}^R + \mathbf{u}^R - \mathbf{u}^C) d\Omega = \\ &\quad \|\mathbf{u}^{ts} - \mathbf{u}^R\|_{E_\Omega}^2 + \|\mathbf{u}^R - \mathbf{u}^C\|_{E_\Omega}^2 + 2A(\mathbf{u}^R - \mathbf{u}^C, \mathbf{u}^{ts} - \mathbf{u}^R)_\Omega \end{aligned} \quad (17)$$

Subtracting (3) to (10) gives as  $\mathcal{M}^R \subset \mathcal{M}^C$ :

$$\forall \mathbf{v}^* \in \mathcal{M}_0^R, A(\mathbf{u}^R - \mathbf{u}^C, \mathbf{v}^*)_\Omega = B(\mathbf{v}^*)_\Omega - B(\mathbf{v}^*)_\Omega = 0 \quad (18)$$

Based on (18) and as  $\mathbf{u}^{ts} - \mathbf{u}^R \in \mathcal{M}_0^R$ , then the extra term of (17) vanishes:

$$A(\mathbf{u}^R - \mathbf{u}^C, \mathbf{u}^{ts} - \mathbf{u}^R)_\Omega = 0 \quad (19)$$

Leading to the relation:

$$\|\mathbf{u}^{ts} - \mathbf{u}^C\|_{E_\Omega}^2 = \|\mathbf{u}^{ts} - \mathbf{u}^R\|_{E_\Omega}^2 + \|\mathbf{u}^R - \mathbf{u}^C\|_{E_\Omega}^2 \quad (20)$$

The second term on the right-hand side of (20) represents the error introduced by the reference mesh discretization with respect to the continuous solution. The first one is the error introduced by the two-scale method. Most publications on the subject do compute  $\mathbf{u}^R$  with another solver and verify a posteriori that  $\|\mathbf{u}^{ts} - \mathbf{u}^C\|_{E_\Omega}$  tends to  $\|\mathbf{u}^R - \mathbf{u}^C\|_{E_\Omega}$  (i.e. that  $\|\mathbf{u}^{ts} - \mathbf{u}^R\|_{E_\Omega}$  tends to zero) in few iterations. In this work *resi* carries out this verification during the iterations. A numerical comparison of these errors is given in section 6.1.

### 3.3 Specific global-scale system construction: the algebraic operator

The  $\mathbf{u}_r$  (as mentioned above, the simplified notation of  $\mathbf{u}_r^{ts}$ ) vector will act as a bridge between computational tasks. It stores classical values at the nodes of  $\mathbf{u}^{ts}$  field which will be used to compute *resi* and impose boundary conditions on fine-scale problems. The  $\mathbf{u}_r$  dofs of this field can be related to global-scale field dofs via the kinematic equation (5).

With this equation, for any node  $\mathbf{x}^j$  of the reference mesh, it is possible to write, without any approximation, that the two-scale solution  $\mathbf{u}^{ts}$  is equal to the global enriched discrete solution at this location:

$$\mathbf{u}^{ts}(\mathbf{x}^j) = \mathbf{U}^G(\mathbf{x}^j) = \sum_{i \in I^g} N^i(\mathbf{x}^j) \mathbf{U}^i + \sum_{p \in I_e^g} N^p(\mathbf{x}^j) \mathbf{E}^p * \mathbf{F}^p(\mathbf{x}^j) \quad (21)$$

This can be rewritten in algebraic form as:

$$\mathbf{u}_M = \mathbf{T}_{MG} \cdot \mathbf{U}_G \quad (22)$$

where  $\mathbf{T}_{MG}$  is a linear interpolation operator whose structure and construction are given in D. In this work, the process of eliminating linear relations (12) is made transparent by choosing, from the R-set, to first eliminate the L-set before applying linear interpolation. Thus, the operator in (22) interpolates from the G-set to the M-set.

Considering the matrices of (11) with the L-set eliminated, and the equation (22) to apply a change of variable, the equality between the potential energy and the work of external forces can be written as follows:

$$\mathbf{U}_G^t \cdot \mathbf{T}_{MG}^t \cdot \mathbf{A}_{MM} \cdot \mathbf{T}_{MG} \cdot \mathbf{U}_G = \mathbf{U}_G^t \cdot \mathbf{T}_{MG}^t \cdot \mathbf{B}_M \quad (23)$$

This gives the following system (see E for the detailed construction):

$$\mathbf{A}_{gg} \cdot \mathbf{U}_g = \mathbf{B}_g \quad (24)$$

From a practical point of view, the sub-blocks of  $\mathbf{T}_{MG}$ ,  $\mathbf{A}_{MM}$  and  $\mathbf{B}_M$  are large sparse matrices, so they are never fully assembled in memory but stored in blocks using a per macro-element strategy. This strategy, which gathers in memory all the matrices and vectors necessary for the calculation relative to a macro element, is favorable to the reduction of cache misses and to multi-threading computation. Moreover, during the two-scale loop, only the terms related to  $\mathbf{F}^p$  (related to  $\mathbf{T}_{Fe}$  operator given in E ) have to be updated at each scale iteration. Thus some sub-block of  $\mathbf{A}_{gg}$  and  $\mathbf{B}_g$  are constant during the iteration and are computed and assembled only once at initialization time.

The INIT procedure (algorithm F.2 detailed in F ) is in charge of this initialization. Let  $\omega^{e_{macro}}$  be the region of  $\Omega$  covered by a macro element  $e_{macro}$ .  $\omega^{e_{macro}}$  is discretized by one or more micro-elements of the reference mesh. With two loops on all macro elements, the INIT procedure integrates and assembles (10) over  $\omega^{e_{macro}}$  with the elimination of (12) but keeping Dirichlet terms. The resulting matrices and vectors  $\mathbf{A}_{FF}^{e_{macro}}$  and  $\mathbf{B}_F^{e_{macro}}$  are stored for all SP elements. From this first matrix assembly of  $\mathbf{A}_{FF}$  and  $\mathbf{B}_F$  per block and the creation of the sub blocks of  $\mathbf{T}_{MG}$ , all the constant terms of  $\mathbf{A}_{gg}$  and  $\mathbf{B}_g$  can be computed algebraically and assembled in two dedicated memory areas,  $\mathbf{A}_{gg}^{ini}$  and  $\mathbf{B}_g^{ini}$ .

### 3.4 global to local transfer

In this work the idea is to obtain the  $\mathbf{u}^{ts}$  field not by solving directly (13) but by solving (24) and use (22) to go from  $\mathbf{U}^G$  to  $\mathbf{u}_F$ . This last point is achieved by the UPDATE\_MICRO\_DOFS procedure (algorithm F.4 detailed in F) which uses the same per-macro-element storage strategy and stores the  $\mathbf{u}^{ts}$  field in the  $\mathbf{u}_F^{e_{macro}}$  vectors attached to SP macro-elements. Note that this procedure does not loop over the NSP elements and that no information about the h-set is stored in memory because in the computational tasks related to  $\mathbf{u}^{ts}$ , this information can be ignored as we will see later.

### 3.5 Local problem

In this work, as in the section 2, the solution of the local problem for a patch  $p$  will be given by solving (7) but using a different mechanism to create the linear system. Consider that  $\omega_p$  is equal to  $\bigcup_{e_{macro} \in J^p} \omega_{e_{macro}}$ , with  $J^p$  the set of macro-elements of the patch  $p$ . As the local problems are parts of the reference problem sharing with it its definition and discretization, the integration of (7) has already been partially done when integrating (10) over  $\omega^{e_{macro}}$ . Thus, creating the matrix and vector for a patch  $p$  is just assembling the blocks  $\mathbf{A}_{FF}^{e_{macro}}$  and  $\mathbf{B}_F^{e_{macro}}$  with  $e_{macro} \in J^p$ .

As for the Dirichlet boundary conditions on  $\partial\omega_p$ , they are directly obtained from the  $\mathbf{u}^{ts}$  field ( $\mathbf{u}_F^{e_{macro}}$  dofs). It is strictly the same as using  $\mathbf{U}^G$  because  $\mathbf{u}_F$  which comes from (22) is computed with  $\mathbf{T}_{MG}$  constructed from (5) as the space  $\mathcal{M}^G$  constructed from same kinematic equation. The application of these boundary conditions gives the following set of local linear systems:

$$\forall p \in I_e^g \quad \mathbf{A}_{qq}^p \cdot \mathbf{u}_q^p = \mathbf{B}_q^p \quad (25)$$

Again, it is the INIT procedure, with a loop over the patches, that is responsible for creating  $\mathbf{A}_{qq}^p$  which is constant during the two-scale iteration. Similarly, the constant part of the vector  $\mathbf{B}_q^p$ , called  $\mathbf{B}_q^p$  and the constant coupling Dirichlet term  $\mathbf{D}_{qd}^p$  are computed in this loop over the patches (see F for more details). Note that the use of Dirichlet

boundary conditions for local problems simplifies the software implementation and offers good performance for solving (25): smaller system size, simple constant algebraic operator ( $\mathbf{D}_{qd}^p$ ) for imposing the prescribed displacements, and the matrix is not polluted by additional parameters (springs) to be set. But the consequence of this choice on the proposed two-scale loop has not been studied and should be in a future work.

### 3.6 The two-scale loop

When the INIT procedure is completed, all local structures associated with macro-elements or patches are allocated and partially computed. Before entering the two-scale loop, the algorithm 1 initializes the field  $\mathbf{u}^{ls}$  by calling UPDATE\_MICRO\_DOFS with the vector  $\mathbf{U}_g$ , solution of a specific macro-scale problem (in general the unenriched macro-scale problem but it can come from another computation).

The algorithm 1 then enters the two-scale loop and first computes the solutions  $\mathbf{u}_q^p$  of (25) by calling the MICRO\_SCALE\_RESOLUTION procedure (algorithm F.5 detailed in F). This procedure creates vectors  $\mathbf{B}_q^p$  from the constant terms and the coupling Dirichlet terms multiplied by the current subset of  $\mathbf{u}_F$ . It then solves the systems with a direct solver (§ of the algorithm F.5), factoring only once the matrices.

Having all the  $\mathbf{u}_q^p$ , the global to local step is done and the local to global step can start by calling the UPDATE\_MACRO\_PRB procedure (algorithm F.3 detailed in F). This procedure computes the enrichment function from the solution  $\mathbf{u}_q^p$  and using  $\mathbf{A}_{gg}^{ini}$  and  $\mathbf{B}_g^{ini}$  finishes the algebraic computation of  $\mathbf{A}_{gg}$  and  $\mathbf{B}_g$ . The system (24) is then solved (§ of the algorithm 1) providing  $\mathbf{U}_g$  solution.

A call to UPDATE\_MICRO\_DOFS with this new  $\mathbf{U}_g$  solution updates  $\mathbf{u}^{ls}$  field so that the *resi* criterion (14) can be computed for the current iteration. This is done by COMPUTE\_RESIDUAL procedure described in the next section. Depending on whether *resi* is greater than the given  $\varepsilon$ , the loop must continue or not.

### 3.7 residual criterion computation

The numerator of the equation (14) can be divided as follows:

$$resi = \frac{\left\| \begin{array}{c} \mathbf{A}_{hr} \cdot \mathbf{u}_r - \mathbf{B}_h \\ \mathbf{A}_{fr} \cdot \mathbf{u}_r - \mathbf{B}_f \end{array} \right\|}{\|\mathbf{B}_r\|} \quad (26)$$

In this work, the h-set part of the residual vector is considered as zero. This is justified by the fact that the discretization of the NSP elements at both scales is the same: the h-set part of the r-set is the same as the h-set part of the g-set. Thus, since the † resolution, when performed by a direct solver, provides a "zero" residual error of the g-set system (zero at the machine accuracy), all this residual vector is zero and in particular its h-set rows. The computation of *resi* is therefore simplified to:

$$resi = \frac{\|\mathbf{A}_{fr} \cdot \mathbf{u}_r - \mathbf{B}_f\|}{\|\mathbf{B}_r\|} \quad (27)$$

The organization of the data by macro-element both simplifies and complicates the computation of (27) performed by the COMPUTE\_RESIDUAL procedure (algorithm F.6 detailed in F). The simplicity comes from the computation by  $e_{macro}$  of the vector  $\mathbf{A}_{FF}^{e_{macro}} \cdot \mathbf{u}_F^{e_{macro}} - \mathbf{B}_F^{e_{macro}}$  with all the vectors and the matrix available as data attached to the  $e_{macro}$  element. The complexity comes from the accumulation of the special local scalar product of these vectors to obtain term  $\|\mathbf{A}_{fr} \cdot \mathbf{u}_r - \mathbf{B}_f\|$ .

The  $\|\mathbf{B}_r\|$  term of the equation (27) is computed by the procedure COMPUTE\_B\_NORM described by the algorithm F.7 in F. This algorithm is very similar to the algorithm F.6 in that the scalar product of the vector  $\mathbf{B}_r$  by itself is transformed into a sum of local dot product. But as  $\mathbf{B}_r$  remains unchanged during the two-scale loop, this procedure is called only once during the initialization by the INIT procedure. The  $\|\mathbf{B}_r\|$  term is therefore supplied as an argument to the COMPUTE\_RESIDUAL procedure which computes the *resi* numerator and just divide by this argument to obtains *resi*.

### 3.8 two-scale enrichment function

In this work we choose to approach blending element problem by using a shift to cancel the enrichment function at the coarse-scale enriched node location and by forcing discretization transition to be embedded in patches, contrasting with SGFEM [4] presented in (9). This last point is somewhat similar to the idea in [9] where enrichment was added to nodes initially not enriched in blending elements, with the use of a special ramp function to correct the original enrichment function. Here, mixed discretization patches are added, so enrichments are added (red node in figure 1c)

on initially unenriched blending elements nodes (unenriched because their support did not cover the behavior being captured). And the treatment of hanging nodes replaces the effect of the ramp function. In this way, the original blending element (orange element connected to red node in figure 1c) regain their partition of the unity property and the new blending elements (yellow element in figure 1c) are not perturbed thanks to the use of a null enrichment function. Some tests not provided in this work show that the proposed enrichment give a good convergence compare to that given by the SGFEM enrichment. In this work, the two-scale enrichment function  $\mathbf{F}^p(\mathbf{x})$  is :

$$\forall p \in I_e^g, \forall \mathbf{x} \in \omega_p \mathbf{F}^p(\mathbf{x}) = \mathbf{u}^{Q^p}(\mathbf{x}) - \mathbf{u}^{Q^p}(\mathbf{x}^p) \text{ and } \forall \mathbf{x} \notin \omega_p \mathbf{F}^p(\mathbf{x}) = \mathbf{0} \quad (28)$$

where:

- $\mathbf{u}^{Q^p}(\mathbf{x})$  and  $I_e^g$  are defined in section 2
- $\mathbf{x}^p$  is the location of the enriched node  $p$

Another specificity of this work is the wish that  $\mathbf{u}^{ts}$  converges to  $\mathbf{u}^R$  which can only be achieved if the enrichment function is linearly interpolated on the reference mesh following the construction and use of  $\mathbf{T}_{MG}$ . Thus, the kinematic equation actually used at the global scale, corresponding to the application of the  $\mathbf{T}_{MG}$  operator, is:

$$\mathbf{U}(\mathbf{x}) = \sum_{i \in I^g} N^i(\mathbf{x}) \mathbf{U}^i + \sum_{p \in I_e^g} \mathbf{E}^p \sum_{m \in \bar{I}_p^l} n^m(\mathbf{x}) N^p(\mathbf{x}_m) \mathbf{F}^p(\mathbf{x}_m) \quad (29)$$

where  $\bar{I}_p^l = I_p^l \setminus \{\text{hanging nodes}\}$  since the L-set has also been eliminated in the patch problems. The construction of the second term of (29) is first illustrated, in 1D, in the figure 2 where artificial elevations show the different quantities of the 8 micro-edges of a  $p$  patch (composed of 2 macro-edges not shown here). The same type of illustration of the

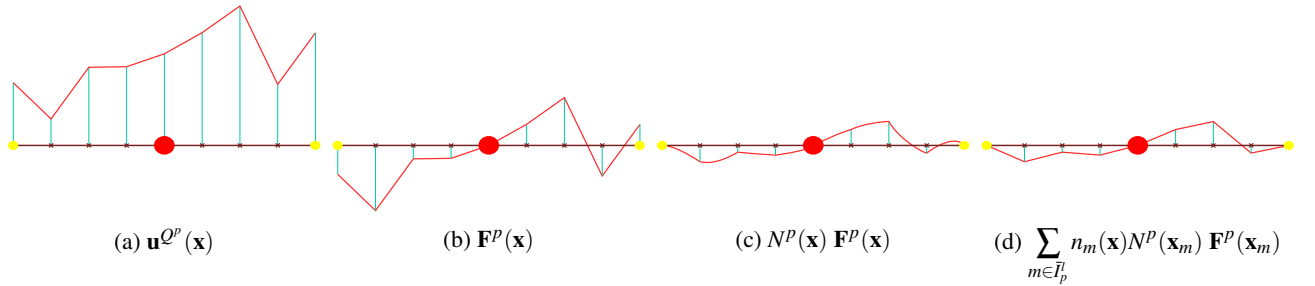


Figure 2: Construction of an interpolated generalized approximation function for a 1D patch  $p$ . For visualization purposes, the quantities here are artificial elevations of the patch mesh.

2D example in figure 1 is shown in figure 3. Again, artificial elevations show the various quantities outside the plane formed by a patch  $p$ . The solutions  $\mathbf{u}^{Q^p}(\mathbf{x})$  (figure 2a and 3a) are completely arbitrary. The enriched function  $\mathbf{F}^p(\mathbf{x})$

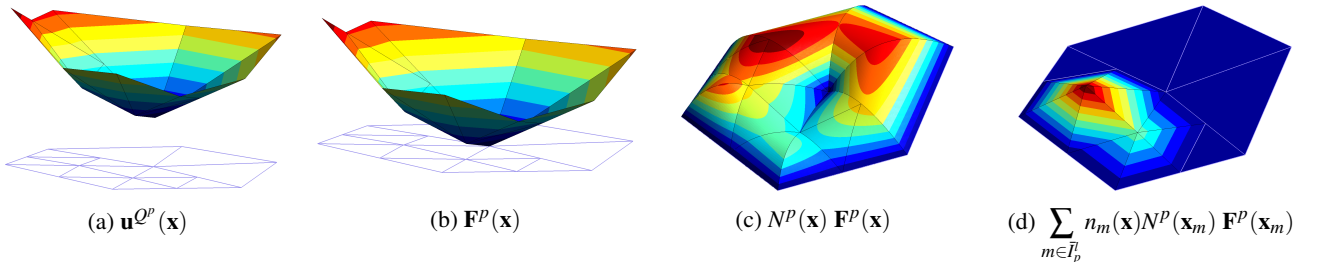


Figure 3: Construction of an interpolated generalized approximation function for a  $p$  patch (based on the example in figure 1 ). For visualization purposes, the quantities transformed into scalars are drawn here as artificial elevations outside the plane formed by the patch mesh. (a,b) and (c,d) are represented from two different viewpoints in space for better visualization.

corresponding to the equation (28) is given in figure 2b and 3b. By construction, this function is null at the location of the enriched node. When multiplied by the standard finite element approximation function to form the generalized

finite element approximation function (figure 2c and 3c), all the boundary values of the patches become zero and we obtain second order curves/surfaces. The final linear interpolation is shown in the figure 2d and 3d. In the 2D example, where a mixture of refined and unrefined elements forms the patch, the interpolated generalized function is necessarily zero on the unrefined element (yellow blending elements in the figure 1c). This property implies that blending elements have unenriched nodes and enriched nodes with zero contribution from enrichment function. Thus, the enrichment contribution is zero for the blending element and the partition of unity is saved because only the classical terms matter. For refined elements,  $N^p(\mathbf{x}_m) \mathbf{F}^p(\mathbf{x}_m)$  is not zero for any location inside the patch (if  $\mathbf{F}^p(\mathbf{x}_m) \neq \mathbf{0}$ ). For the hanging nodes, since they are eliminated in  $\tilde{l}_p$  their values are therefore zero which is consistent with the values in the unrefined elements.

Note that if the refined elements correspond only to a terminal connection specific to the adaptation tool (element added in between figure 1d and figure 1e in C), then, despite the refinement, the associated generalized finite element approximation function is zero on these elements. To avoid this situation, which can lead to a singular problem, the refined SP elements are always divided at least once.

## 4 Theoretical sequential algebra performance

Since the two-scale method uses a resolution with sparse matrix of different patterns and densities, and since the number of iterations of the two-scale loop is not known in advance, estimating the algebraic performance of the two-scale method is difficult in a general context. It is even more complex when using parallelism. Thus, to obtain the numerical complexity of the two-scale solver, we will use a simple sequential numerical example to be able to count the number of flops<sup>5</sup> in each part of the algorithm. The number of flops used will then be expressed as a polynomial function of the problem dimensions keeping only the leading terms to obtain the order of magnitude ( $\mathcal{O}(n)$  notation). If we take a meshed cube with a finite hexahedral element of order one in 3D, we can, using octree refinement, simply count the coarse scale dofs, the patches and the patches' dofs.

For the linear resolution steps of the two-scale method, only direct sparse solver will be considered. Thus, the number of flops for the factorization, in terms of the  $n$  dimension of the problem, is approximately between  $n^2$  and  $n^3$  (dense matrix). And for backward and forward substitution the cost is in between  $2.n$  and  $2.n^2$ . Depending on the strategy of the solver (multi-frontal, left-looking, ...), the reordering of the symbolic factorization (nested dissection, minimum degree, ...) and the density of the initial matrix, the number of flops varies greatly and depends on a variable number of parameters. Thus, to estimate these quantities, a sparse ratio parameter  $SR$  is introduced such that the dimension used to count the number of flops  $n_f$  is:

$$n_f(n, SR) = \sqrt{SR.n^2} \quad (30)$$

with  $SR \in ]0, 1]$ . Then the number of flops for factorization ( $count_{fact}$ ), backward/forward computation ( $count_{bf}$ ) and resolution ( $count_{resolv}$ ) are, using a dense estimation:

$$count_{resolv}(n, SR) = count_{fact}(n, SR) + count_{bf}(n, SR) \quad (31)$$

$$count_{fact}(n, SR) = (n_f(n, SR))^3 \quad (31a)$$

$$count_{bf}(n, SR) = 2.(n_f(n, SR))^2 \quad (31b)$$

This  $SR$  parameter is completely arbitrary. It is introduced to verify that the conclusions obtained in this section are not impacted by the lack of accurate estimation of the factorization and solving phase.

For discretization, the root of the octree uses one element to represent the problem. It corresponds to zero level. A level, noted  $L$  in the following, describes the depth in the octree tree. With  $L = 0$  being the starting level, to go from  $L$  to  $L + 1$ , the octree refinement adds a new node in the middle of all edges, faces and elements of level  $L$ . Then, each element of the level  $L$  is replaced by 8 hexahedra encapsulated in it and connected to the old and new nodes. The number of classical dofs for a level  $L$  is easily deduced from this refinement strategy and is :

$$nb_{dof}(L) = 3.(2^L + 1)^3 \quad (32)$$

Thus, the two-scale coarse enriched problem defined at the  $L_c$  level will cost for  $N_l$  two-scale iteration with a sparse ratio parameter  $SR_c$  using (31) and (32):

$$cost_{coarse}(L_c, N_l, SR_c) = N_l \times count_{resolv}(2 \times nb_{dof}(L_c), SR_c) \quad (33)$$

For a given coarse level  $L_c$ , it is possible to obtain in the same way the cost of computing patches (factorization and solving) for  $N_l$  two-scale iterations, a sparse ratio parameter  $SR_p$  and a final refinement level  $L$ . This is given by the

<sup>5</sup>flop=floating-point operation: one addition, subtraction, division or multiplication of two floating-point numbers



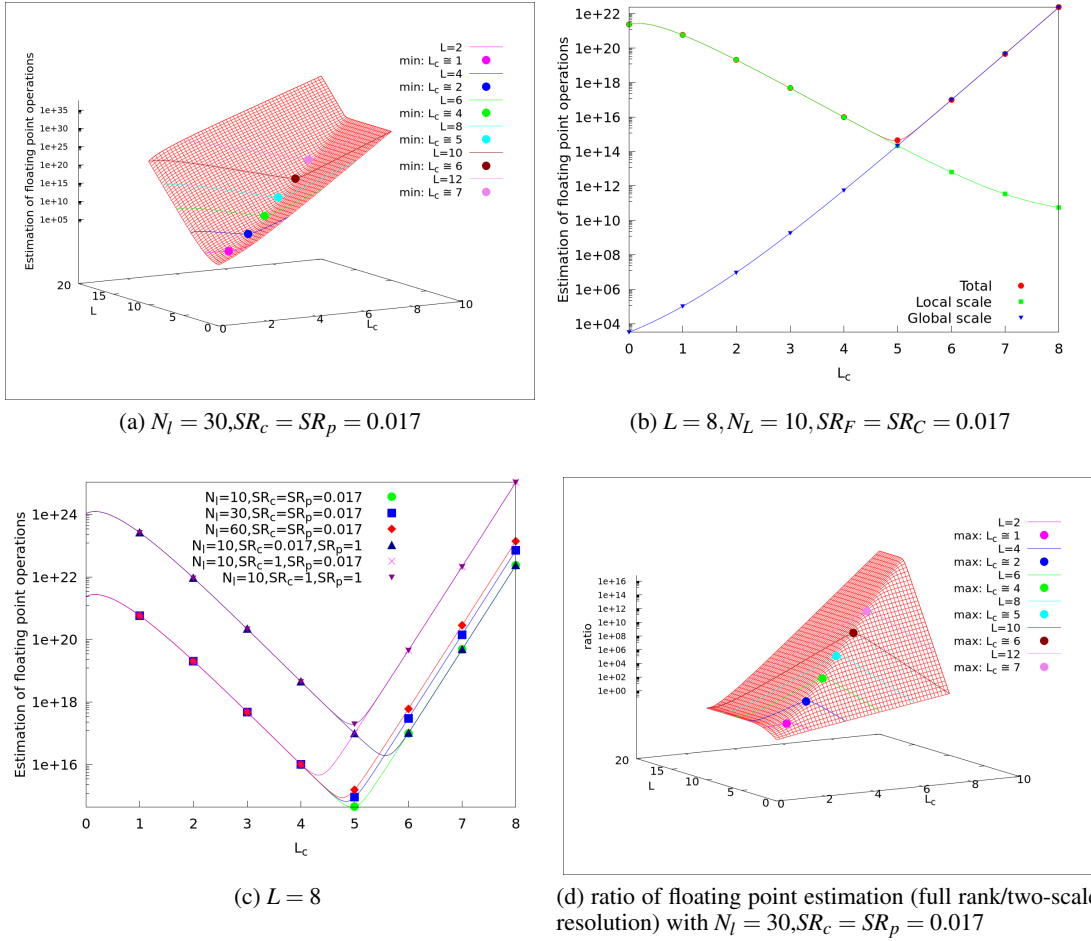


Figure 4: floating point estimation for different value of  $L_c, L, SR_c$  (sparse ratio for coarse problem),  $SR_F$  (sparse ratio for fine problems) and  $N_l$  (number of two-scale iteration)

function  $cost_{patch}(L_c, L, N_l, SR_p)$  detailed in G. Using (33) and (60) we can state that the cost of the two-scale method is:

$$cost_{two-scale}(L_c, L, N_l, SR_c, SR_p) = cost_{patch}(L_c, L, N_l, SR_p) + cost_{coarse}(L_c, N_l, SR_c) \quad (34)$$

Fixing  $N_l, SR_c, SR_p$  the equation (34) for some values of  $L_c$  and  $L$  give the surface of figure 4a. We can see on this continuous representation of (34) that the iso- $L$  curves have a minimum for a specific  $L_c$  value. It means that two-scale method has an optimal coarse level for a fixed target level that provides the best performance (i.e. the lowest number of flop consumption). This can be understood by looking at figure 4b for a specific target  $L = 8$  and fixed  $N_l, SR_c, SR_p$  where the equation (34) is divided into patch contribution (equation (60)) and coarse-level contribution (equation (31)). In this figure, it is clear that the antagonistic evolution of the performance of patch solving and coarse-scale problem solving lead to having a minimal value at the intersection of the curves. In figure 4c the variation of the parameters  $N_l, SR_c, SR_p$  does not change the fact that a minimum exists. In this example where  $L = 8$ , when the number of loop increases, the minimum remains the same. When we consider the variation of the sparsity of the matrix (up to dense case), the minimum is moved around its original position depending on whether the coarse problem or the patch problems are denser or not. With denser matrices for patches, it is naturally preferable to increase  $L_c$  to have smaller patches. And with a denser coarse matrix, it is better to decrease  $L_c$  to have a smaller coarse problem to solve. When both sparsities increase, the minimum remains the same but with a higher value.

Figure 4d presents, as a ratio, an estimate of the performance of a full rank solver (using the equation (31)) compared to the two-scale solver. A ratio greater than, equal to, or less than 1 indicates that the full rank solver uses more, the same, or less flop than the two-scale solver respectively. The surface naturally has a maximum for iso- $L$  curves with the same  $L_c$  as the minimum of the figure 4a (on iso- $L$  curves the cost of the full rank solver is constant). In this

example, the theoretical performance of the two-scale solver compared to the full rank solver is much better for  $L > 2$ . For  $iso - L = 2$  the optimal ratio at  $L_c = 1$  is only of 1.76. And for  $L = 1$ , as in this case the patch problems size are almost equivalent to the  $L_c$  level of discretization no gain is obtained. This illustrates the fact that the two-scale method, to be effective, must be used at a target level that allows to start from a coarse level that induces a scaling effect.

The conclusion drawn from the analysis of this octree refinement example were also observed in parallel with the different test cases studied below. Parallelism, the nature of the unstructured mesh, and the cost of assembly also impact the choice of the optimal coarse mesh for a given fine-scale target discretization. But the observation of the test case 6.1 led to use the following formula to define the scale jump for most cases with regular refinement:

$$L = L_c + 3 \quad (35)$$

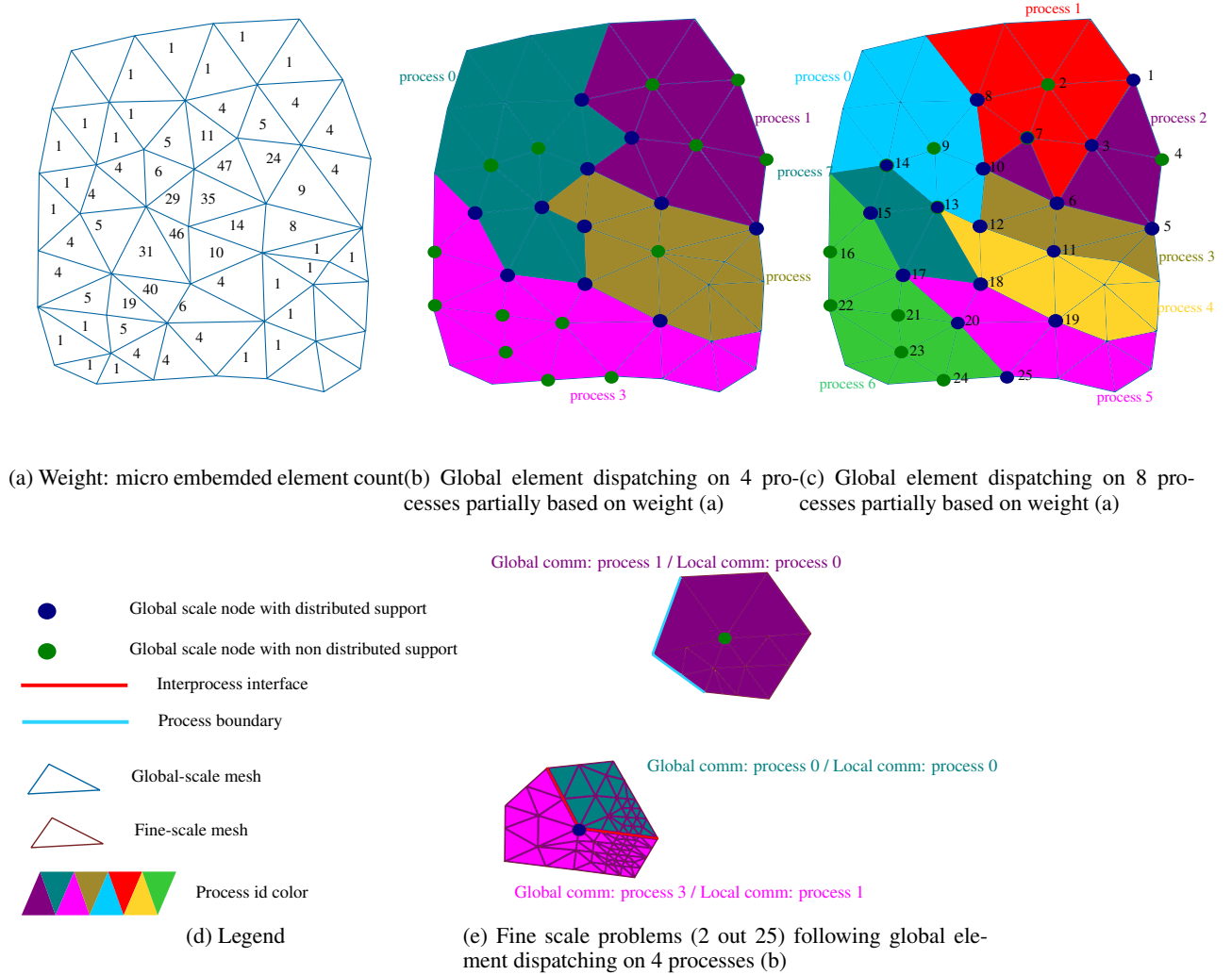


Figure 5: two-scale fictitious 2D problem of figure1 distributed on processes

## 5 Parallel paradigm

This work does not use shared-memory multithreaded parallelism and uses only the distributed-memory message passing paradigm<sup>6</sup>. This choice comes from the thread-safety constraint which would have generated too much

<sup>6</sup>In this work we use the MPI-3.0 (or higher) message passing standard.

implementation work for this first study (for example the in-house library used to code the two-scale method is not thread-safe). As a result, multi-threading is never used in this study and to be fair when comparing with other methods, their multi-threading capability was also disabled. Thus, in this section, parallelism will always concern the message passing paradigm.

Parallelism is introduced at all scales in all two-scale frameworks, but with a quite different granularity. At the global level, the mesh is distributed over processes (see figures 5b and 5c for the example of figure 1 distributed over 4 and 8 processes respectively), based on a macro-element partitioning, in order to allow a good load balancing. This partitioning (not evaluated in depth in this paper), given by ParMetis ([16]) in this work, is supposed to balance the cost of creating linear systems, assembling them and solving them at both scales. To do this, a cost per macro-element is obtained directly from the number of its encapsulated micro-elements (see figure 5a) and the number of enriched nodes. If the entire global-scale mesh is refined (as in the examples in the section 6.1 and 6.2), all macro elements have roughly the same number of encapsulated micro elements and enriched nodes. Thus, the cost per element can be considered as a constant. Now, if only a specific region is involved (see the 2D example in Figure 1a or the example in section 6.3), the number of encapsulated micro-elements and enriched nodes provides weights to the ParaMetis multi-objective partitioning optimization algorithm. In the examples studied, this partitioning provides great scalability for the assembly task, as all processes receive roughly the same amount of micro-elements to integrate and assemble (see in particular the table 2 in section 6.1). It also allows the use of a fairly well balanced parallel resolution for the linear system related to the global-scale problem ( $\dagger$  in the algorithm 1). The section 5.1 gives more details on the choice of solver to use at this level.

At the fine scale, patches follow the distribution of the global scale mesh (see figure 5e) and are therefore naturally distributed in most processes. This results, as in [18], in a high level of coarse-grained parallelism because many fine-scale problems are solved independently (without communication) at the same time by many processes. But some patches are split between the computational units due to the global mesh distribution (see the left patch in the figure 5e). In this work the distributed patch problems are solved entirely in parallel without any overlapping mechanism (phantom variables, ...). The assembly of the problems ( $\mathbf{A}_{qq}^p$  and  $\mathbf{B}_q^p$  of algorithm F.2 and  $\mathbf{B}_q^p$  of algorithm F.5) is thus done in parallel without communication. Then, the matrix contributions of the linear system are provided to a parallel solver ( $\ddagger$  of the algorithm F.5) and treated with a mid-grain parallelism. But this introduces some constraints on the overall process of fine-scale parallel resolution. The distributed patches are no longer independent. Typically, if two distributed patches share the same process, it will be impossible to run the resolution of both in that process. The solver is not able to treat two independent matrices at the same time. This implies that the computation of distributed patches must be scheduled as explained in 5.2. These distributed patches have an ambivalent impact on performance. On the one hand, they reduce the time to solve a rather large fine-scale problem. And on the other hand, if their number increases too much, it expands the amount of communication and can also have an impact on sequencing.

## 5.1 global scale problem parallel resolution

In this work, we first chose an asynchronous parallel MPI sparse direct solver (MUMPS [2, 3]) for the resolution of the linear system associated with the global problem. It was a safe choice (even if the matrix becomes badly conditioned) for this first implementation but by no means a requirement. The symbolic step is performed only once at the beginning of the two-scale loop. Factorization and solving step are repeated for each iteration with the updated  $\mathbf{A}_{gg}$  and  $\mathbf{B}_g$ . With many patches, as the fine scale resolution has good scalability (see the results presented in section 6), many processes can be used well beyond the scalability of the parallel direct solver which solves at the coarse-scale, a problem of rather smaller size. To limit this effect, in all simulations tested, a subset of the available processes (taking at most  $nbp_{max}$  processes,  $nbp_{max}$  arbitrarily chosen to stay within the range of good performance of the direct solver) was used to solve this coarse-scale problem (gathering  $\mathbf{A}_{gg}$  contribution of the processes eliminated from the resolution in the  $nbp_{max}$  retained processes). This version is referred to as Two-scale<sup>gld</sup> below. This reduction had a positive effect, but the overall speed-up<sup>7</sup> of the two-scale resolution was still deteriorated by the coarse-scale efficiency. To reduce this effect, as the two-scale loop iterates over a coarse-scale problem without changing its discretization, it is possible to use a parallel preconditioned iterative solver (conjugate gradient) that starts with the solution of the previous iteration. This choice intrinsically reduces the coarse-scale resolution by considering that the successive solutions are not too far apart from each other, so that the number of iterations in the iterative solver should be small. And this choice adds scalability because the conjugate gradient scales well (to the point where the scalar product becomes a problem). A natural choice is to use for the preconditioner a previous factorization performed by the direct solver. The preconditioning step then only costs a forward/backward resolution, performed in parallel, following the distribution of the direct solver. If not done to many times, it is cheap compared to a full factorization. Note that this technique

<sup>7</sup>the speed-up is the ratio between the time used by an application in single-process mode and the time used in multi-process mode. Ideally, it should give the number of processes used.

does not take into account the stable nature of the classical dofs of the coarse-scale problem as is the case in [19]. This would have added additional complexity regarding load balancing and resolution. Nevertheless, the proposed approach offers apriori a slightly richer preconditioner compared to the block Jacobi proposed in this quote because it incorporates all terms (including the classic  $x$  enriched coupling blocks). The use of the iterative solver and the quality of the preconditioner are controlled using the following arbitrary rules:

1. The iterative resolution is used instead of the direct resolution as soon as the criterion "*resi*" becomes smaller than  $\epsilon \times 10000$  ( $\epsilon$  being the precision to be reach by "*resi*" in algorithm 1 ) and as soon as 2 two-scale iterations have been performed
2. When the iterative resolution takes more than 13 iterations to converge, the preconditioner is recomputed: at the next two-scale iteration, the direct solver is used again to provide a new solution and a new factorization. The iterative solver is then reused in the next two-scale iteration.

The second rule avoids spending too much time in the iterative solver when the preconditioner is not of high quality. The first rule requires waiting for the two-scale solution to reach a minimum quality so that the variation between the two-scale iteration is small enough for the preconditioner to efficiently reduce the number of iterations of the iterative solver. This version is hereafter referred to as Two-scale<sup>gli</sup>. Also note that in this version, for the direct resolution phase, low-rank resolution (see M) can also be used instead of full rank resolution. This is left as future work.

At the coarse scale, another type of solver ( a domain decomposition solver presented in L) was also tested during this study in order to gain scalability as illustrated in section 6.3.

## 5.2 local scale problem scheduling

The 2D example in figure 1 will be used to illustrate the static scheduling algorithm. As already mentioned, two distributed patches that share the same process cannot start solving their linear system at the same time in that process. To avoid this situation, a simple idea is to force distributed patches that share the same process to be computed at different times. To do this, a static<sup>8</sup> scheduling is created that requires all distributed patches over all processes to be computed in a specific order during the two-scale loop. The general idea is to solve as many distributed patches as possible at once, thus maximizing the use of processes and reducing the number of sequences.

To achieve this goal, the first mandatory task is to identify the dependencies between the distributed patches so that they can be sequenced. A distributed patch depends on another if it shares a process with it. This dependency can be extended to local patches to create an undirected graph where the vertices are all patches and the edges represent a process connection (i.e. two patches are connected by an edge if they belong even partially to the same process). Using the mesh distribution in figure 5b this graph concept is illustrated in figure 6b: the vertices of this graph are patches (here, for a quick visual recognition of patches, the vertices of the graph are located at the same place as the enriched nodes of the mesh and each of them has been assigned an arbitrary identifier), the edges of this graph represent a process connection (in this figure, the edges are colored the same way as macro-element of figure 5b to clearly identify the process identifier given in figure 6l).

From this undirected graph, it is possible to create a set  $\mathcal{S}$  of distributed vertices such that for all vertices in  $\mathcal{S}$ , no edge connect them. Thus, these vertices can be computed at the same time because they do not share a common process (no edges connect them). Finding this set  $\mathcal{S}$  (not unique) corresponds in graph theory to the "independent set problem" and will correspond to finding a sequence of the scheduling. It is interesting to maximize the size of  $\mathcal{S}$  (which corresponds to the NP-hard "maximum independent set problem" in graph theory) because on the one hand it maximizes a priori the number of used processes and therefore the load balancing is good. On the other hand, the distributed vertices are consumed faster and therefore the number of sequences can be minimized. When the set  $\mathcal{S}$  is assigned to a sequence (mainly by creating a colored MPI communicator associated with it), its vertices (and their connecting edges) can be removed from the graph. The maximum independent set problem is then solved on the remaining subgraph to find the next sequence. All sequences are found this way until all distributed patches are removed from the subgraph. Then the remaining local patches can be processed in any order as they are independent.

The condition of maximizing the size of  $\mathcal{S}$  is not sufficient to obtain a balanced load. The vertices of  $\mathcal{S}$  must have the same "load" (in a sequence, if a vertex  $v_i$  of  $\mathcal{S}$  takes longer to compute than the others, most of the process will be idle while waiting for  $v_i$  to finish). Thus, with distributed patches having different computational consumption (called weights hereafter), the choice of  $\mathcal{S}$  must be oriented by these weights in order to have approximately the same "load" for all the vertices of  $\mathcal{S}$ . In this work, these weights are simply the number of micro-elements in a patch which reflects its number of dofs and thus its computational cost (see figure 6a computed from the weights in figure 5a). The NP-hard

<sup>8</sup>Avoiding dynamic scheduling is normally more efficient

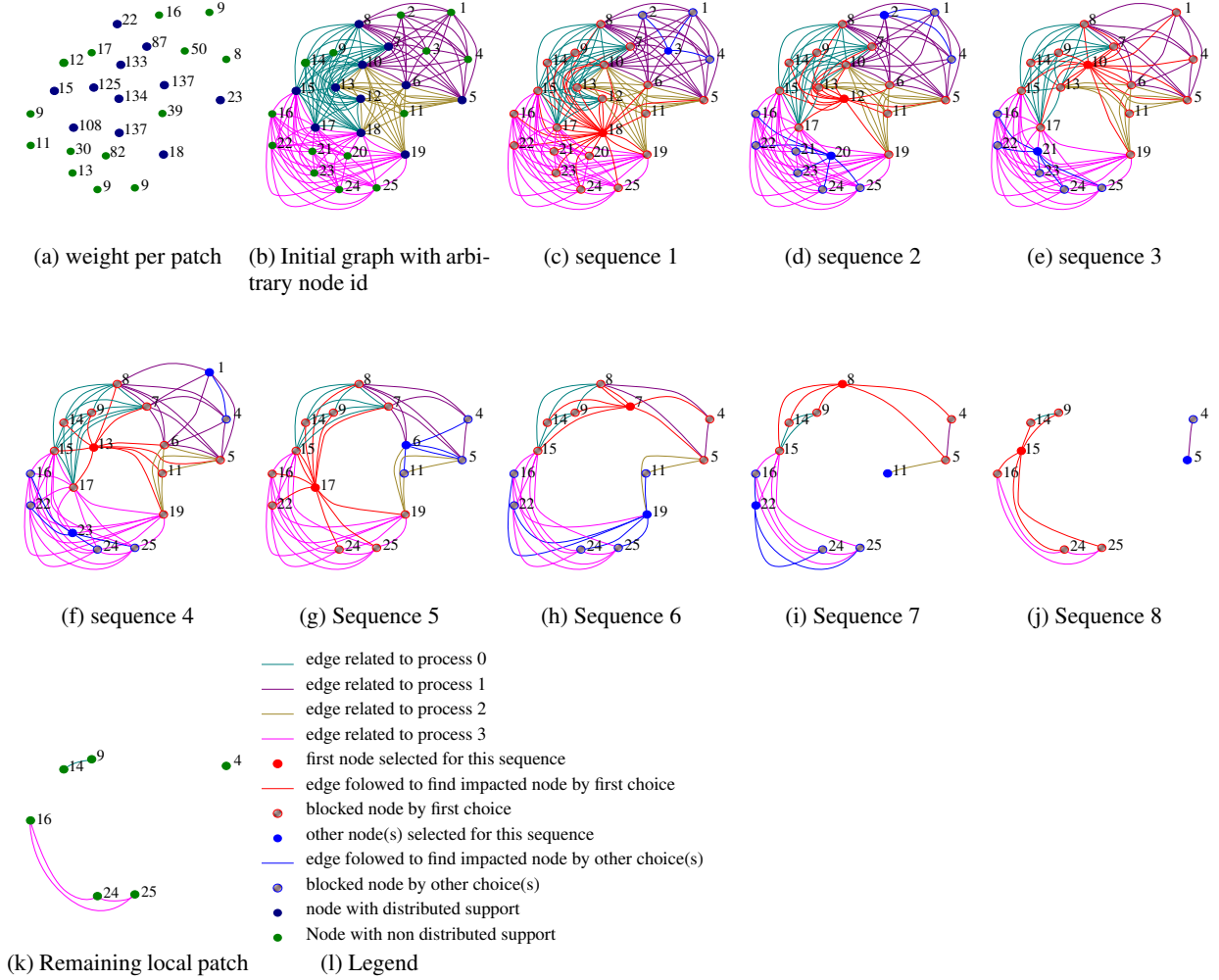


Figure 6: Patch sequencing for figure 5b example. At each sequence, a set  $\mathcal{S}$  is chosen so that as many distributed patches as possible are solved at the same time and during the same time period. A sequence is first built by the lowest process which chooses one of its distributed nodes (red node) in the graph. Then, all the other processes that are not already blocked by this first choice do the same (blue node) in ascending order of the process identification numbers. See H for a detailed description and the table 1a for each  $\mathcal{S}$ . After a sequence is constructed, its nodes and connected edges are removed from the graph to give a new sub-graph used to create the next sequence until no more distributed nodes are available.

nature of the maximum independent set problem, this weighting constraint, and the a priori distributed nature of the undirected graph lead to the choice of a basic sub-optimal heuristic to quickly find a static scheduling.

More precisely, the chosen algorithm, formalized in the algorithms H.8, H.9 and H.10 detailed in H, is played in the table 1a and figure 6 for the example of the figure 5b. In this 2D example, 8 sequences are required, which corresponds to the maximum number of distributed patches per process: in the process with 8 distributed patches, there cannot be less than 8 sequences. With the example of figure 1, distributed on 8 processes (see figure 5c), the table 1b shows that in this case 6 sequences must be computed. But in this case, the last sequence is less efficient because process 3, 4, 5 and 7 are not used. This shows that the scalability of the distributed two-scale method will be influenced by the quality of the algorithm H.8. In the section 6.3, and in particular in the table 3 of this section, we study in a real example the heuristic effect of this algorithm.

Total number of distributed patches: 11						
Maximum number of distributed patches per process: 8						
Minimum number of distributed patches per process: 4						
Average number of distributed patches per process: 6						
sequence	Active patches	Active distributed patches	% Active distributed patches	Active processes	% Active processes	Figure
1	2	1	50	4	100	18,3
2	3	1	33.3	4	100	12,2,20
3	2	1	50	4	100	10,21
4	3	1	33.3	4	100	13,1,23
5	2	2	100	4	100	17,6
6	2	2	100	4	100	7,19
7	3	1	33.3	4	100	8,11,22
8	2	2	100	4	100	15,5
average	2.4	1.4	62.5	4	100	

(a) distribution of figure 5b

Total number of distributed patches: 17						
Maximum number of distributed patches per process: 6						
Minimum number of distributed patches per process: 4						
Average number of distributed patches per process: 5.1						
sequence	Active patches	Active distributed patches	% Active distributed patches	Active processes	% Active processes	Figure
1	3	3	100	8	100	12,7,17
2	3	2	66.7	8	100	10,18,21
3	3	3	100	8	100	13,6,20
4	4	4	100	8	100	8,5,19,15
5	4	4	100	8	100	14,3,11,25
6	3	1	33.3	4	50	9,1,23
average	3.3	2.8	83.3	7.3	91.7	

(b) distribution of figure 5c

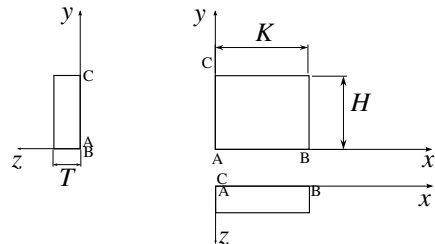
Table 1: Distributed patches sequencing with the algorithm H.8 for the fictitious 2D problem in figure 1 distributed over 4 and 8 processes (figure 5). It does not correspond the calculation of all patches because the average does not take into account the computation of the non-constrained local patches.

## 6 Numerical simulation

All simulation were run on the Liger cluster (see I for details) in the exclusive node condition (no other users at the node level but shared resources at the network and I/O level). In many cases, the two-scale solver is compared to the full rank direct solver MUMPS (denoted by "fr" hereafter), to a low-rank direct solver based on MUMPS (see M, denoted by "blr" hereafter) and to a domain decomposition solver (see L, denoted by "dd" hereafter). Hereinafter, the Two-scale<sup>gld</sup> and Two-scale<sup>gli</sup> versions are referred to as "ts" and "tsi" respectively. In terms of notation  $E$  will be the Young's modulus and  $\nu$  the Poisson's ratio.

### 6.1 Analytic solution

This test is intended to validate the proposed work using a given cubic displacement field over a plate:



$$\vec{u}^C(x, y, z) = \frac{(\nu + 1)(1 - 2\nu)F}{E} \begin{bmatrix} (x^2(\frac{K}{2} - \frac{x}{3}) + 2\nu(y^2 - z^2)) \\ -4\nu xy \\ 4\nu xz \end{bmatrix} \quad (36)$$

where :

- $E = 36.5 \text{ GPa}$
- $\nu = 0.2$
- $F$  is a scalar corresponding to a force
- $K$  is the plate length (figure 7)

Figure 7: Analytical test: plate under volume and surface loading. A, B, and C are the corner points used to fix the rigid body modes.

The imposed loads are obtained from the equation (36) (writing the equilibrium of the system) and the plate is made of a homogeneous isotropic elastic material. The plate is discretized with a coarse mesh (595 tetrahedrons, 188 vertices) which corresponds, hereafter, to the level 0 (L0). Up to 4 other discretizations (L1, L2, L3, L4) derived from this level are used as the global-scale problem. Each of them is built using the adaptation strategy described in C (considering the whole mesh as an area of interest: no hanging nodes). Each level corresponds to the previous one with all its

elements divided once (L2 is L1 divided once). This corresponds exactly to the refinement process used for scaling. Thus, since all nodes are enriched, the 4 meshes are identical to any refined SP targeting the same level (L2 mesh will be the same as the refined super-patch created by refining L0 mesh 2 times).

We evaluate the performance of the proposed parallel two-scale solver and compare it to the solvers "fr", "blr" and "dd". In all figures, for the two-scale curves, "LY from LX" or "from LX" (when the fine scale-level "Y" is implicit) means to use a "X" level for the discretization of the global level and to use a "Y" level for the discretization of the super-patch ( $Y > X$ ). Since the full rank direct solver provides a residual error close to the machine accuracy, a relatively fair comparison requires to adopt a value of  $1.e-7$  for  $\epsilon$  in the algorithm 1, L.12 and M.14. As noted in section 5, for comparison purposes, the multithreading capability of MUMPS and underlying BLAS is not used. Thus, the number of cores (abscissa in many figures) directly represents the number of MPI process dispatched on one or more nodes of the cluster. Figure 8 presents, for different SP refinement, an analysis of the elapsed time used by all

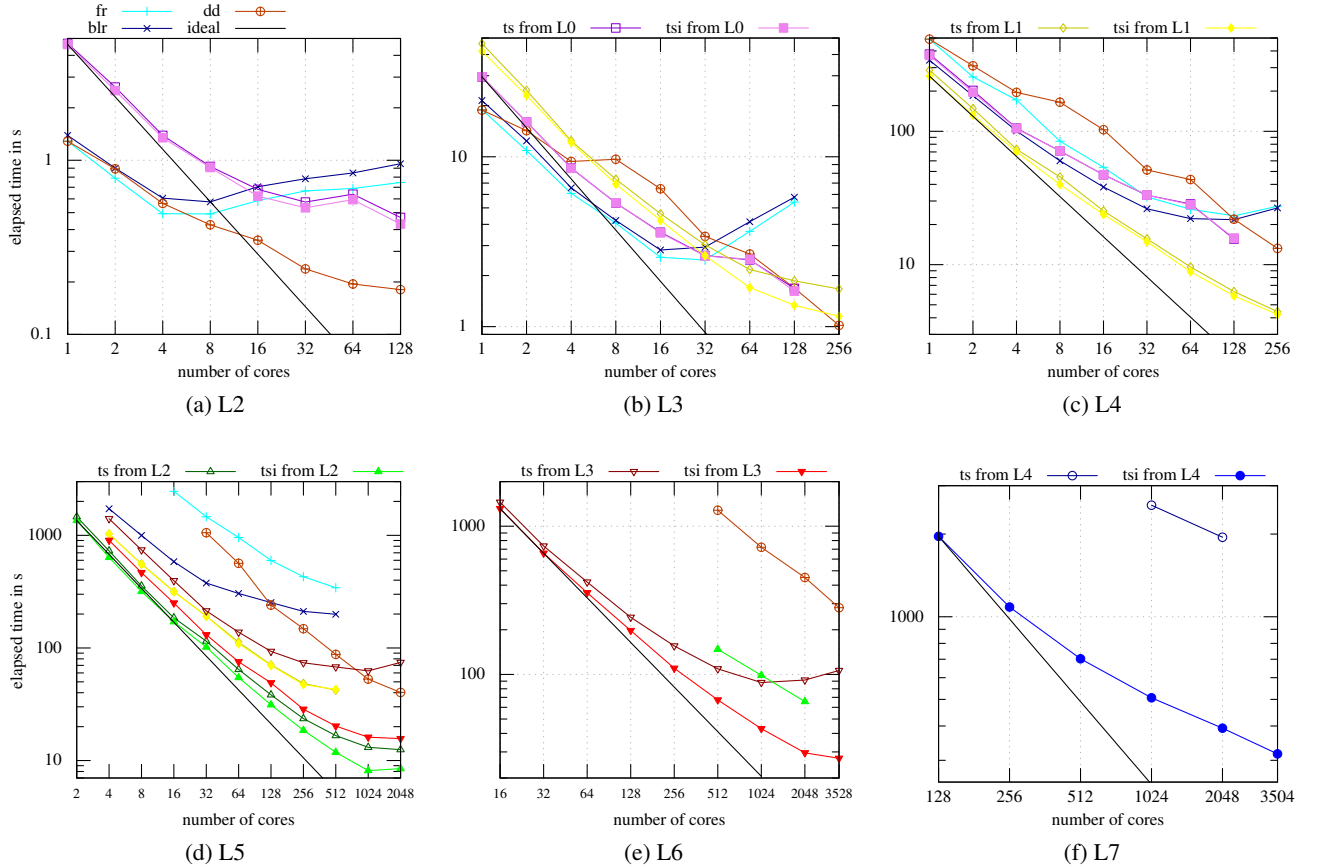


Figure 8: Cubic field: elapsed time in second versus the number of cores. Log/log scale. The results for a fine-scale refinement at L2 , L3, L4, L5, L6 and L7 level are presented in a, b, c, d, e and f respectively. The ideal curve shows the slope when the elapsed time of a single process is perfectly divided by the number of processes used for the calculation (this corresponds to the ideal speed-up). This curve is always shifted so that it starts at the same point as the best two-scale solution for the smallest number of cores.

solvers. The points not present on these curves are mainly due to the fact that, with this cluster, it was impossible to compute them: not enough memory, too much computation time, too many processes for the solver or integer overflow. These limitations only apply to the actual cluster installation and are in no way an absolute judgment on the software used, especially in a non-multi-threaded context.

As discussed in section 4, the two-scale solver has an ideal scale ratio. Thus, for the super-patch refinement of levels L3, L4, L5 and L6 different coarse-scale levels were tested. The observed optimal scale ratio is 3 (best elapsed times curves are "tsi from L1", "tsi from L2" and "tsi from L3" respectively for the super-patch refinement of levels L4 (8c), L5 (8d) and L6 (8e):  $1+3=4$ ,  $2+3=5$  and  $3+3=6$ ), which is in good agreement with the analysis in section 4 and gives equation (35). For L7, only this ratio was used to save computing resources. Regarding the number of dofs, the figure



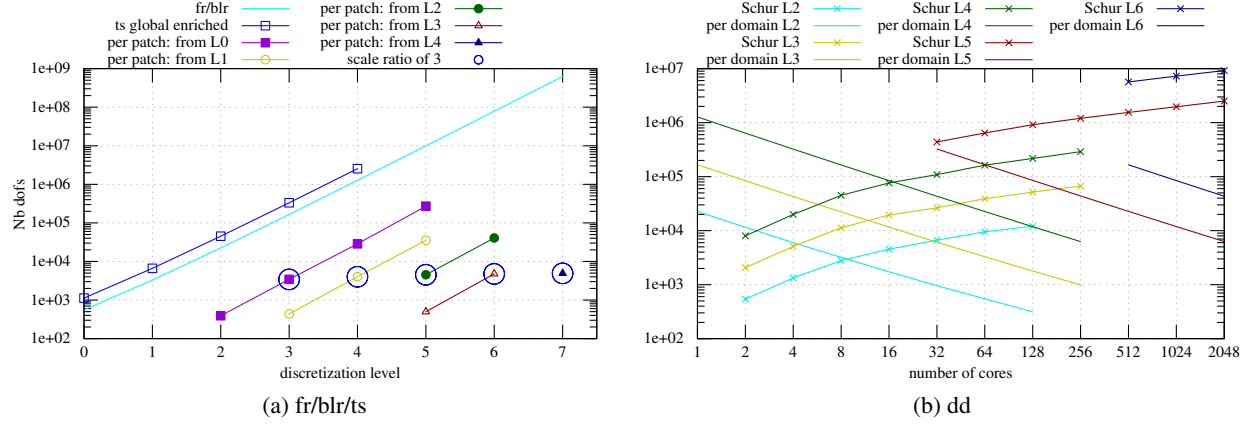


Figure 9: Cubic field: degree of freedom numbers .

9a shows that this ratio corresponds to a fixed number of dofs per patch appearing visually as a horizontal line (circle between 3435 and 4928). Compare to the number of "fr/blr" dofs that increases with discretization, the two-scale solver can keep the size of the fine-scale resolutions within a specific range as long as the scale ratio is maintained. Keeping the same ratio implies increasing the discretization level for the global scale problem. In the figure 9a the "ts global enriched" curve is simply 2 times the "fr/blr" curve (all nodes are enriched). This already highlights the issue of having a global problem with a not so small size. This point is addressed by the Two-scale<sup>gli</sup> version as verified below. Another impact can be seen in figure 10 where increasing the discretization level for a global scale problem implies an increase in the "total" number of patches involved in the computation. This last point is naturally treated by the parallelism as can be seen on the same figure. The number of patches calculated per process decreases when using an increasing number of cores.

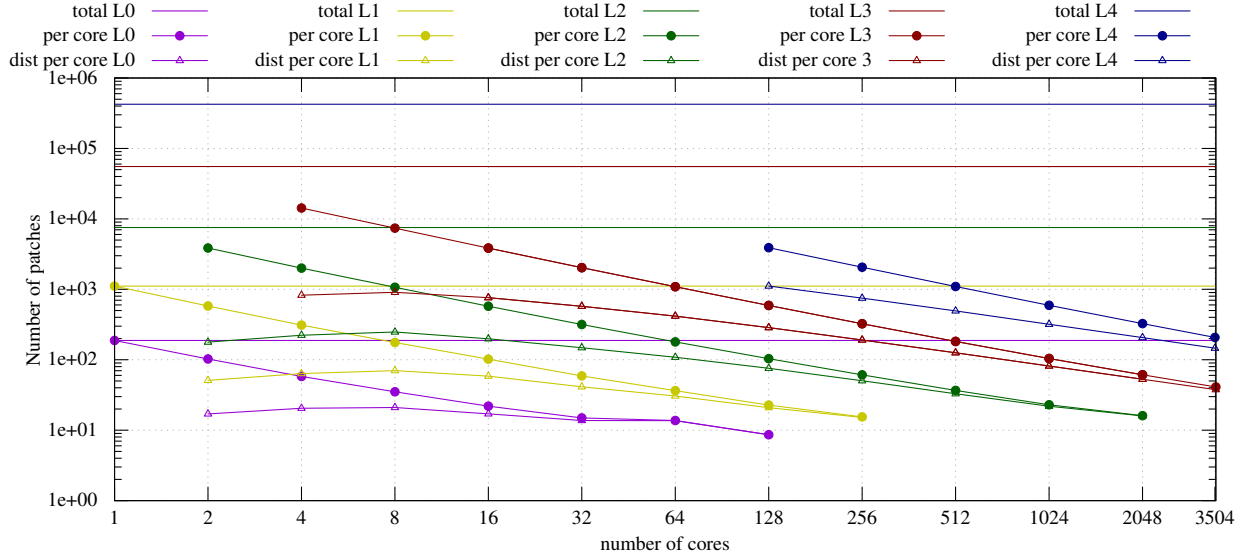


Figure 10: Cubic field: number of patches. Log/log scale..

For the super-patch refinement of level L2 (figure 8a) the two-scale solver does not provide better performance compared to the tested solvers (for "fr" and "blr", it is only with a high number of cores that the two-scale solver reaches the same level of performance of these solvers before their efficiency loss). One of the reasons is certainly that the optimal ratio of 3 cannot be reached and thus the cost of overlapping patches is not compensated by an improvement in algorithmic complexity (fine-scale problems size to small). When this ratio of 3 is reached (figure 8b), the two-scale solver starts to provide performances similar to those of other solutions. From Level 4 and above, the two-scale solver performs better than all the other solutions tested.



In figure 8d (L5), corresponding to "fr/blr"  $\sim 1.e^{+7}$  dofs (figure 9a), the potentiality of the other solver is expressed, as expected, in different ranges of number of cores. The "fr" solver provides an exact result but has a limited scalability and needs memory (the computation was not possible with less than 16 cores distributed over 16 nodes :  $16 \times 128 \text{Go} \approx 2 \text{To}$ ). The "blr" solver reduces the memory footprint and elapsed time compared to the full rank version with a controlled error ( $\varepsilon = 1.e^{-7}$ ). The "dd" solver offers good scalability but fails for a small number of processes. This is related to the choice of implementation which uses only one domain per process. Thus, for a small number of cores, the domains become very large and their resolution cannot fit in a single node of the cluster: the figure 9b shows that the average size of the domain increases to the "fr/blr" size when the number of cores decreases to 1 process. A classical alternative, not tested in this work, is to consider that the domain size is independent of the process (i.e. a process can compute more than one domain whose size is controlled by an arbitrary threshold). But the Schur complement is then potentially handled by fewer processes compared to the proposed "dd" implementation, and thus would have added additional complexity in the analyses. However, it would have been easy to compare the case where the number of dofs for domains and patches is the same. Nevertheless, with 2048 processes, the "dd" domains represent about the same number of dofs as the patches (figure 9) and the two-scale solver shows better performance in this condition. This comparison should be addressed in more detail and is left as a future prospect. As for the other solvers, with a small number of cores, the two-scale memory consumption becomes an problem (impossible computation with less than 2 process for the "from L2" version) but clearly at a lower level. This validates the choice made in the implementation regarding the per-macro-element storage (see section 3.3) and shows the low memory consumption impact of the fines scale problems. Also in figure 8d, the curves show that the proposed two-scale solver, even with a non optimal scale ratio, consistently gives better performance from 2 to 2048 processes compared to other solvers. Note also that another interesting reading of this figure 8d gives the following conclusion: with a small number of processes, the two-scale solver gives the same level of performance (i.e. elapsed time) compared to other solvers using larger number of processes.

With L6 (figure 8e, 78 851 421 fine scale dofs) and L7 (figure 8f, 627 350 205 fine scale dofs), the two-scale solver confirms its low resource requirements. The memory consumption allows to launch calculations with "only" 16 and 128 processes. For L7, no other solver passes with the chosen hardware and software configuration. And for L6 only "dd" starts to provide results with 512 cores that the two-scale solver provides with only 16 processes in the same time frame.

More detailed information about the "L6 from L3" test is given in the table 2. This table shows that the construction

	Task: elapsed time in s and % of total resolution					
Two-scale resolution	1314.4	100	67.3	100	29.6	100
<i>resi</i> computation	34.4	2.6	1.8	2.6	0.6	2.2
$\mathbf{u}_r$ update	15.9	1.2	0.6	0.9	0.2	0.6
$\mathbf{A}_{gg}$ (product,operator construction and assembly of equation 49 )	261.6	19.9	8.2	12.1	2.0	6.9
$\mathbf{B}_g$ (product and assembly of equation 53)	3.4	0.3	0.1	0.2	0.03	0.1
$\mathbf{A}_{FF}^{e_{macro}}$ (computation and assembly per macro-element)	153.3	11.7	4.9	7.3	1.2	4.1
$\mathbf{B}_F^{e_{macro}}$ (computation and assembly per macro-element)	36.1	2.7	1.1	1.7	0.3	0.9
System of equation 24 construction (sum of above)	454.4	34.6	14.3	21.3	3.5	12
nb of cores	16		512		2048	

Table 2: Detailed elapsed times of the global matrix construction, *resi* computation and  $\mathbf{u}_r$  update for some points of "tsi" L6 from L3 curve (figure 8e)

time of the global system (equation 24) represents less than 35% of the two-scale solver resolution with 16 processes. It is only 12% with 2048 processes, which can be explained by the perfect scalability of this task ( $454.4/128 \approx 3.5$ ) compared to the scalability of the two-scale solver ( $1314.4/128 \approx 10.3 < 29.6$ ). The different calculation ( $\mathbf{A}_{gg}, \mathbf{B}_g, \mathbf{A}_{FF}^{e_{macro}}$  and  $\mathbf{B}_F^{e_{macro}}$ ) have the same perfect scalability and contribute with the same ratio to the construction task. The most expensive calculation is related to the construction of  $\mathbf{A}_{gg}$  (19.9%, 12.1% and 6.9%) and in particular the product  $\mathbf{A}_{FF}^{e_{macro}} \cdot \mathbf{T}_{Fe}^{e_{macro}}$  which represents  $\sim 56\%$  of the construction of  $\mathbf{A}_{gg}$  (result not given in the table 2). It is a sparse matrix by sparse matrix product (not using the level 3 BLAS routine) performed on all SP elements at each two-scale iteration. Perhaps an effort on its implementation would allow to obtain better performances but it would be anyway only on a small part of the two-scale resolution. The performance of the global scale system construction is therefore no longer analyzed in this work (but included in the results) because it is second order in the calculations and scales perfectly. Regarding the computation of *resi*, it consistently represents less than 3% of the two-scale resolution and scales relatively (few communication) well ( $34.4/128 \approx 0.3 < 0.6$ ). This validates the proposed algorithm F.6. The same conclusion applies to the update of  $\mathbf{u}_r$  (algorithm F.4) which costs less than 1,3% and scales well ( $15.9/128 \approx 0.12 \lesssim 0.2$ ).

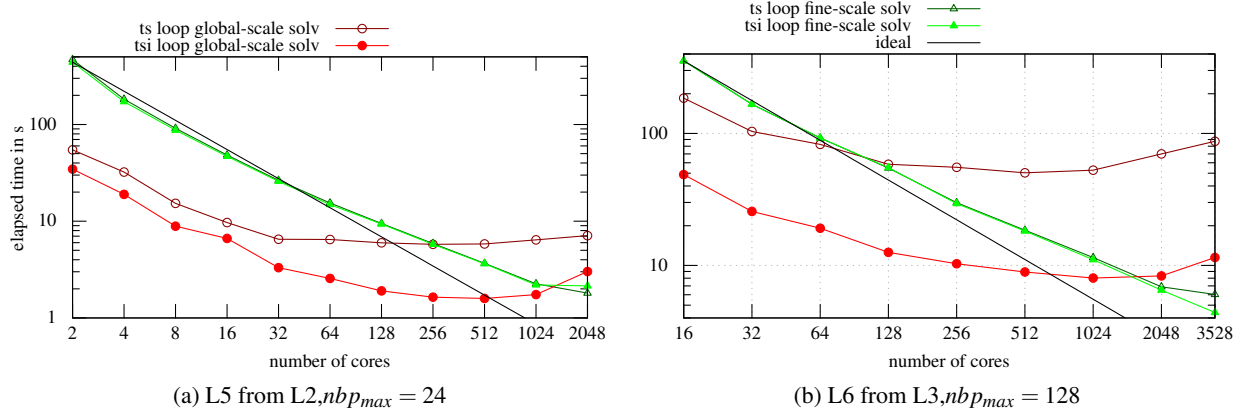


Figure 11: Cubic field: elapsed time in second of the two-scale loop resolutions (ts and tsi versions) divided in two parts: the global-scale resolution and the local-scale resolutions. Log/log scale..

The curve "fr" in figure 8 for L2,L3,L4 and L5 shows that beyond a limit, the elapsed times increase when the number of used cores increases. This justifies why, in the section 5.1, the version  $\text{Two-scale}^{gld}$  takes at most  $nbp_{max}$  processes to compute the problem at the global scale. But this has an impact on scalability. In the figure 11, for two configurations ("L5 from L2" and "L6 from L3"), the elapsed times of the scale loop resolutions are isolated and divided into global scale contribution(resolution  $\dagger$  in algorithm 1) and fine scale contribution (MICRO-SCALE\_RESOLUTION call of algorithm 1). It shows that the elapsed time of the global-scale resolution corresponding to the  $\text{Two-scale}^{gld}$  version ("ts loop global-scale solv") decreases until  $nbp_{max}$  is reached. For a larger number of processes, the elapsed time remains stable and even increases. This last point can be explained by the way the subset of  $nbp_{max}$  processes is chosen. With the current implementation, this subset follows a uniform distribution with respect to the mapping of all the processes. This ensures that problem solving spans many nodes to ensure balanced memory consumption. But this leads, with a high number of processes, to force almost all the communications of factoring and forward/backward solving, to go through the network between nodes that may be relatively far apart (in the sens of the network topology). Another parameter explaining this increase, is related to the gathering of  $\mathbf{A}_{gg}$  and  $\mathbf{B}_g$ , and the scattering of  $\mathbf{U}_g$ , from/to a large number of processes that add communication. This poor performance for a number of processes higher than  $nbp_{max}$  justifies the introduction of the  $\text{Two-scale}^{gli}$  version. Its effect is first to reduce the global-scale consumption: the "tsi loop global-scale solv" is shifted down compared to the "ts loop global-scale solv" (a factorization is replaced by some forward/backward resolution and sparse matrix multiplication per vector at some iterations). This is even more true in the case of figure 11b where the global scale level is larger than in the case of figure 11a. The second effect of this version is to maintain a decreasing slope of the "tsi loop global-scale solv" curves when using more than  $nbp_{max}$  processes. The iterative solver adds scalability. With more than 1024 processes, the elapsed time increases again for "tsi loop global-scale solv". The non-perfect scalability and this increase are again related to the choice of the  $nbp_{max}$  cores. The preconditioner uses the factorization of the direct solver to perform forward/backward resolution but only on  $nbp_{max}$  processes spread over many nodes. This limits the scalability because this part will not use more than  $nbp_{max}$  processes and, as said above, network will be more stressed. Note that with Mumps, we choose to have the solution and the right-hand side centralized on process 0 to simplify the exchange of these vectors between the  $nbp_{max}$  processes and all processes. Perhaps using the ability of MUMPS to spread the solution vector and the right-hand side vector across processes would improve the situation. But it's not clear because the vector gathering/scattering operation should still be performed, now directly, between  $nbp_{max}$  processes and all processes, but not longer collectively. In comparison, the elapsed time of the fine-scale resolution (curves "ts loop fine-scale solv" and "tsi loop fine-scale solv" in figure 11) decrease steadily and confirms a fairly good scalability of the fine-scale resolution.

Now, regarding the strong scaling efficiency<sup>9</sup> of the two-scale solver, the figure 12b shows a decrease in performance with increasing number of cores. This deterioration is mainly related to the poor performance of the global-scale as mentioned above in the analysis of the figure 11. But it is not the only reason. The strong scaling efficiency (not shown here) of "ts loop fine-scale solv" and "tsi loop fine-scale solv" in figure 11 shows that the performance remains above 50% over a wide range, but decreases. This decrease in fine-scale problem solving performance can be understood by analyzing the evolution of the number of distributed patches per process. The figure 10 shows that the number of

<sup>9</sup>Strong scaling efficiency is the ratio of speed-up to the number of processes used. It is multiplied by 100 to obtain a %. 100% implies a perfect use of resource(cores)

distributed patches per process reaches the number of patches per process when the number of processes increases. This implies that the amount of communication increases as more patches need to communicate during their resolution. This in itself has a significant impact on overall efficiency. But this also increases the number of sequences that the algorithm H.8 must process. And, because this algorithm uses a heuristic, perfect sequencing may be more difficult to achieve when almost all patches are distributed (the performance of the sequencing algorithm will be discussed in the section 6.3).

A direct comparison of the strong scaling efficiency with other solvers is possible for small problems (L2, L3, L4) where the data for one process is available for all solvers. In figure 12a and 12b, the efficiency drops below 50% when using more than 8 (L2) or 32 (L3 and L4) processes with the two-scale solver. In comparison, this 50% drop appears earlier for "dd" (4 processes) and "fr", "blr" (4 processes for L2, 8 processes for L3 and 16 processes for L4). For the other discretization level (L5, L6 and L7), the data for "one process" are missing and the first available point is therefore arbitrarily considered as perfect (100%). In these cases, only the slopes can be compared. But by using a linear fit of the curves on their regularly decreasing part, the approximate slope can be extracted ("slop" in figure 12a and 12b). This shows that the two-scale solver has lower slopes compared to "dd", "fr" and "blr". In conclusion, in all cases, the two-scale solver presents slightly better strong scaling performances than the other "solvers".

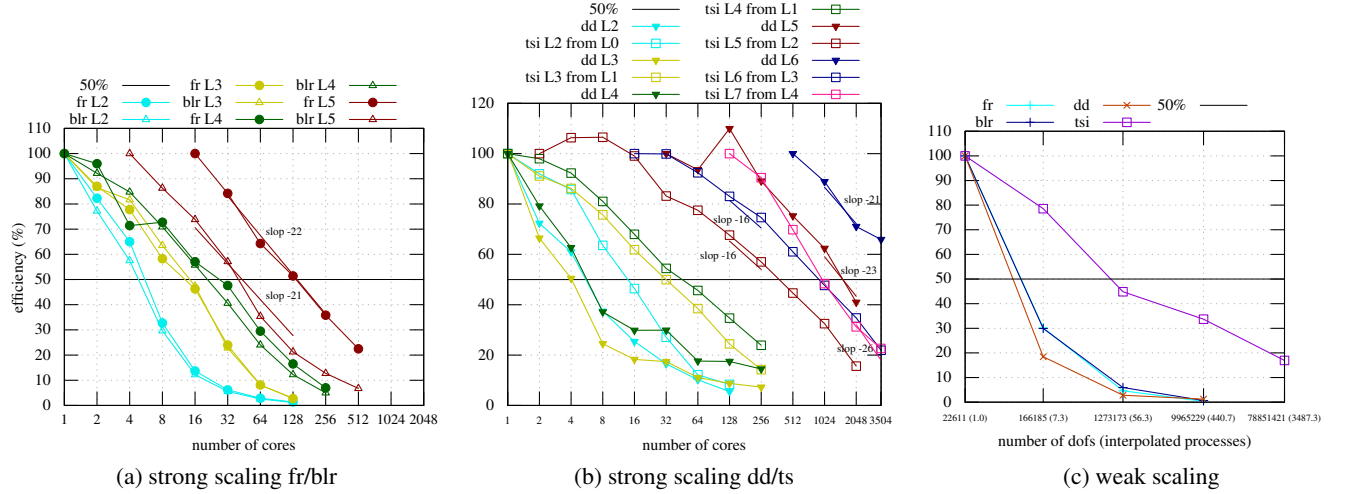


Figure 12: Cubic field: scaling efficiency. log/lin scale..

With respect to weak scaling efficiency<sup>10</sup> a full simulation campaign has not been conducted. Interpolation between the data in figures 12a and 12b is used to produce the curves in figure 12c where "tsi" uses a different coarse-scale problem size. The efficiency remain above 50% up to  $1.e^{+6}$  dofs and drops to 17% for  $7.8e^{+7}$  dofs, which in itself is positive (i.e. the efficiency does not drop below 5% immediately). Compared to other solvers, the two-scale solver offers a better efficiency. Note that for the "dd" solver, the elapsed time reference for a single process is that of "fr" because the implementation does not handle the single domain case. Thus, the weak efficiency in this case should certainly be moved up.

We now analyze the quality of the two-scale solver using the following relative errors:

$$\mathcal{E}(\mathbf{u}^{ts}, \mathbf{u}^C) = \frac{\|\mathbf{u}^{ts} - \mathbf{u}^C\|_{E_\Omega}}{\|\mathbf{u}^C\|_{E_\Omega}} \text{ and } \mathcal{E}(\mathbf{u}^{ts}, \mathbf{u}^R) = \frac{\|\mathbf{u}^{ts} - \mathbf{u}^R\|_{E_\Omega}}{\|\mathbf{u}^R\|_{E_\Omega}} \quad (37)$$

where  $\mathbf{u}^C$  is the analytical solution given by (36) (equivalent to the continuous solution of the section 3.2) and  $\mathbf{u}^R$  is the reference solution given by solving of (13) with an auxiliary computation ("fr" or "dd" with  $\varepsilon = 10^{-13}$ ). Figure 13 shows in the left graph  $\mathcal{E}(\mathbf{u}^{ts}, \mathbf{u}^C)$ , in the right graph  $\mathcal{E}(\mathbf{u}^{ts}, \mathbf{u}^R)$  and in the central graph the residual error  $\frac{\|\mathbf{A}_{rr} \cdot \mathbf{u}_r - \mathbf{B}_r\|}{\|\mathbf{B}_r\|}$  (*resi*) provided by the algorithm F.6. These graphs show the evolution of the error with respect to the

<sup>10</sup>For a problem of size  $N$ , the weak scaling efficiency is the ratio of the time used by an application to solve a problem in single-process mode divided by the time used in multi-process mode (with  $nbp$  processes) to solve a problem of size  $nbp \times N$ . It is multiply by 100 to obtain a %. 100% implies perfect use of the resource(cores)

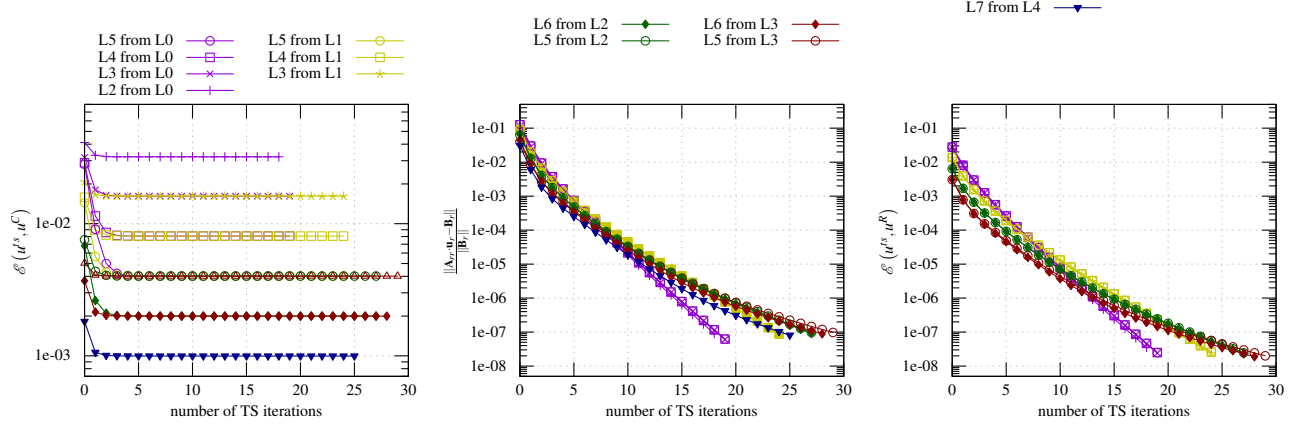


Figure 13: Cubic field: errors .

two-scale iterations. The equation (20) is verified numerically with these curves. This explains why, as  $\mathcal{E}(u^s, u^R)$  tends towards zero in all cases,  $\mathcal{E}(u^s, u^C)$  decreases to a constant value which corresponds to the discretization error  $\|u^R - u^C\|_{E_\Omega} / \|u^C\|_{E_\Omega}$ . As the fine-scale discretization increases, this constant naturally decrease. But in all cases, only a few iterations make  $\mathcal{E}(u^s, u^C)$  close to the discretization error. This confirms the same observation made in the literature that the error on the boundary conditions of fine scale problems decreases rapidly with respect to  $\|u^R - u^C\|_{E_\Omega}$ . The proposed two-scale solver behaves in the same way, regardless of the number of processes used (there is no side effect introduced by parallelism). In these graphs, we can see that the  $\mathcal{E}(u^s, u^R)$  error, corresponding mainly to the error on the boundary condition of fine-scale problems, evolves in a similar way to the residual error. For  $\varepsilon = 1.e^{-7}$ , the  $\mathcal{E}(u^s, u^R)$  error is below this threshold a few iterations before the residual error. Thus, this last criterion is conservative: when it is respected, it ensures that  $\mathcal{E}(u^s, u^R)$  is respected. We can also observe that the curves, whether for the residual or for  $\mathcal{E}(u^s, u^R)$  error, are almost the same for a given coarse-mesh discretization. In particular L2, L3, L4 and L5 "from L0" are very close. This is also the case for the curves "from L1" and "from L2". For the "from L3", a small gap appears between L5 and L6. After a few iterations of the scale loop, the curves behave almost linearly (in linear/logarithmic scale) with a softening of the slopes when at the global-scale the discretization grows. These observations, which still need to be analyzed theoretically, show that  $\mathcal{E}(u^s, u^R)$  and  $resi$  are influenced by the level of discretization on the global-scale. But the next test case will already give us a more refined interpretation of these observations.

This last part studies the choice of  $\varepsilon = 1.e^{-7}$ . From the graph of  $\mathcal{E}(u^s, u^C)$ , after a few iterations there is no real interest in continuing the scale loop because the precision is clearly imposed by  $\|u^R - u^C\|_{E_\Omega}$ . A relative error with respect to this quantity may be satisfactory in some calculation contexts. To evaluate the impact of such a looser error condition, some tests are performed with an arbitrary residual error precision:  $\varepsilon = \frac{\mathcal{E}(u^R, u^C)}{10}$ . As mentioned above, the residual error is conservative so if it is less than  $\varepsilon$  then  $\mathcal{E}(u^s, u^R)$  is too. This leads to the following condition:

$$\mathcal{E}(u^s, u^R) \leq \frac{\mathcal{E}(u^R, u^C)}{10} \quad (38)$$

Passing at power of 2 and using equation (20) the overall error in such condition will respect the following condition:

$$\mathcal{E}(u^s, u^C)^2 \leq \left(1 + \frac{\|u^R\|_{E_\Omega}^2}{100 \times \|u^C\|_{E_\Omega}^2}\right) \times \mathcal{E}(u^R, u^C)^2 \quad (39)$$

And the relative error between  $\mathcal{E}(u^s, u^C)$  and  $\mathcal{E}(u^R, u^C)$  is then limited by:

$$\frac{\mathcal{E}(u^s, u^C) - \mathcal{E}(u^R, u^C)}{\mathcal{E}(u^R, u^C)} \leq \sqrt{1 + \frac{\|u^R\|_{E_\Omega}^2}{100 \times \|u^C\|_{E_\Omega}^2}} - 1 \quad (40)$$

Thus, numerically, the arbitrarily chosen  $\varepsilon$  leads to less than 0.5% relative error between  $\mathcal{E}(u^s, u^C)$  and  $\mathcal{E}(u^R, u^C)$  using 0.9998 for  $\|u^R\|_{E_\Omega}^2 / \|u^C\|_{E_\Omega}^2$  (average of data L3, L4 and L5). The elapsed time performance for  $\varepsilon = \frac{\mathcal{E}(u^R, u^C)}{10}$

are presented in figure 14 as a ratio of the elapsed time for the current solver to the best elapsed time among all solutions and all  $\varepsilon$ . For the three fine-scale discretizations tested, L2, L5 and L6, in addition to  $\varepsilon = 1.e^{-7}$ , the tested

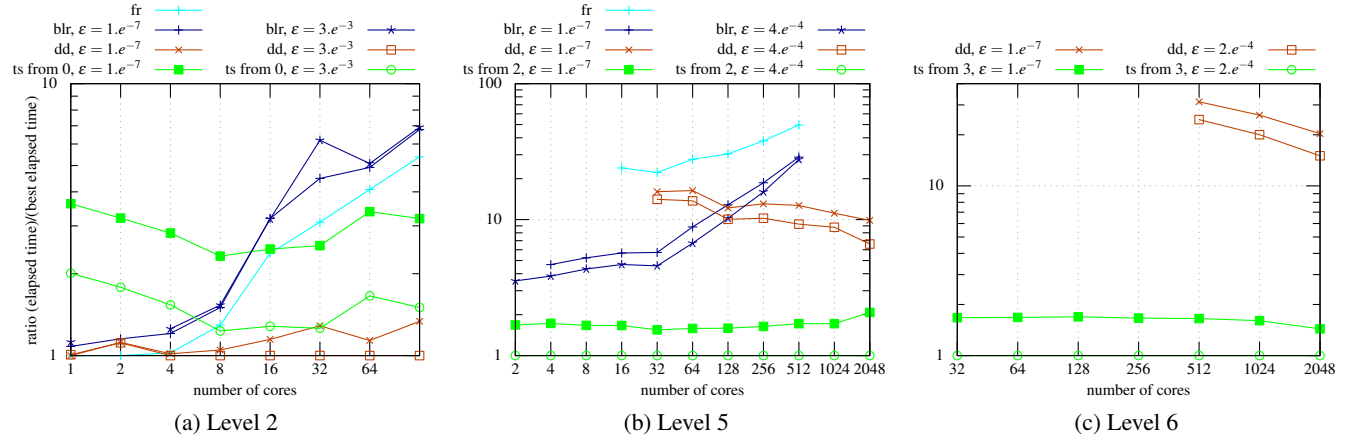


Figure 14: Accuracy impact: ratio indicating how much slower the solver associate with a curve is compared to the best solver (based on elapsed time) .

values of  $\varepsilon$  are  $3.e^{-3}$ ,  $4.e^{-4}$  and  $2.e^{-4}$  respectively. For all discretizations, a larger  $\varepsilon$  reduces the computation time of all solutions depending on it.

For L5 and L6 (figure 14b and 14c), the best solution is the two-scale solver with a larger  $\varepsilon$ . The other solvers, even if some gains are observed with larger  $\varepsilon$ , do not provide better performances than two-scale solver. For the "blr" solver, the gain in the factorization step due to the decrease in accuracy is partially lost by a larger number of iterations in the resolution of the conjugate gradient. For the "dd" solver, the gain due to decrease in accuracy is in the conjugate gradient resolution of the global boundary problem. With large domains, this task represents about 50% of the "dd" time consumed, so the gains are moderate. As the number of cores increases, this task takes most of the time ( 97% for L5 with 2048 processes) and the gains increase slightly. For the two-scale solver, the decrease in accuracy reduces the number of iterations of the scale loop. For L5 with 32, 128 and 2048 processes this task represents respectively about 46%, 51% and 66% of the time consumed which explains a moderate gain (less than 2). For L2 (figure 14a), the gain obtained with the two-scale solver is more consistent compared to the other solvers but is not sufficient for this solver to show the best performance.

## 6.2 Micro structural test case

This example illustrates the cases where matrix conditioning can be a problem for a conventional iterative solver which then needs good preconditioners. A cube (with opposite diagonal corners at the following coordinates: (0,0,0) and (2,2,2); unit: m) is randomly divided by 64 plans of different orientation and origin (see J). In the cube, each sub-region delimited by plans has a specific and uniform E. These Young's moduli, which follow an arbitrary internal encoding, range from 36.5GPa to 3650GPa. The coding makes the distribution of materials relatively random, as illustrated in figure 15.

In this test case, with the two-scale solver, all coarse nodes are enriched ( $card(e) = card(c)$ ). Thus, after choosing a fine-scale discretization arbitrarily considered to meet our micro-structure representation needs, we consider a coarse-scale discretization that follows the equation (35) (note that the coarse mesh is slightly adapted to the plane positions. This can be seen in the figure 15d where the visible left corner has larger element sizes, because no plane cuts this region). The resulting fine-scale discretization has 60 278 925 dofs and corresponds to a section 6.1 problem between L5 and L6 (figure 9a). This cube is compressed in all directions by the same constant load (4MN) applied on all surfaces. As in the section 6.1, the two-scale loop starts with the displacement field of the macro problem without enrichment and the stopping criterion for the iterations is  $\varepsilon = 1e^{-7}$ . The two-scale solver (Two-scale<sup>gli</sup> version) is again compared with the "dd" solver. This first simulation gives after 93 two-scale iterations the fields presented in the figure 16 with the solution of "dd". Note that the creation of post-processing files based on R-set dofs, obtained in parallel using MPI-IO functions, uses the per-macro-element organization of data described in the section 3.3 and thus can be further parallelized using multi-threading. As with the displacement field, we can obtain the strains from the R-set solution, as shown in figure 16d, again by looping over the macro-elements using  $\mathbf{u}_F^{e_{macro}}$ .



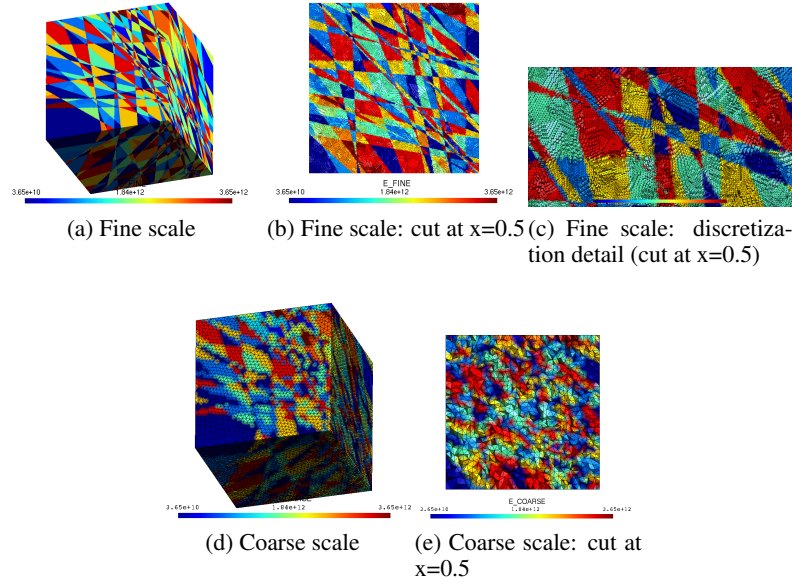


Figure 15: Micro-structure discretization and Young's modulus values (in Pa).

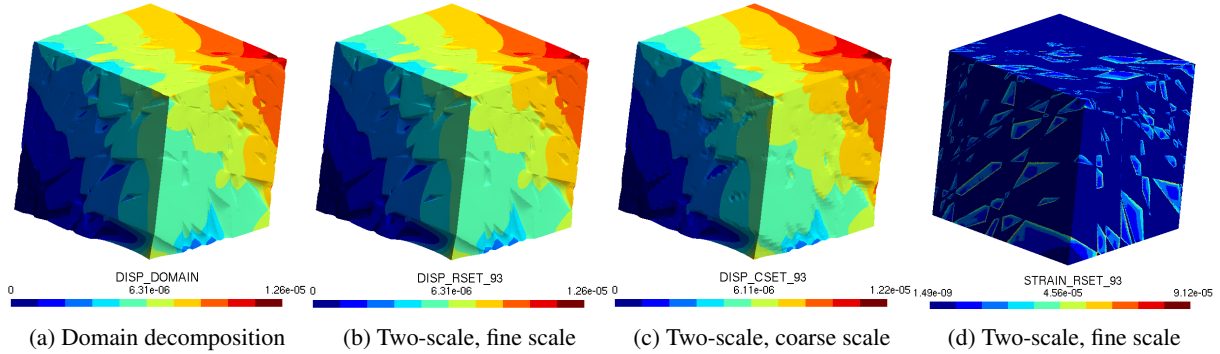


Figure 16: Micro-structure solutions: Displacement field with the "dd" solver (a). Displacement (b,c) / strain (d) field at iteration 93 with the two-scale solver. The two-scale solver can give the displacement field at both scales. At the coarse-scale (c), only the dofs in the C-set are used for post-processing, giving a crude visualization on the macro-element. At the fine-scale (b), using the R-set dofs, all details are given and can be compared to the solution obtained with the "dd" solver (a).

The elapsed times for this first computation are given in the figure 17a. It shows that, as in the equivalent test case of section 6.1, the two-scale solver provides better performance compared to the "dd" solver. The strong scaling efficiency curves (not presented here) show that the two-scale solver also has a smaller slope than the "dd" solver.

Let us now consider a broader application framework and imagine that this problem is the subject of a micro-structure optimization study with respect to a displacement field based objective. In this case, many calculations from a given set of parameters must be performed to obtain sensitivities and/or new configurations. To mimic such a case, the Young's modulus values are randomly perturbed by  $\pm 1\%$  and the computation starts from the first result obtained above. For the two-scale solver, this implies to use the r-set solution of the previous calculation, to redo the factorization of the fine-scale problems and to enter the scale loop. For the "dd" solver, the domains are condensed again, the preconditioners recomputed, and since the Schur complement relies on the same space, the iterative solver starts from the previous boundary problem solution. Figure 17b shows the performance for this second computation ("tsi (var 1%)" and "dd (var 1%)" for the two-scale and domain decomposition solvers respectively). In figure 17c, the relative performance of the two computations is presented as a ratio of the elapsed time of one computation to the best elapsed time among all computations and solvers. The two-scale solver has a reduced elapsed time because it iterated only 37

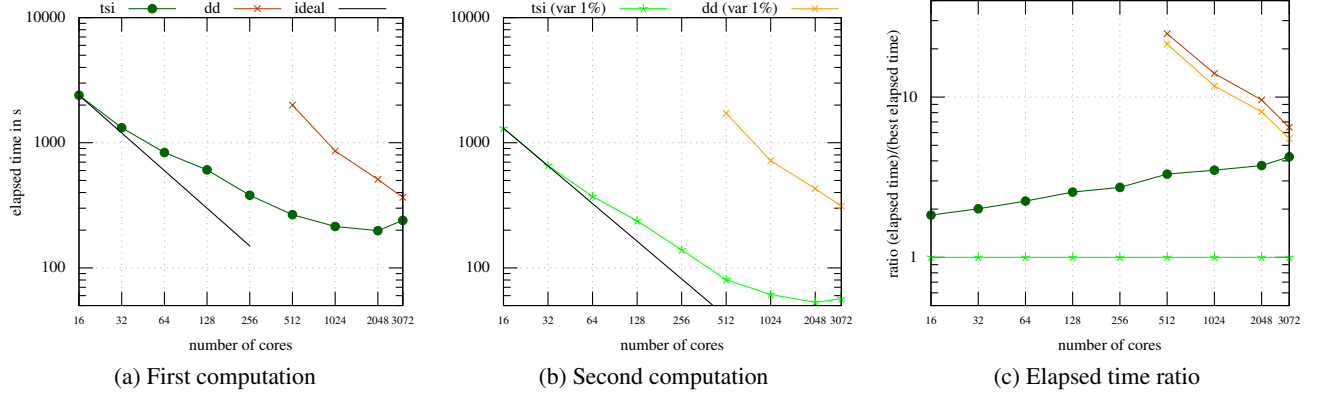
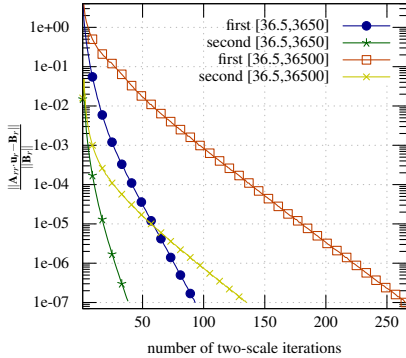


Figure 17: Micro structural performances: Elapsed time and performance ration for the first and second computation..

times, compared to 93 times for the initial calculation. This can be explained by the fact that the initial solution for this computation is already of better quality than what the unenriched coarse field can give ( $resi = 1.5e^{-2}$  compare to  $resi = 1.6$  for the first computation) even if the Young's moduli have changed. Moreover, the local variation of  $E$  may only influence the modulus and not the shape of the enrichment functions. But starting from a better solution also reduces the number of two-scale iterations where the full rank solver is used at the coarse scale. In the first computation  $resi < \varepsilon \times 10000$  (rule from section 5.1) is met after 25 iterations. For the second computation, this condition is met only after 4 iterations. This explains why the ratio of "ts" in figure 17c grows with the number of processes: as already observed in the analysis of figure 11, when a high number of cores is reached, the reduced set of  $nbp_{max}$  processes has a negative impact on the factorization performance. Thus, this poor performance has an impact only 4 times on the second computation against 25 times for the first. For the "dd" solver, restarting from the previous global boundary solution reduces the number of iterations in solving the global problem but not enough to significantly decrease elapsed time. The second "dd" computation cost almost the same as the first one, which gives an advantage to two-scale solver in this case.

To obtain an even worse conditioned system, exactly the same scenario is replayed with a wider range of  $E$  values: from 36.5 GPa to 36500 GPa (maximum ten times larger than previous one). Results with 2048 cores and both ranges, are given in the table 18b. With the new  $E$ -range, the number of two-scale iterations for the first computation (the one



(a) Curves

E (GPa)	run	two-scale			dd	
		nb of iterations		time (s)	nb of iterations	time (s)
		all	$resi \geq 10^{-3}$			
[36.5,3650]	first	93	25	198.6	1868	509.9
	second	37	4	53.1	1487	429.8
[36.5,36500]	first	265	96	691.4	2191	621.4
	second	134	7	128.8	1487	519.4
E (GPa)	run	all	$resi \geq 10^{-1}$	time (s)		
[36.5,36500]	first	265	27	452.8		
	second	134	0	149.4		

(b) table

Figure 18: With 2048 cores, comparison of the first and second micro-structure calculations with different Young's modulus ranges."nb of iterations" is the number of iteration of the loop of the algorithm 1 and L.12. "time" is the elapsed time to solve the problem.

starting from the coarse unenriched solution) increases from 93 to 265. This increase is related to a worse starting point and conditioning, which degraded the residual convergence rate, as can be seen in figure 18a. In this figure, the slope (after a few iterations) of the first computation with a smaller  $E$ -range (thus with better matrix conditioning) is stronger than that of the first computation with a larger  $E$ -range (thus with worse matrix conditioning). This is confirmed by the second calculation where the curves start with a smaller residual error but have the same slope as their counterpart

in the first calculation. This brings explanations to the observation made in section 6.1 where a finer discretization of the problem at the global scale gives a slower residual convergence (see the slopes of the curves in figure 13). In fact, we can now add that it is the conditioning of the global matrix (related to the level of discretization) that has an impact on the convergence.

Regarding performance, like the two-scale solver, the "dd" solver needs more iterations to converge (the worse conditioning is not fully corrected by domain condensation). For first calculation, "dd" needs 2191 iterations with the new E-range against 1868 with the original E-range. The elapsed time is moderately impacted and increase to 621.4s from 509.9s. The second calculation proceeds in the same way and there is a moderate gain starting with the first calculation (for both E-range). For two-scale solver, this increasing number of iterations has a greater impact on the first calculation. The elapsed time goes from 198.6s to 691.4s which gives an advantage to "dd" in this case. This increase in time is in fact closely related to the number of iterations where the global problem is computed by the full rank solver. With Two-scale<sup>gli</sup> version, the iterative resolution is activated when  $resi < \varepsilon \times 1000$  (rule of the section 5.1) and with  $\varepsilon = 1e^{-7}$  the condition is  $resi < 1e^{-3}$ . The table 18b gives the number of iterations that do not meet this condition and therefore only correspond to a full rank resolution. For the first calculation, 96 iterations are performed in full rank mode with the new E-range compared to 25. If we change the condition to  $resi < 0.1$ , only 27 iterations are spent in full rank mode and the elapsed time drops to 452.8s which is now better than "dd". This shows that the Two-scale<sup>gli</sup> setting can be improved in some cases. But even with this new setting, some computations not reported here, with a larger E-range, shows that the two-scale solver is in trouble compared to "dd" when the matrix conditioning degrades further. In all cases, the second calculation with the two-scale solver, with both settings and both E-ranges, has a better elapsed time than the first calculation. This confirms the interest of using the two-scale solver when a history can be kept from one computation to another.

### 6.3 Pull-out test case

This test case is inspired by the crack propagation simulation studied in [8, 25, 10, 5]. It represents the pull-out of a steel anchor embedded in an unreinforced concrete ( $E=26.4\text{GPa}$ ,  $\nu=0.193$ ) cylinder. The chosen geometry and boundary conditions used in this test are given in figure 19. The steel anchor, not shown in this figure, is located in the

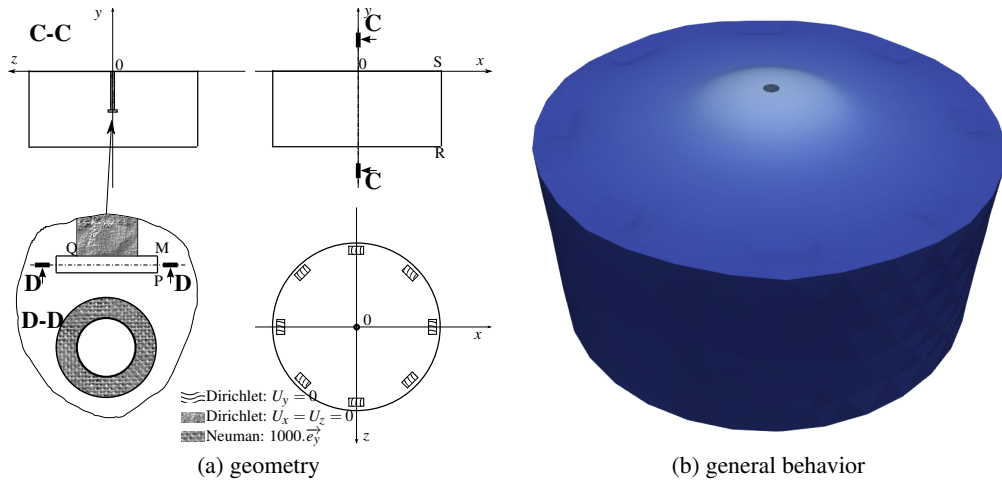


Figure 19: Pull-out test case geometry, boundary conditions and general behavior (obtained by one simulation of this section):

$M(0,-450,-60), P(0,-470,-60), Q(0,-450,36), R(1000,-900,0), S(1000,0,0)$  unit=mm

hollowing out in the center of the disk and is pulled in the  $\vec{e}_y$  direction. Its action is simply modeled as a force applied to the contact surface between the compression surface of the anchor head and the concrete. Other interactions of the anchor with the concrete are simplified because contact, decohesion or other mechanical bond phenomena are beyond the scope of this study. Thus, all remaining surfaces of the anchor head are considered to have no interaction with the concrete which is left as free surfaces in these areas. The surface of the anchor body is considered to impose a sliding contact interface along the  $\vec{e}_y$  axis.



The crack is represented by a damage field  $d$ . The behavior of the material thus follows the linear elastic damage potential  $\varphi(\varepsilon, d)$  which is written, using the Hooke tensor  $\mathbb{C}$ , as follows:

$$\varphi(\varepsilon, d) = \frac{1}{2}(1-d)\varepsilon : \mathbb{C} : \varepsilon \quad (41)$$

When  $d = 1$ , the material has lost all its rigidity and can be considered as a crack. In the pull-out test, the crack starts under the head of the anchor and develops at a specific angle in the form of a cone. The more you pull on the steel anchor, the more the crack continues to grow in a cone. The classic scenario for simulating such evolutionary phenomena is to use mesh adaptation to follow the movement of the crack front so that the damaged area is always entirely within a finer mesh region. By always refining a little ahead of the front, the number of mesh adaptations can be limited, keeping the same mesh for a few evolutionary iterations called step below. To study such a scenario with the two-scale method, we consider three arbitrary evolution stages that correspond to three coarse mesh adaptations. And for each of them, four fictitious steps advance the crack front evenly according to the cone angle in the adapted fixed mesh. The damage field is calculated by considering the conical envelope described in K with the parameter  $h$  in (61) controlling the crack cone size. The coarse mesh is adapted for  $h = -400$  (50 874 c-set dofs),  $h = -300$  (119 829 c-set dofs) and  $h = -100$  (362 904 c-set dofs) considering that  $h$  during the steps will fluctuate between  $[-410, -400]$ ,  $[-310, -300]$  and  $[-110, -100]$  respectively. The mesh sizes of the fine problems follow the equation (35). This corresponds approximately to 4, 16 and 58.6 million r-set dofs for the  $h = -400$ ,  $h = -300$  and  $h = -100$  stages respectively. The super-patch is built at each stage to cover only the damaged area during the 4 evolutionary iterations as shown in figure 20. So, in this test case, there are NSP elements and transition patches (the one with

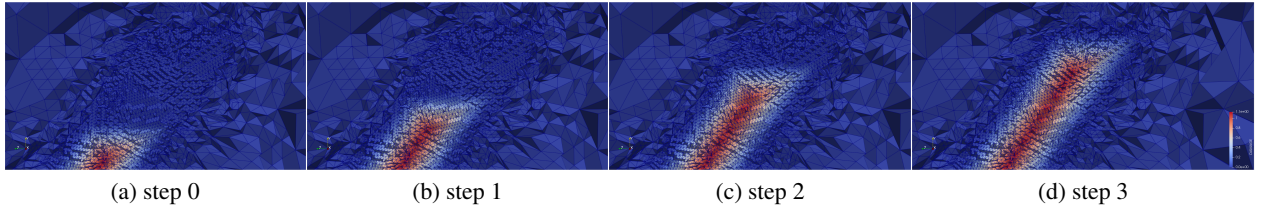


Figure 20: Evolution of the imposed damage field for the  $h = -400$  adaptation. Cross-section of the SP. Zoom of the crack front (with a rather unrealistic shape as mentioned in K).

hanging node treatment). The two-scale resolution is performed 4 times. The first one starts from a zero displacement field (in a real simulation, it would be a displacement field obtained by projection of the result of the last step of the last stage). The next three two-scale resolutions will start with the displacement field calculated in the previous iteration. Here, since the super-patch discretization remains the same, the displacement fields at both scales are on a stable space. Only some patches need to be re-factored to account for material degradation related to damage propagation. The precision chosen, as in the other test cases, is  $\varepsilon = 1.e^{-7}$ .

The displacement results of the two-scale solver, obtained at both scales for all stages, are shown in figure 21. The displacements field are presented on the coarse mesh (using only C-set dofs) and on the SP fine discretization (F-set dofs). Figure 21d, 21e and 21f show at each adaptation the region covered by the SP. At the crack, we can see distorted elements confirming the correct displacement jump introduced by the fully damaged material. This jump is also evident in the clear separation of colors between the cone that is torn off and the rest of the disk that hardly moves. This is even clearer in figures 21a, 21b and 21c where the crack appears in context of the complete disk. The pulled out cone becomes more and more visible as the damage grows. These results, confirmed by simulation with other solvers, fully validate the proposed two-scale implementation (in particular the treatment of the hanging nodes (section 3.2) and the enrichment of mixed patch (figure 3)).

The two-scale solver (the Two-scale<sup>gli</sup> version) is again compared to the "fr", "blr" and "dd" solvers. The cumulative elapsed times of the different steps (per adaptation) give the performance curves shown in the figure 22. For "fr" and "blr" it is simply 4 times almost the same cost (mainly factoring and solving, the symbolic phase being done only once). But for "dd" and "tsi", each execution, after the first one, starts from the previous one and gains iterations in their looping part. For "dd" only the first step requires iterating in the conjugate gradient to solve the global boundary problem. The other steps just enter the loop of the algorithm L.13 once and stop. They cost less than the first step (almost only the condensation and preconditionner are updated and do count, but both depends only on the domain size). For "tsi", the restart process reduces the number of scale iterations as can be seen in figure 23 by starting with a solution with smaller residual error. As the crack grows, the matrix conditioning decreases, and we can again observe that the rate of convergence of the residual error decreases (figure 23d).

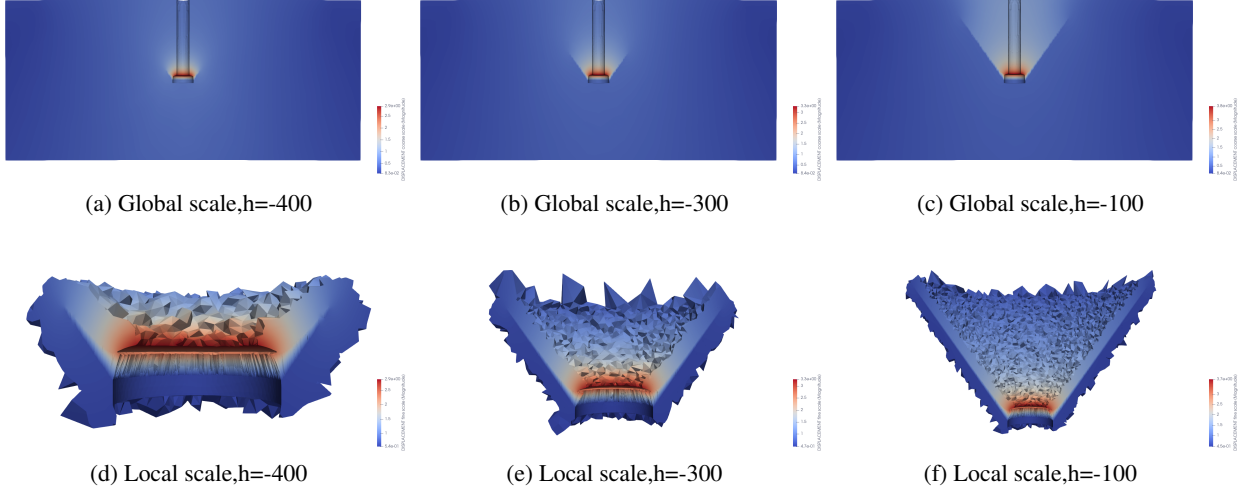


Figure 21: Displacement field for  $h=-400$ ,  $h=-300$  and  $h=-100$ . Cross-section of the SP discretization and the coarse mesh. Displacement multiplied by 10.

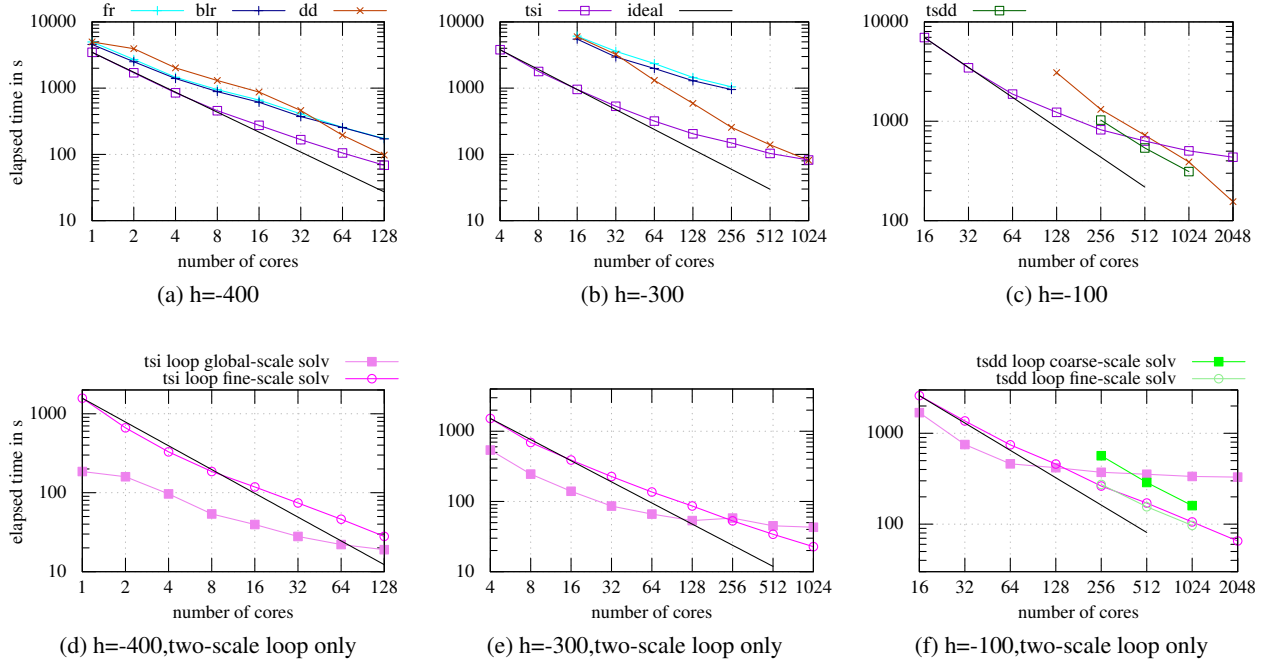


Figure 22: Accumulation over the 4 steps for each adaptation of the elapsed time in second. For the full computation in (a,b,c) and only for the two-scale loop in (d,e,f). Log/log scale..

As in the other test cases, the two-scale solver provides consistent performance for all numbers of cores tested. Only the "dd" solver achieves equal or better performance when used with a high number of processes. This decrease in scalability is due, when using many cores, on the one hand to the low number of patches per process and the high number of distributed patches and on the other hand to the low scalability of the coarse-scale resolution (even with the use of the Two-scale<sup>gli</sup> version). This can be seen in figures 22d, 22e and 22f where the times spent in the two-scale loop to solve the fine-scale problems ("loop fine-scale solv") and the global-scale problem ("loop global-scale solv") are shown. We can observe the drop in scalability when reaching  $nbp_{max}$  processes (see section 5.1) with the coarse scale resolution. To prove that this last point, if addressed, can significantly improve the scalability of the two-scale

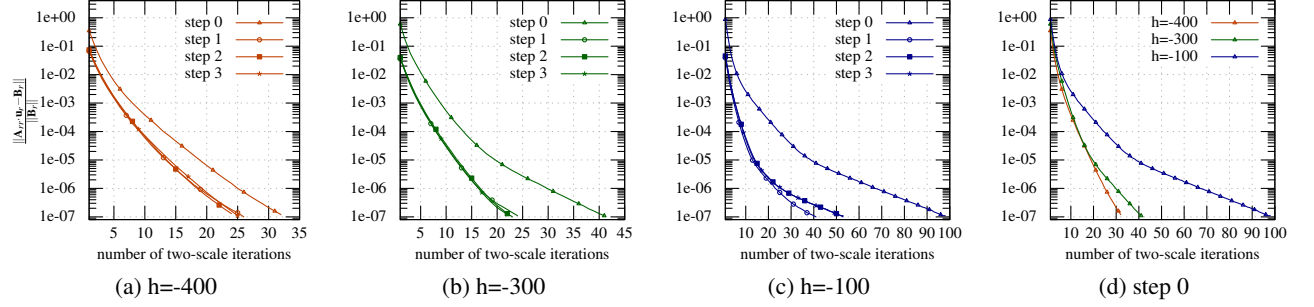


Figure 23: Convergence of residual errors for the 3 adaptation stages and associated steps. Lin/Log scale.

solver, a new two-scale version ("tsdd" hereafter) has been implemented with the domain decomposition solver of  $L$  used at the coarse scale level ( $\dagger$  of algorithm 1). This change brings the scalability of the "dd" solver to the coarse scale. And by always using the last solution of the global boundary problem (at coarse scale) as the starting point for the "dd" conjugate gradient resolution (algorithm L.12), the evolutionary aspect of the simulation is now taken into account in coarse scale resolution. In addition, during the two-scale loop, restarting from the previous solution of the global boundary problem also reduces the number of iterations of the conjugate gradient. The iteration gains appears in the figure 24. Note the oscillation that appears for step 0 around the 35th iteration just as the residual curve in the figure 23c stabilizes on another slope. This must be understood in a future work on the subject. This new "tsdd" version gives, as expected, better results (see figure 22c) since the use of the "dd" solver at coarse scale is more efficient than a direct/iterative resolution as can be seen in 22f. The slope at both scales is correct, giving a nice overall slope for the "tsdd" solver. This proves, that any solver that scales well to a large number of cores and benefits from iterative context resolution will be a good candidate to solve large coarse-scale problem. It is natural to think of the two-scale distributed solver for this, as it can provide such capabilities, as has been proven in this work. This is left as a future prospect.

Since the patches do not have the same "weight", the local problem scheduling proposed in section 5.2 can be fully validated by this test case. In table 3 tree variants of the algorithms H.8, H.11, H.9 and H.10, called V0, V1 and V2, are tested for  $h=-300$  and  $h=-100$  with 64 and 512 processes.

The V0 version corresponds to the algorithms H.8, H.9 and H.10 where the weight is not used:  $\mathcal{D}$  and  $\mathcal{L}$  are not sorted,  $mxwg$  and  $mxwl$  are not calculated or used, the first available patch in the group is selected (i.e. the one with a "random" weight that depends only on how the patches were constructed). The V1 version uses the descending weight ordered groups  $\mathcal{D}$  and  $\mathcal{L}$  but does not use or compute  $mxwg$  and  $mxwl$ . The first available patch in the group is selected (i.e. the one with the highest weight). The V2 version corresponds to the proposed algorithms H.8, H.9 and H.10. To compare these versions, a metric called "observed cost per process" counts the elapsed time (averaged over 3 runs) per process related to all tasks connected with distributed patch sequencing (i.e. all creations, factorizations, and resolutions of all patches for all two-scale iterations and steps). The mean and standard deviation of this metric, for all processes, are given in absolute value and relative to the V2 performance. The V0 and V1 versions are 3.7% to 8.1% and 8.4% to 14.4% slower than the V2 version, respectively, in terms of average performance. Surprisingly, the "random" V0 version is not the worst. Certainly because during construction, the groups were built in a favorable order by chance. The standard deviation of this measure reflects the load imbalance introduced by the sequencing algorithm and the coarse mesh distribution. Between V0,V1 and V2, only the sequencing varies and the coarse mesh distribution remain the same. Thus, the variation in standard deviation from V2 somewhat reflects the load imbalance added by V0 and V1, which are 24.9% to 38.3% and 59.3% to 97.0% more dispersed than the V2 version, respectively. In any case, the V2 version is the one that also provides the smallest (or equal) number of sequences compared to the V0 and V1 versions. These numbers of sequences are as expected higher but close to the average number of distributed patches per process. All these observations validate the choice of V2 as the best version to use in this paper among V0,V1 and V2.

Also note that this test case validates the enrichment function and the processing of hanging nodes in patches with a mixture of refined and unrefined elements. Some test not presented here confirm that these choices give the best two-scale convergence compared to some truncated patch solutions.

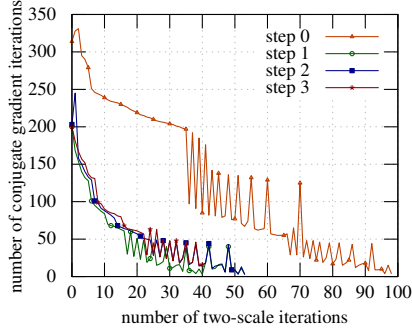


Figure 24: Number of iterations for solving the "dd" conjugate gradient at the coarse scale ("tsdd" version) for  $h=100$  with 1024 cores..

		$h=300$	$h=100$	$h=100$
V0	Number of processes	64	64	512
	Total number of patches	26609	94388	94388
	Min number of patches per process	456	1457	225
	Max number of patches per process	610	1802	316
	Average number of patches per process	535.5	1702.1	272.6
	Average number of distributed patches per process	226.6	442.1	160.4
	Number of sequence	303.3	586.3	221.3
	Average observed cost per process	elapsed time (s)	158.4	908.7
		vs V2 (%)	8.1	3.7
	Observed cost standard deviation	in s	12.6	57.0
		vs V2 (%)	24.9	38.3
V1	Number of sequence	301.3	591.7	216.7
	Average observed cost per process	elapsed time (s)	167.7	986.1
		vs V2 (%)	14.4	12.5
	Observed cost standard deviation	in s	17.0	81.2
		vs V2 (%)	68.4	97.0
	Number of sequence	303.3	580.0	213.7
V2	Average observed cost per process	elapsed time (s)	146.5	876.4
	Observed cost standard deviation	in s	10.1	41.2

Table 3: Comparison of distributed patches sequencing algorithms. V2 corresponds to the algorithm H.8, H.11, H.9 and H.10. V0 corresponds to the algorithm H.8, H.9 and H.10 without taking into account the weight (The  $\mathcal{D}$  and  $\mathcal{L}$  are not sorted, the  $mxwg$  and  $mxwl$  are not computed nor used, the first available patch in these groups is selected). V1 corresponds to the algorithm H.8, H.9 and H.10 with a patch selection, neither using nor computing,  $mxwg$  and  $mxwl$  (the first available patch in the group is selected). The results given are the average values of 3 runs with the same parameters. The observed cost corresponds to the creation, factoring and resolution of all patches for all two-scale iterations and steps.

## 7 Conclusions

This work introduces some novelties in the original GFEM<sup>gl</sup> method:

- a new criterion to control the iterations of the two-scale resolution loop;
- a efficient algebraic computation of the matrices of linear systems at both scales;
- the use for the enrichment of a linearly interpolated function (with a shift);
- the treatment of blending element problem with the use of additional enriched nodes corresponding to mixed discretization patches;
- a distributed implementation of the two-scale method;
- a new algorithm for scheduling the computation of fine-scale problems;
- a proof given in sequential that there is an optimal scale jump (confirmed in parallel);
- the use of specific resolution (Two-scale<sup>gld</sup>, Two-scale<sup>gli</sup>, iterative domain decomposition solver) at global level to improve scalability of this scale.

These new features improve the capability of the two-scale method in several ways. The new stopping criterion is comparable to the error (in energy norm) of the boundary condition imposed on the fine-scale problem. It thus allows to obtain results with a given precision. And when used by the two-scale solver in evolutionary phenomena (where the resolution starts from a close previous solution) the number of two-scale iterations can be considerably reduced.

With respect to performance, the proposed distributed implementation is promising and performs efficiently compared to some other parallel solvers for a wide range of used cores. In particular, it allows, with few cores, to handle larger problems than with the other solvers tested. Parallelism at both scales is clearly to be maintained, but some elements still need to be improved (at global scale in particular). The scalability of local scale is correct thanks to, among other things, the new scheduling of the local scale problems.

Now, in terms of future works, parallel performance and the use of the new criterion are two topics that can be explored further. The proposed new residual error criterion has already given valuable insights into the convergence of the two-scale solver. In particular, this allowed to highlight the influence of the matrix conditioning of the system at the global scale on the convergence. A full analysis of this observation should be done to get a theoretical confirmation. Regarding enrichment, a closer comparison with SGFEM and other enrichment techniques could also be conducted in a future work in a quantitative way, thanks to this new convergence criterion.

Otherwise, for parallel performance, when the global problem becomes large, both solutions, Two-scale<sup>gli</sup> and iterative domain decomposition solver, exploited the fact that between two-scale iterations, at the global scale, the linear system evolves relatively slowly. Therefore, the iterative resolution of this type of problem can gain in performance by using the previous computed solution. This lead to the conclusion that any solver that scales well over a wide range of cores numbers and that takes advantage of an iterative context in its computation will be a good candidate for solving large coarse scale problem. And of course, the two-scale solver itself can be used for this. But many questions need to be answered before embarking on such a process. Would we act independently, with one two-scale solver solving the large problem at the coarse scale of another two-scale solver at each of its iterations? Or should we just do some "fine to coarse" transfer, solve a smaller coarse problem, and do some "coarse to fine" transfers? And in this last case, what "some" should be: 2 more? This last idea, which is somehow related to the multigrid methodology ( in [30] grid transfer according to V or W or other scheme), is an interesting future work.

Still on the subject of parallel performance, one can also consider a hybrid multithreading/MPI implementation of the proposed two-scale distributed implementation to somehow select the right range of cores for the right scale. Specifically, in the algorithm F.5, as mentioned in section 5.2, when all distributed patches are calculated, the remaining local patches are computed independently (processes are not longer synchronized). For this, in a process, a sequential computation was naturally used but as in [18] a multithreaded computation can also be a solution. The main impact would be to provide a parameter to adjust the number of distributed patches and the memory consumption per process. In a multithreaded context, the constraint added by the dynamic scheduling proposed in [18] (the largest local patch limits the number of threads) will certainly play a role in choosing the MPI/thread partition. But this flexibility will certainly also allow to choose the right number of processes at the global scale depending on the solver used at this scale. As a side effect, many other tasks can also benefit from this hybrid implementation: many loops on the super-patch macro elements can be nicely paralyzed across many threads in the algorithm F.2, F.4, F.3, F.6 and F.7 due to the per-macro-element storage and computation of data. But for large global-scale problem, the question of which solver to choose for that scale will certainly remain open.

Finally, a last perspective on local scale performance concerns the use of a direct solver to solve patches (distributed or not). It is possible to consider that the enrichment functions vary slowly during the two-scale iteration. Thus, if conditioning is not an issue, using an iterative solver to solve the patches may be more efficient because using the previous solutions at almost all two-scale iteration would certainly reduce the number of solver iterations. And in this context, storing data by macro element could relatively naturally result in a versatile block Jacobi preconditioner (each block can be used for many patches). This can also have an impact on the memory footprint (it is no longer necessary to store the factorization of each patch).

## acknowledgements

The authors would like to thank Nicolas Chevaugnon and Gregory Legrain with whom the conversations about parallelism and the GFEM<sup>gl</sup> method were fruitful.

## References

- [1] P. Amestoy, C. Ashcraft, O. Boiteau, A. Buttari, J. L'Excellent, and C. Weisbecker. Improving multifrontal methods by means of block low-rank representations. *SIAM Journal on Scientific Computing*, 37(3):A1451–A1474, 2015.
- [2] P. Amestoy, I. Duff, J. L'Excellent, and J. Koster. A fully asynchronous multifrontal solver using distributed dynamic scheduling. *SIAM Journal on Matrix Analysis and Applications*, 23(1):15–41, 2001.
- [3] P. R. Amestoy, A. Guermouche, J.-Y. L'Excellent, and S. Pralet. Hybrid scheduling for the parallel solution of linear systems. *Parallel Computing*, 32(2):136 – 156, 2006. Parallel Matrix Algorithms and Applications (PMAA'04).
- [4] I. Babuška and U. Banerjee. Stable Generalized Finite Element Method (SGFEM). *Computer Methods in Applied Mechanics and Engineering*, 201-204:91–111, 2012.

- [5] S. Bordas, T. Rabczuk, and G. Zi. Three-dimensional crack initiation, propagation, branching and junction in non-linear materials by an extended meshfree method without asymptotic enrichment. *Engineering Fracture Mechanics*, 75(5):943–960, Mar. 2008.
- [6] C. A. Duarte and D. J. Kim. Analysis and applications of a generalized finite element method with global-local enrichment functions. *Computer Methods in Applied Mechanics and Engineering*, 197(6-8):487–504, 2008.
- [7] C. A. Duarte, D.-J. Kim, and I. Babuška. A global-local approach for the construction of enrichment functions for the generalized fem and its application to three-dimensional cracks. In V. M. A. Leitão, C. J. S. Alves, and C. Armando Duarte, editors, *Advances in Meshfree Techniques*, pages 1–26, Dordrecht, 2007. Springer Netherlands.
- [8] R. Eligehausen and G. Sawade. A fracture mechanics based description of the pull-out behavior of headed studs embedded in concrete. In *RILEM Report*, page 281–299. L. Elfgrén, Chapman and Hall, London, 1989.
- [9] T. Fries. A corrected XFEM approximation without problems in blending elements. *International Journal for Numerical Methods in Engineering*, 75(5):503–532, jul 2008.
- [10] T. C. Gasser and G. A. Holzapfel. Modeling 3D crack propagation in unreinforced concrete using PUFEM. *Computer Methods in Applied Mechanics and Engineering*, 194(25-26):2859–2896, 2005.
- [11] R. Geelen, J. Plews, M. Tupek, and J. Dolbow. An extended/generalized phase-field finite element method for crack growth with global-local enrichment. *International Journal for Numerical Methods in Engineering*, 121(11):2534–2557, jun 2020.
- [12] V. Gupta, C. Duarte, I. Babuška, and U. Banerjee. Stable GFEM (SGFEM): Improved conditioning and accuracy of GFEM/XFEM for three-dimensional fracture mechanics. *Computer Methods in Applied Mechanics and Engineering*, 289(FEBRUARY):355–386, 2015.
- [13] V. Gupta, C. A. Duarte, I. Babuška, and U. Banerjee. A stable and optimally convergent generalized FEM (SGFEM) for linear elastic fracture mechanics. *Computer Methods in Applied Mechanics and Engineering*, 266:23–39, 2013.
- [14] V. Gupta, D.-j. Kim, and C. A. Duarte. Analysis and improvements of global–local enrichments for the Generalized Finite Element Method. *Computer Methods in Applied Mechanics and Engineering*, 245-246:47–62, oct 2012.
- [15] N. J. Higham and T. Mary. Solving block low-rank linear systems by LU factorization is numerically stable. *IMA Journal of Numerical Analysis*, 42(2):951–980, apr 2022.
- [16] G. Karypis and V. Kumar. A coarse-grain parallel multilevel  $k$ -way partitioning algorithm. In *Proceedings of the 8th SIAM conference on Parallel Processing for Scientific Computing*, 1997.
- [17] D.-J. Kim, C. A. Duarte, and S. P. Proenca. A generalized finite element method with global-local enrichment functions for confined plasticity problems. *Computational Mechanics*, 50(5):563–578, nov 2012.
- [18] D. J. Kim, C. A. Duarte, and N. A. Sobh. Parallel simulations of three-dimensional cracks using the generalized finite element method. *Computational Mechanics*, 47(3):265–282, 2011.
- [19] D.-J. Kim, S.-G. Hong, and C. A. Duarte. Generalized finite element analysis using the preconditioned conjugate gradient method. *Applied Mathematical Modelling*, 39(19):5837–5848, oct 2015.
- [20] D.-J. Kim, J. P. a. Pereira, and C. a. Duarte. Analysis of three-dimensional fracture mechanics problems: A two-scale approach using coarse-generalized FEM meshes. *International Journal for numerical methods in engineering*, 81:335–365, 2010.
- [21] H. Li and C. A. Duarte. A two-scale generalized finite element method for parallel simulations of spot welds in large structures. *Computer Methods in Applied Mechanics and Engineering*, 337:28–65, 2018.
- [22] H. Li, P. O’Hara, and C. Duarte. Non-intrusive coupling of a 3-D Generalized Finite Element Method and Abaqus for the multiscale analysis of localized defects and structural features. *Finite Elements in Analysis and Design*, 193(April):103554, oct 2021.
- [23] A. K. Noor. Global-local methodologies and their application to nonlinear analysis. *Finite Elements in Analysis and Design*, 2(4):333–346, 1986.
- [24] P. O’Hara, C. A. Duarte, and T. Eason. Generalized finite element analysis of three-dimensional heat transfer problems exhibiting sharp thermal gradients. *Computer Methods in Applied Mechanics and Engineering*, 198(21-26):1857–1871, 2009.
- [25] J. Ožbolt, R. Eligehausen, and H. Reinhardt. Size effect on the concrete cone pull-out load. *International Journal of Fracture*, 95(1):391–404, 1999.



- [26] J. P. A. Pereira, D.-J. Kim, and C. A. Duarte. A two-scale approach for the analysis of propagating three-dimensional fractures. *Computational Mechanics*, 49(1):99–121, Aug. 2011.
- [27] J. Plews and C. Duarte. Bridging multiple structural scales with a generalized finite element method. *International Journal for Numerical Methods in Engineering*, 102(3-4):180–201, apr 2015.
- [28] J. Plews and C. Duarte. Generalized finite element approaches for analysis of localized thermo-structural effects. *International Journal for Numerical Methods in Engineering*, 104(6):408–438, nov 2015.
- [29] J. A. Plews and C. A. Duarte. A two-scale generalized finite element approach for modeling localized thermo-plasticity. *International Journal for Numerical Methods in Engineering*, 108(10):1123–1158, dec 2016.
- [30] Y. Saad. *Iterative Methods for Sparse Linear Systems*. Society for Industrial and Applied Mathematics, second edition, 2003.
- [31] A. Salzman. *Thick Level Set model implementation in 3D parallel context*. PhD thesis, Ecole Centrale de Nantes, 1, rue de la noë, 44321, Nantes, France, Oct. 2019.

## A notation convention

The following conventions are used in the algorithms in this document:

- $\Leftarrow$  implies assembling a vector or matrix of a space(s) or set(s) embedded in the receiving space(s) or set(s)
- $(A, B) \Leftarrow (C, D)$  is equivalent to  $A \Leftarrow C$  and  $B \Leftarrow D$
- $(A, B) \Leftarrow (C, D)$  is equivalent to  $A \Leftarrow C$  and  $B \Leftarrow D$
- $A \Leftarrow (C, D)$  is equivalent to  $A \Leftarrow C$  and  $A \Leftarrow D$
- $A \Leftarrow \{B, C\}$  indicate that the matrices  $B$  and  $C$  are merged by column to form a single matrix stored in  $A$
- $(A, B, C) \Leftarrow \text{PROCEDURE} \dots$  indicates that the called PROCEDURE returns data which are stored in  $A, B$  and  $C$ . See return declaration in PROCEDURE.
- $\triangleright$  represents a task involving communication (point to point or collective)
- If  $\mathcal{C}$  is a set of entities:
  - $\mathcal{C} \setminus e$  is removing  $e$  from  $\mathcal{C}$
  - $\mathcal{C} \cup e$  is adding  $e$  to the end of  $\mathcal{C}$
- $weight_k$  is the weight of a patch identified by the letter  $k$ : number of micro-scale elements embedded in the patch  $k$
- To simplify the algorithms,  $A^{-1}$  expresses the inverse of the matrix  $A$ , but it is in many cases the factorization that is actually obtained and used. Thus  $X = A^{-1} \cdot B$  is calculate as the solution of  $L \cdot D \cdot L^T \cdot X = B$  where  $L$  and  $D$  are the lower triangular and diagonal matrices obtained by factoring  $A$ .
- The subscripted letters, corresponding to the sets of values defined in the table 1, give the dofs on which the matrix or the vector is defined. Thus,  $\mathbf{A}_{gg}$  is a matrix of dimension  $card(g) \times card(g)$  and  $\mathbf{U}_g$  is a vector of size  $card(g)$ .
- The superscript *patches* indicates the set of matrices or vectors of all fine-scale problems:  $X^{patches} = \{X^p : p \in patches\}$  with  $patches = \{1, 2, \dots, card(I_e^g)\}$  (see section 2 for definition of  $I_e^g$ )

## B values set

A large number of sets are put in place to clarify the presentation of the different discretizations. The value of the discretized field at a node is called the value. This value can be fixed or free. When it is free, it can be classical or enriched. There are three reasons why a value may be fixed: on the physical Dirichlet boundary conditions, on the patch boundary when solving fine scale problems or when setting the hanging node value of a micro node. Regarding the set notations, lower case will be used for free values while upper case will be used for fixed values or for a set of values gathering both fixed and free values. All value types are described in table 1.

Set	Values type	Relation	Scale
$G$	global-scale values	$G = D \cup g, D \cap g = \emptyset$	coarse-level
$D$	fixed values (Dirichlet)	$D \subset G$	
$C$	classical values	$C = D \cup c$	
$g$	free values	$g = c \cup e$	
$c$	classical free values	$c = C \setminus D, c = h \cup k$	
$e$	enriched free values	$e = G \setminus C$	
$m$	free values related to SP elements	$m = k \cup e$	
$k$	classical free values related to SP elements	$k \in c, k \cap h = \emptyset$	
$h$	classical free values not related to SP elements	$h = c \setminus k$	
$Q$	fine-scale values	$Q = L \cup DG \cup d \cup q$	patch-level ( $p^{th}$ )
$L$	fixed values (by linear relation)	$L \subset Q, L \cap DP = \emptyset, L \cap d = \emptyset$	
$DP$	fixed values ( $D$ restricted to patch $p$ )	$DP = D \cap Q$	
$d$	fixed values (Dirichlet from fine solution $f$ )	$d = f \cap Q$	
$q$	free values	$q = Q \setminus (d \cup DG \cup L)$	
$R$	reference values	$R = M \cup L, M \cap L = \emptyset$	mix fine/coarse level
$L$	fixed values (by linear relation)	$L \subset R, L \cap DR = \emptyset$	
$M$	reference values without L	$M = r \cup DR = F \cup H, r \cap DR = \emptyset$	
$DR$	fixed values (inherited from D)	$DR \subset M, D \subset DR$	
$F$	reference values related to SP elements	$F = f \cup (DR \setminus (DR \cap H))$	
$H$	reference values not related to SP elements	$H = h \cup (DR \setminus (DR \cap F))$	
$r$	reference free values	$r = h \cup f$	
$f$	free values related to SP elements	$f \subset r$	
$h$	free values not related to SP elements	$h = r \setminus f, h$ same as $h$ at coarse-level	

Table 1: Value sets description ( lowercase letter for free values, upper case letter for free and fixed values)

## C Mesh adaptation

In this work, the mesh adaptation uses a simple splitting strategy. For each level of refinement, we take the impacted elements (i.e. those that meet a certain criterion provided by a user-defined function) from the previous level and divide each of them in an encapsulated manner. New nodes are added to the middle of the edges of impacted elements. The affected elements are then replaced by a tetrahedronization based on the old and new nodes, so that the new elements are encapsulated in the destroyed old elements. The figure 1 illustrates this process, in 2D for simplicity. In the figure

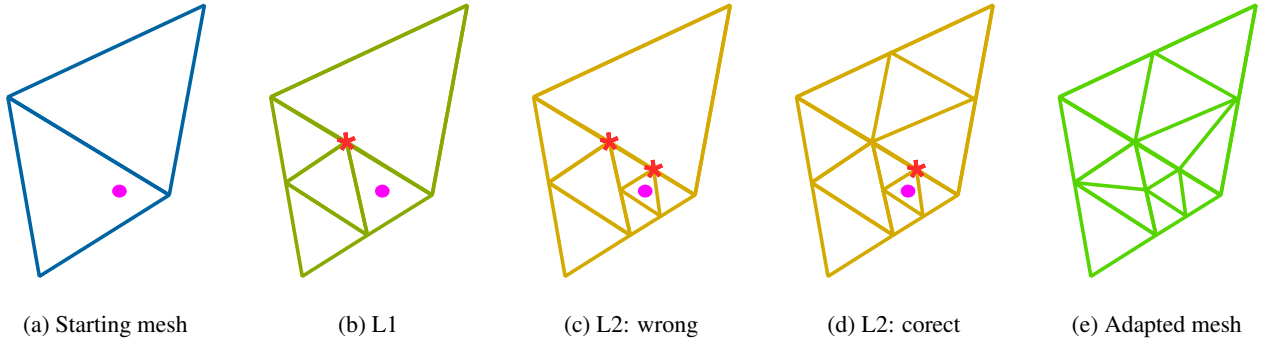


Figure 1: mesh refinement principles (presented in 2D but the same principle applies in 3D): the dot represents the area of interest and the stars the hanging nodes. Only one hanging node is accepted per edge

1a 2 triangles represent the starting level of the adaptation with a dot representing the area of interest. The first level of refinement, L1 (figure 1b), divides only the triangle covering the area of interest. A hanging node (start in figure 1b) appears in the middle of the edge common to the triangles in the figure 1a. Then, when moving to the next level of refinement, L2, again only the element covering the area of interest is split. If we simply split this element (figure 1c) 2 hanging nodes appear on the same edge. This is considered too abrupt in terms of mesh transition and is therefore avoided by forcing the splitting of the second initial unmodified triangle (figure 1d). This "one hanging node per edge" rule imposes a smoother mesh transition. When the adaptation is complete (i.e. for example when the target size of the element is reached in the area of interest), the hanging nodes are removed by splitting the element with the hanging



edge/face using only that node and the existing vertices (figure 1e). Note that in 3D, an additional node can be added to the center of gravity of the tetrahedron which is modified by removing the hanging node.

The algorithm associated with this process is implemented in parallel. In short, for one level of refinement, it reviews all impacted elements. Next, it examines whether splitting these elements would violate the "one hanging node per edge" rule. If this is the case, the connected elements (i.e. those with a hanging edge/face) are added to the list of elements to divide. This verification operation is repeated until no more elements are added. There may be some communication during this task. Then all selected element are split. The next level of refinement may occur or, if it is complete (i.e. there are no more elements selected for splitting), the final deletion of hanging nodes is performed. More details can be found in [31].

Note that a constrained Delaunay tetrahedralization can be an interesting alternative for this work as long as the coarse mesh remains a skeleton of the new discretization: all faces/edges of the tetrahedra of the coarse mesh remain defined (possibly divided several times) in the new mesh.

## D $\mathbf{T}_{MG}$ construction

The  $\mathbf{T}_{MG}$  matrix is a linear interpolation operator with the following structure, considering that the M-set is ordered with the H-set first and the F-set second, and that the G-set is ordered with the D-set first, the c-set second and the e-set third with h-set first in the c-set:

$$\mathbf{T}_{MG} = \begin{pmatrix} \mathbf{T}_{HD} & \mathbf{T}_{Hh} & \mathbf{0} & \mathbf{0} \\ \mathbf{T}_{FD} & \mathbf{0} & \mathbf{T}_{Fk} & \mathbf{T}_{Fe} \end{pmatrix} \quad (42)$$

A term of  $\mathbf{T}_{MG}$  at index  $(a, b)$  is, according to the equation (21), either  $N^i(\mathbf{x}^j)$  or  $N^i(\mathbf{x}^j)\mathbf{F}^p(\mathbf{x}^j) \cdot \mathbf{e}_k$  where  $\mathbf{x}^j$  is the node associated to the dof  $a$ ,  $\mathbf{e}_k$  is the unite-vector associated to the component that dof  $a$  represent on the node  $\mathbf{x}^j$ , and  $\mathbf{x}^i$  is the node associated to dof  $b$ . When  $a \in H$  and  $b \in m$ , as the node  $\mathbf{x}^j$  is not in the support of the node  $\mathbf{x}^i$  all  $N^i(\mathbf{x}^j)$  terms are zero and the H-set $\times$ m-set block is null. And it is the same when  $a \in F$  and  $b \in h$ , the block F-set $\times$ h-set is null. When  $b \in D$  only the nodes  $\mathbf{x}^j$  on the derived Dirichlet boundary conditions give nonzero terms, i.e. when  $a \in DR$ . All other terms are zero in  $\mathbf{T}_{HD}$  and  $\mathbf{T}_{FD}$ . For  $a \in H$  and  $b \in h$  the macro and micro meshes are the same and the only non-zero terms are when  $a = b$ . The h-set $\times$ h-set block is then an identity matrix and all the other terms of  $\mathbf{T}_{Hh}$  are null. The remaining blocks  $\mathbf{T}_{Fk}$  and  $\mathbf{T}_{Fe}$  correspond respectively to  $N^i(\mathbf{x}^j)$  for a classical dof ( $b \in k$ ) and to  $N^i(\mathbf{x}^j)\mathbf{F}^p(\mathbf{x}^j) \cdot \mathbf{e}_k$  for an enriched dof ( $b \in e$ ).

## E Global scale problem construction

The equality (23) gives the following system:

$$\mathbf{T}_{MG}' \cdot \mathbf{A}_{MM} \cdot \mathbf{T}_{MG} \cdot \mathbf{U}_g = \mathbf{T}_{MG}' \cdot \mathbf{B}_M \quad (43)$$

It can be rewritten as follows using (42) and the divided matrices on the sets H and F :

$$\begin{pmatrix} \mathbf{T}_{HD}' & \mathbf{T}_{FD}' \\ \mathbf{T}_{Hh}' & \mathbf{0} \\ \mathbf{0} & \mathbf{T}_{Fk}' \\ \mathbf{0} & \mathbf{T}_{Fe}' \end{pmatrix} \cdot \begin{pmatrix} \mathbf{A}_{HH} & \mathbf{A}_{HF} \\ \mathbf{A}_{FH} & \mathbf{A}_{FF} \end{pmatrix} \cdot \begin{pmatrix} \mathbf{T}_{HD} & \mathbf{T}_{Hh} & \mathbf{0} & \mathbf{0} \\ \mathbf{T}_{FD} & \mathbf{0} & \mathbf{T}_{Fk} & \mathbf{T}_{Fe} \end{pmatrix} \cdot \begin{pmatrix} \mathbf{u}_D \\ \mathbf{u}_h \\ \mathbf{u}_k \\ \mathbf{u}_e \end{pmatrix} = \begin{pmatrix} \mathbf{T}_{HD}' & \mathbf{T}_{FD}' \\ \mathbf{T}_{Hh}' & \mathbf{0} \\ \mathbf{0} & \mathbf{T}_{Fk}' \\ \mathbf{0} & \mathbf{T}_{Fe}' \end{pmatrix} \cdot \begin{pmatrix} \mathbf{B}_H \\ \mathbf{B}_F \end{pmatrix} \quad (44)$$

This gives the system:

$$\begin{pmatrix} \mathbf{A}_{DD} & \mathbf{A}_{Dg} \\ \mathbf{A}_{gD} & \mathbf{A}_{gg} \end{pmatrix} \cdot \begin{pmatrix} \mathbf{U}_D \\ \mathbf{U}_g \end{pmatrix} = \begin{pmatrix} \mathbf{B}_D \\ \mathbf{BN}_g \end{pmatrix} \quad (45)$$

where, considering here a symmetric system (but there is no restriction for a non-symmetric system) :

$$\mathbf{A}_{gg} = \begin{pmatrix} \mathbf{T}_{Hh}' \cdot \mathbf{A}_{HH} \cdot \mathbf{T}_{Hh} & \mathbf{T}_{Hh}' \cdot \mathbf{A}_{HF} \cdot \mathbf{T}_{Fk} & \mathbf{T}_{Hh}' \cdot \mathbf{A}_{HF} \cdot \mathbf{T}_{Fe} \\ \mathbf{T}_{Fk}' \cdot \mathbf{A}_{HF} \cdot \mathbf{T}_{Hh} & \mathbf{T}_{Fk}' \cdot \mathbf{P}_{Fk} & \mathbf{P}_{Fk}' \cdot \mathbf{T}_{Fe} \\ \mathbf{T}_{Fe}' \cdot \mathbf{A}_{HF} \cdot \mathbf{T}_{Hh} & \mathbf{T}_{Fe}' \cdot \mathbf{P}_{Fk} & \mathbf{T}_{Fe}' \cdot \mathbf{A}_{FF} \cdot \mathbf{T}_{Fe} \end{pmatrix} \text{ with } \mathbf{P}_{Fk} = \mathbf{A}_{FF} \cdot \mathbf{T}_{Fk} \quad (46)$$

$$\mathbf{BN}_g = \begin{pmatrix} \mathbf{T}_{Hh}' \cdot \mathbf{B}_H \\ \mathbf{T}_{Fk}' \cdot \mathbf{B}_F \\ \mathbf{T}_{Fe}' \cdot \mathbf{B}_F \end{pmatrix} \quad (47)$$

$$\mathbf{A}_{gD} = \begin{pmatrix} \mathbf{T}_{Hh}^t \cdot (\mathbf{A}_{HH} \cdot \mathbf{T}_{HD} + \mathbf{A}_{HF} \cdot \mathbf{T}_{FD}) \\ \mathbf{T}_{Fk}^t \cdot \mathbf{A}_{HF}^t \cdot \mathbf{T}_{HD} + \mathbf{P}_{Fk}^t \cdot \mathbf{T}_{FD} \\ \mathbf{T}_{Fe}^t \cdot (\mathbf{A}_{HF}^t \cdot \mathbf{T}_{HD} + \mathbf{A}_{FF} \cdot \mathbf{T}_{FD}) \end{pmatrix} \quad (48)$$

and  $\mathbf{A}_{DD}$ ,  $\mathbf{A}_{Dg}$  and  $\mathbf{B}_D$  not being shown here because not used later. The  $\mathbf{A}_{HF}$  term represents the coupling term of the NSP part with the SP boundary (nodes surrounding SP, around yellow part in the figure 1c, named SPF in this work). For this boundary, we know that the nodes are not enriched, so the sub-bloc corresponding to these dofs in  $\mathbf{T}_{Fe}$  is zero and  $\mathbf{A}_{HF} \cdot \mathbf{T}_{Fe} = 0$ . Moreover, for this boundary, all the fine-scale elements are identical to the global-scale elements, therefore the sub-bloc corresponding to these dofs in  $\mathbf{T}_{Fk}$  is an identity matrix  $\mathbf{I}_{Fk}$  and  $\mathbf{A}_{HF} \cdot \mathbf{T}_{Fk} = \mathbf{A}_{HF} \cdot \mathbf{I}_{Fk}$ . Otherwise, the  $\mathbf{T}_{Hh}$  operator, because of its structure (given in 42) reduces a block with H-set rows or columns to a block with h-set rows or columns. Thus  $\mathbf{A}_{gg}$  can be written as :

$$\mathbf{A}_{gg} = \begin{pmatrix} \mathbf{A}_{hh} & \mathbf{A}_{hF} \cdot \mathbf{I}_{Fk} & \mathbf{0} \\ \mathbf{I}_{Fk}^t \cdot \mathbf{A}_{hF}^t & \mathbf{T}_{Fk}^t \cdot \mathbf{P}_{Fk} & \mathbf{P}_{Fk}^t \cdot \mathbf{T}_{Fe} \\ \mathbf{0} & \mathbf{T}_{Fe}^t \cdot \mathbf{P}_{Fk} & \mathbf{T}_{Fe}^t \cdot \mathbf{A}_{FF} \cdot \mathbf{T}_{Fe} \end{pmatrix} \quad (49)$$

And the  $\mathbf{BN}_g$  and  $\mathbf{A}_{gD}$  matrices simplify as follows:

$$\mathbf{BN}_g = \begin{pmatrix} \mathbf{B}_h \\ \mathbf{T}_{Fk}^t \cdot \mathbf{B}_F \\ \mathbf{T}_{Fe}^t \cdot \mathbf{B}_F \end{pmatrix} \quad (50)$$

$$\mathbf{A}_{gD} = \begin{pmatrix} \mathbf{A}_{hH} \cdot \mathbf{T}_{HD} + \mathbf{A}_{hF} \cdot \mathbf{T}_{FD} \\ \mathbf{I}_{Fk}^t \cdot \mathbf{A}_{HF}^t \cdot \mathbf{T}_{HD} + \mathbf{P}_{Fk}^t \cdot \mathbf{T}_{FD} \\ \mathbf{T}_{Fe}^t \cdot \mathbf{A}_{FF} \cdot \mathbf{T}_{FD} \end{pmatrix} \quad (51)$$

By eliminating the Dirichlet boundary condition of the system (45), the final system to solve is (24) with

$$\mathbf{B}_g = \mathbf{BN}_g - \mathbf{A}_{gD} \cdot \mathbf{U}_D \quad (52)$$

and with full terms:

$$\mathbf{B}_g = \begin{pmatrix} \mathbf{B}_h - \mathbf{A}_{hH} \cdot \mathbf{T}_{HD} \cdot \mathbf{U}_D - \mathbf{A}_{hF} \cdot \mathbf{T}_{FD} \cdot \mathbf{U}_D \\ \mathbf{T}_{Fk}^t \cdot \mathbf{B}_F - \mathbf{I}_{Fk}^t \cdot \mathbf{A}_{HF}^t \cdot \mathbf{T}_{HD} \cdot \mathbf{U}_D - \mathbf{P}_{Fk}^t \cdot \mathbf{T}_{FD} \cdot \mathbf{U}_D \\ \mathbf{T}_{Fe}^t \cdot (\mathbf{B}_F - \mathbf{A}_{FF} \cdot \mathbf{T}_{FD} \cdot \mathbf{U}_D) \end{pmatrix} \quad (53)$$

In this work, the Dirichlet boundary conditions are zero imposed displacements in all tested cases. Thus, to simplify the presentation,  $\mathbf{U}_D$  is fixed at  $\mathbf{0}$  and 53 becomes:

$$\mathbf{B}_g = \begin{pmatrix} \mathbf{B}_h \\ \mathbf{T}_{Fk}^t \cdot \mathbf{B}_F \\ \mathbf{T}_{Fe}^t \cdot \mathbf{B}_F \end{pmatrix} \quad (54)$$

## F Two-scale procedures

### F.1 INIT

The INIT procedure is given by algorithm F.2. In this procedure, the constant sub-blocks of 49 and 54 are stored in memory as  $\mathbf{A}_{gg}^{ini}$  and  $\mathbf{B}_g^{ini}$  which will be reused in the two-scale loop to compute the final matrices  $\mathbf{A}_{gg}$  and  $\mathbf{B}_g$ . In INIT, the first loop on SP macro-elements computes and attaches to a macro-element  $e_{macro}$  the matrices  $\mathbf{A}_{FF}^{e_{macro}}$  and  $\mathbf{B}_F^{e_{macro}}$ , computed by integration and assembly of (10) over  $\omega^{e_{macro}}$  with elimination of (12) but keeping Dirichlet values. In this loop, the vectors  $\mathbf{u}_F^{e_{macro}}$ , dedicated to the storage of the  $e_{macro}$  part of the  $\mathbf{u}_F$  vector, are also allocated and attached to  $e_{macro}$ . Still in this loop,  $\mathbf{T}_{Fk}^{e_{macro}}$  and  $\mathbf{P}_{Fk}^{e_{macro}}$  are computed and attached to the macro-elements because they will also be reused in the two-scale loop (in fact it is  $\mathbf{T}_{Fm}^{e_{macro}}$  operator with a  $\mathbf{T}_{Fe}^{e_{macro}}$  null at this stage that is saved in memory). Finally, the  $\mathbf{T}_{Fk}^{e_{macro}} \cdot \mathbf{P}_{Fk}^{e_{macro}}$  and  $\mathbf{T}_{Fk}^{e_{macro}} \cdot \mathbf{B}_F^{e_{macro}}$  terms are calculated and assembled into  $\mathbf{A}_{gg}^{ini}$  and  $\mathbf{B}_g^{ini}$ . The second loop on the NSP elements (if any) computes the terms  $\mathbf{A}_{hh}$ ,  $\mathbf{A}_{hF}$  and  $\mathbf{B}_h$  and assembles them into  $\mathbf{A}_{gg}^{ini}$  and  $\mathbf{B}_g^{imp}$ . This last temporary vector contains the boundary condition for the NSP elements and is used as an argument to the COMPUTE\_B\_NORM procedure (algorithm F.7 below) called by INIT to obtain  $\|\mathbf{B}_r\|$ , the constant denominator of  $resi$ . Once this is done,  $\mathbf{B}_g^{imp}$  is added to  $\mathbf{B}_g^{ini}$  to save it. The INIT procedure, with a loop over the patches, is also responsible for defining and partially creating the fine-scale linear systems (25). Construction of one of these systems for  $p \in I_e^g$ , is simply obtained by assembling  $\mathbf{A}_{FF}^{e_{macro}}$  and  $\mathbf{B}_F^{e_{macro}}$  with  $e_{macro} \in J^p$  to form the following system:

$$\begin{pmatrix} \mathbf{A}_{DRDR}^p & \mathbf{A}_{DRd}^p & \mathbf{A}_{DRq}^p \\ \mathbf{A}_{dDR}^p & \mathbf{A}_{dd}^p & \mathbf{A}_{dq}^p \\ \mathbf{A}_{qDR}^p & \mathbf{A}_{qd}^p & \mathbf{A}_{qq}^p \end{pmatrix} \cdot \begin{pmatrix} \mathbf{u}_{DR}^p \\ \mathbf{u}_d^p \\ \mathbf{u}_q^p \end{pmatrix} = \begin{pmatrix} \mathbf{BN}_{DR}^p \\ \mathbf{BN}_d^p \\ \mathbf{BN}_q^p \end{pmatrix} \quad (55)$$

---

**Algorithm F.2** Two-scale algorithm: initialization part. Procedure COMPUTE\_B\_NORM is given by algorithm F.7

---

```

procedure INIT
  create empty  $\mathbf{A}_{gg}^{ini}$  and  $\mathbf{B}_g^{ini}$ 
  for  $e_{macro} \in SP$  do
    Initialize  $\mathbf{u}_R^{e_{macro}}$  fine-scale dofs covered by  $e_{macro}$ 
    Eliminate linear relation if any from  $\mathbf{u}_R^{e_{macro}}$  to create  $\mathbf{u}_F^{e_{macro}}$ 
    create empty  $\mathbf{A}_{FF}^{e_{macro}}$  matrix and  $\mathbf{B}_F^{e_{macro}}$  vector
    for  $e_{micro} \in e_{macro}$  do
      compute  $\mathbf{A}_{FF}^{e_{micro}}$  matrix and  $\mathbf{B}_F^{e_{micro}}$  vector
       $(\mathbf{A}_{FF}^{e_{macro}}, \mathbf{B}_F^{e_{macro}}) \leftarrow (\mathbf{A}_{FF}^{e_{micro}}, \mathbf{B}_F^{e_{micro}})$ 
    end for
    Create  $\mathbf{T}_{Fk}^{e_{macro}}$  operator based on classical form function of  $e_{macro}$  at  $\mathbf{u}_F^{e_{macro}}$  dof location
     $\mathbf{P}_{Fk}^{e_{macro}} \leftarrow \mathbf{A}_{FF}^{e_{macro}} \cdot \mathbf{T}_{Fk}^{e_{macro}}$ 
     $\mathbf{A}_{kk}^{e_{macro}} \leftarrow \mathbf{T}_{Fk}^{e_{macro}} \cdot \mathbf{P}_{Fk}^{e_{macro}}$ 
     $\mathbf{B}_k^{e_{macro}} \leftarrow \mathbf{T}_{Fk}^{e_{macro}} \cdot \mathbf{B}_F^{e_{macro}}$ 
     $(\mathbf{A}_{gg}^{ini}, \mathbf{B}_g^{ini}) \leftarrow (\mathbf{A}_{kk}^{e_{macro}}, \mathbf{B}_k^{e_{macro}})$ 
    Create a zero value  $\mathbf{T}_{Fe}^{e_{macro}}$  operator, component product of shifted enrichment function with classical form function of
     $e_{macro}$  at  $\mathbf{u}_F^{e_{macro}}$  dof location
     $\mathbf{T}_{Fm}^{e_{macro}} \leftarrow \{\mathbf{T}_{Fk}^{e_{macro}}, \mathbf{T}_{Fe}^{e_{macro}}\}$ 
  end for
  for  $e_{macro} \in NSP$  do
    compute  $\mathbf{A}_{hh}^{e_{macro}}, \mathbf{A}_{hF}^{e_{macro}}$  matrix and  $\mathbf{B}_h^{e_{macro}}$  vector
     $(\mathbf{A}_{gg}^{ini}, \mathbf{B}_g^{ini}) \leftarrow ((\mathbf{A}_{hh}^{e_{macro}}, \mathbf{A}_{hF}^{e_{macro}} \cdot \mathbf{I}_{Fk}^{e_{macro}}), \mathbf{B}_h^{e_{macro}})$ 
  end for
   $\|\mathbf{B}_r\| \leftarrow \text{COMPUTE\_B\_NORM}(\mathbf{B}_g^{tmp}, \mathbf{B}_F)$ 
   $\mathbf{B}_g^{ini} \leftarrow \mathbf{B}_g^{ini} + \mathbf{B}_g^{tmp}$ 
  for  $p \in patches$  do
    Create  $\mathbf{u}_Q^p$  fine-scale dofs covered by patch  $p$ 
    Eliminate fixed values from  $\mathbf{u}_Q^p$  to create  $\mathbf{u}_q^p$ 
    Create empty  $\mathbf{A}_{qq}^p$  matrix and  $\mathbf{B}_q^p$  vector
    for  $e_{macro} \in p$  do
       $(\mathbf{A}_{qq}^p \text{ and } \mathbf{A}_{qd}^p, \mathbf{B}_q^p) \leftarrow (\mathbf{A}_{FF}^{e_{macro}}, \mathbf{B}_F^{e_{macro}})$ 
    end for
     $\mathbf{D}_{qd}^p \leftarrow -\mathbf{A}_{qd}^p$ 
  end for
  return  $\mathbf{A}_{gg}^{ini}, \mathbf{B}_g^{ini}, \mathbf{A}_{FF}, \mathbf{B}_F, \|\mathbf{B}_r\|, \mathbf{A}_{qq}^{patches}, \mathbf{B}_q^{patches}, \mathbf{D}_{qd}^{patches}$ 
end procedure

```

---

Eliminating from (55) the Dirichlet boundary condition on  $\partial\omega_p$  we obtain:

$$\mathbf{A}_{qq}^p \cdot \mathbf{u}_q^p = \mathbf{B}_q^p - \mathbf{A}_{qDR}^p \cdot \mathbf{u}_{DR}^p - \mathbf{A}_{qd}^p \cdot \mathbf{u}_d^p \quad (56)$$

Right-hand side of (56) (which corresponds to the vector  $\mathbf{B}_q^p$ ) is divided in two contributions:  $\mathbf{B}_q^p = \mathbf{B}_q^p - \mathbf{A}_{qDR}^p \cdot \mathbf{u}_{DR}^p$  which is constant during the two-scale loop and  $\mathbf{D}_{qd}^p \cdot \mathbf{u}_d^p$  (with  $\mathbf{D}_{qd}^p = -\mathbf{A}_{qd}^p$ ) which varies during the two-scale loop as does  $\mathbf{u}_d^p$  (subset of  $\mathbf{u}_F$ ). Thus, the INIT procedure creates for all patches  $\mathbf{A}_{qq}^p, \mathbf{B}_q^p$  and  $\mathbf{D}_{qd}^p$ .

## F.2 UPDATE\_MICRO\_DOFS

The UPDATE\_MICRO\_DOFS procedure (algorithm F.4) updates the values of  $\mathbf{u}_F$  from a  $\mathbf{U}_G$  vector given as argument according to the equation (22). This is done by a simple loop over the SP elements where for  $e_{macro} \in SP$  the following is computed:  $\mathbf{u}_F^{e_{macro}} = \mathbf{T}_{Fm}^{e_{macro}} \cdot \mathbf{U}_m^{e_{macro}}$  where  $\mathbf{U}_m^{e_{macro}}$  is the restriction of  $\mathbf{U}_G$  to  $e_{macro}$  dofs. The  $\mathbf{T}_{Fm}^{e_{macro}}$  is supposed to be correctly computed when we enter this procedure (i.e. its  $\mathbf{T}_{Fe}^{e_{macro}}$  part either null or updated by the UPDATE\_MACRO\_PRB procedure).

### F.3 MICRO-SCALE\_RESOLUTION

The MICRO-SCALE\_RESOLUTION procedure (algorithm F.5) loops over the patches to compute, for each patch  $p$ , the term  $\mathbf{D}_{qd}^p \cdot \mathbf{u}_d^p$  (given in (56)) with  $\mathbf{u}_d^p$  being the current  $\mathbf{u}_F$  restricted to  $\partial\omega_p \setminus \partial\Omega^D$ . This term added to  $\mathbf{BI}_q^p$  gives the right-hand side  $\mathbf{B}_q^p$  of the system (25). Then, as mentioned earlier, this system of equations is solved with a direct solver ( $\ddagger$  in algorithm F.5) that first processes a factorization of  $\mathbf{A}_{qq}^p$  before doing a backward/forward resolution. When the factorization is finished, as  $\mathbf{A}_{qq}^p$  is constant during the two-scale loop, only the factors are kept in memory,  $\mathbf{A}_{qq}^p$  being freed thus gaining memory. The following resolutions use the factors directly to solve the systems, which saves factoring time. This procedure, when completed, provides all  $\mathbf{u}_q^p$  solutions.

### F.4 UPDATE\_MACRO\_PRB

The UPDATE\_MACRO\_PRB procedure (algorithm F.3) is dedicated to the update of the problem at the global-scale (local to global transfer). It starts by copying  $\mathbf{A}_{gg}^{ini}$  and  $\mathbf{B}_g^{ini}$  into  $\mathbf{A}_{gg}$  and  $\mathbf{B}_g$  respectively. Then, a loop on the SP elements finishes the computation of  $\mathbf{A}_{gg}$  and  $\mathbf{B}_g$  as follows. The  $\mathbf{T}_{Fe}^{e_{macro}}$ , based on all  $\mathbf{u}_q^p$  covering  $e_{macro}$ , is constructed by following the enrichment function defined in (28) and the kinematic equation (29). This operator is used to update the  $\mathbf{T}_{Fm}^{e_{macro}}$  operator (for the algorithm F.4) and compute the terms  $\mathbf{T}_{Fe}^{e_{macro}} \cdot \mathbf{B}_F^{e_{macro}}$ ,  $\mathbf{T}_{Fe}^{e_{macro}} \cdot \mathbf{P}_{Fk}^{e_{macro}}$  and  $\mathbf{T}_{Fe}^{e_{macro}} \cdot \mathbf{A}_{FF}^{e_{macro}} \cdot \mathbf{T}_{Fe}^{e_{macro}}$  which are assembled into  $\mathbf{A}_{gg}$  and  $\mathbf{B}_g$ .

**Algorithm F.3** Two-scale algorithm : update macro problem. Here  $\mathbf{1}_F^{e_{macro}}$  is a unit vector corresponding to the F-set dofs (restricted to the dofs covered by  $e_{macro}$ ). The  $e^P$  corresponds to the index of the enriched dof for the patch  $p$  and  $k^P$  to the index of the classical dof related to  $e^P$

---

```

procedure UPDATE_MACRO_PRB( $\mathbf{A}_{gg}^{ini}$ ,  $\mathbf{B}_g^{ini}$ ,
 $\mathbf{u}_q^{patches}$ )
  ( $\mathbf{A}_{gg}, \mathbf{B}_g$ )  $\leftarrow$  ( $\mathbf{A}_{gg}^{ini}, \mathbf{B}_g^{ini}$ )
  for  $e_{macro} \in SP$  do
    for  $p \in patches$  including  $e_{macro}$  do
       $\mathbf{X}_F^{p,e_{macro}} \leftarrow$  restriction of  $\mathbf{u}_q^p$  to dofs covered by
       $e_{macro}$ 
       $shift^p \leftarrow \mathbf{X}_F^{p,e_{macro}} [e^p]$ 
       $\mathbf{T}_{Fe}^{e_{macro}} \leftarrow \mathbf{T}_{Fk^p}^{e_{macro}} * (\mathbf{X}_F^{p,e_{macro}} - \mathbf{1}_F^{e_{macro}} \times shift^p)$ 
    end for
     $\mathbf{T}_{Fm}^{e_{macro}} \leftarrow \{\mathbf{T}_{Fk}^{e_{macro}}, \mathbf{T}_{Fe}^{e_{macro}}\}$ 
     $\mathbf{A}_{ee}^{e_{macro}} \leftarrow \mathbf{T}_{Fe}^{e_{macro}} \cdot \mathbf{A}_{FF}^{e_{macro}} \cdot \mathbf{T}_{Fe}^{e_{macro}}$ 
     $\mathbf{A}_{ek}^{e_{macro}} \leftarrow \mathbf{T}_{Fe}^{e_{macro}} \cdot \mathbf{P}_{Fk}^{e_{macro}}$ 
     $\mathbf{A}_{gg} \leftarrow (\mathbf{A}_{ee}^{e_{macro}}, \mathbf{A}_{ek}^{e_{macro}})$ 
     $\mathbf{B}_g \leftarrow \mathbf{T}_{Fe}^{e_{macro}} \cdot \mathbf{B}_F^{e_{macro}}$ 
  end for
  return  $\mathbf{A}_{gg}, \mathbf{B}_g$ 
end procedure

```

---

**Algorithm F.4** Two-scale algorithm: update micro-scale field.

---

```

procedure UPDATE_MICRO_DOFS( $\mathbf{u}_g$ )
  for  $e_{macro} \in SP$  do
     $\mathbf{U}_m^{e_{macro}} \leftarrow$  restriction of  $\mathbf{u}_g$  to  $e_{macro}$  dofs
     $\mathbf{u}_F^{e_{macro}} \leftarrow \mathbf{T}_{Fm}^{e_{macro}} \cdot \mathbf{U}_m^{e_{macro}}$ 
  end for
  return  $\mathbf{u}_F$ 
end procedure

```

---

**Algorithm F.5** Two-scale algorithm: fine-scale problem computation.

---

```

procedure MICRO-SCALE_RESOLUTION( $\mathbf{u}_F$ ,  $\mathbf{A}_{qq}^{patches}$ ,
 $\mathbf{BI}_q^{patches}$ ,  $\mathbf{D}_{qd}^{patches}$ )
  for  $p \in patches$  do
    for  $e_{macro} \in p$  do
       $\mathbf{u}_d^p \leftarrow \mathbf{u}_F^{e_{macro}}$ 
    end for
     $\mathbf{B}_q^p \leftarrow \mathbf{BI}_q^p + \mathbf{D}_{qd}^p \cdot \mathbf{u}_d^p$ 
     $\mathbf{u}_q^p \leftarrow \mathbf{A}_{qq}^{-1,p} \cdot \mathbf{B}_q^p \ddagger$ 
  end for
  return  $\mathbf{u}_q^{patches}$ 
end procedure

```

---

### F.5 COMPUTE\_RESIDUAL

The COMPUTE\_RESIDUAL procedure (algorithm F.6) computes only the term  $\|\mathbf{A}_{fr} \cdot \mathbf{u}_r - \mathbf{B}_f\|$  of (27) considering that it is mainly a scalar product of the vector  $\mathbf{A}_{fr} \cdot \mathbf{u}_r - \mathbf{B}_f$  by itself. In this procedure, since the information is stored on the F-set, the computations are performed on this set. But since the organization of the data is by macro-element, the residual vector is not assembled into a complete F-set vector. During the first loop on SP, its contribution per macro-element ( $\mathbf{A}_{FF}^{e_{macro}} \cdot \mathbf{u}_F^{e_{macro}} - \mathbf{B}_F^{e_{macro}}$ ) is stored in an accumulation buffer called  $\mathbf{VR}_F^{e_{macro}}$ . It is an accumulation buffer because the residual contributions of  $e_{macro}$  boundaries from other adjacent macro-elements (remote or local to the process) are added to it. This accumulation allows to compute a part of the dot product of the residual F-set vector as a local dot product (appearing in the second loop on the SP element). Their sum is the numerator of  $resi$  to the power of two. But since this local computation is redundant at the boundaries of the macro-elements, a diagonal scaling matrix, applied to the local dot product, is computed once for the entire two-scale loop, so that the boundary terms are counted only once. This scaling matrix is also used, with a zero scaling factor, to remove the Dirichlet DR-set

contributions in the local dot product. This design maintains a semi-independent computation of these accumulation buffers and local dot product which can be treated in parallel (MPI and even with threads as proposed in conclusion). Note that, with the enrichment strategy adopted in section 3.8, as the h-set part of the residual vector that has been eliminated, the rows associated with the SPF nodes (see E) can also be considered null. They are eliminated by using a zero scale factor in the local scalar product for the SPF node dofs. The *resi* value is obtained by dividing the computed numerator by  $\|\mathbf{B}_r\|$  term given as argument to the procedure.

## F.6 COMPUTE\_B\_NORM

The COMPUTE\_B\_NORM procedure (algorithm F.7) provides the term  $\|\mathbf{B}_r\|$  from the vectors  $\mathbf{B}_g^{tmp}$  and  $\mathbf{B}_F$  containing the Neumann boundary condition and volume loading related to the NSP and SP elements respectively. It uses an algorithm very similar to that of F.6 in that the scalar product of vector  $\mathbf{B}_r$  by itself is transformed into a sum of local dot products. The scalar product of  $\mathbf{B}_g^{tmp}$  initializes the sum of the local scalar products of  $\mathbf{B}_r$ . The same diagonal scaling matrix as in F.6, is applied to the local dot product to correct for the redundant contribution to the macro-element boundaries.

**Algorithm F.6** Two-scale algorithm: compute residual value. Return  $\frac{\|\mathbf{A}_{rr} \cdot \mathbf{u}_r - \mathbf{B}_r\|}{\|\mathbf{B}_r\|}$

---

```

procedure COMPUTE_RESIDUAL( $\mathbf{u}_F$ ,  $\mathbf{A}_{FF}$ ,  $\mathbf{B}_F$ ,  $\|\mathbf{B}_r\|$ )
   $resi \leftarrow 0$ 
  for  $e_{macro} \in SP$  do
     $\mathbf{V}_F^{e_{macro}} \leftarrow \mathbf{A}_{FF}^{e_{macro}} \cdot \mathbf{u}_F^{e_{macro}} - \mathbf{B}_F^{e_{macro}}$ 
     $\mathbf{VR}_F^{e_{macro}} \leftarrow \mathbf{VR}_F^{e_{macro}} + \mathbf{V}_F^{e_{macro}}$ 
    for  $e_{adj} \in e_{macro}$  Adjacency do
       $\mathbf{VR}_F^{e_{adj}} \leftarrow \mathbf{VR}_F^{e_{adj}} + \mathbf{V}_F^{e_{macro} \cap e_{adj}}$ 
    end for
  end for
  for  $e_{macro} \in SP$  do
     $\mathbf{V}_F^{e_{macro}} \leftarrow \text{scaled } \mathbf{VR}_F^{e_{macro}}$ 
     $resi \leftarrow resi + \mathbf{V}_F^{e_{macro}} \cdot \mathbf{VR}_F^{e_{macro}}$ 
  end for
  reduce  $resi$  on all processes
   $resi \leftarrow \sqrt{resi} / \|\mathbf{B}_r\|$ 
  return  $resi$ 
end procedure

```

---

**Algorithm F.7** Two-scale algorithm: compute  $\|\mathbf{B}_r\|$

---

```

procedure COMPUTE_B_NORM( $\mathbf{B}_g^{tmp}$ ,  $\mathbf{B}_F$ )
   $\|\mathbf{B}_r\| \leftarrow \mathbf{B}_g^{tmp} \cdot \mathbf{B}_g^{tmp}$ 
  for  $e_{macro} \in SP$  do
     $\mathbf{VR}_F^{e_{macro}} \leftarrow \mathbf{VR}_F^{e_{macro}} + \mathbf{B}_F^{e_{macro}}$ 
    for  $e_{adj} \in e_{macro}$  Adjacency do
       $\mathbf{VR}_F^{e_{adj}} \leftarrow \mathbf{VR}_F^{e_{adj}} + \mathbf{B}_F^{e_{macro} \cap e_{adj}}$ 
    end for
  end for
  for  $e_{macro} \in SP$  do
     $\mathbf{V}_F^{e_{macro}} \leftarrow \text{scaled } \mathbf{VR}_F^{e_{macro}}$ 
     $\|\mathbf{B}_r\| \leftarrow \|\mathbf{B}_r\| + \mathbf{V}_F^{e_{macro}} \cdot \mathbf{VR}_F^{e_{macro}}$ 
  end for
  reduce  $\|\mathbf{B}_r\|$  on all processes
   $\|\mathbf{B}_r\| \leftarrow \sqrt{\|\mathbf{B}_r\|}$ 
  return  $\|\mathbf{B}_r\|$ 
end procedure

```

---

## G Patch cost estimate

In the example of the cube, we have 4 types of patches depending on whether the enriched dof is on the corners, edges, faces or volumes of the cube. Following the octree refinement strategy, for a coarse level  $L_c$  and a final level  $L$  ( $L_c \leq L$ ), the numbers of these patches and their number of dofs are given by the following:

$$nbpatch_{corner}(L_c) = 8 \quad (57a)$$

$$nbpatch_{edge}(L_c) = 12(2^{L_c} - 1) \quad (57b)$$

$$nbpatch_{face}(L_c) = 6(2^{L_c} - 1)^2 \quad (57c)$$

$$nbpatch_{vol}(L_c) = (2^{L_c} - 1)^3 \quad (57d)$$

$$nbdofs_{corner}(L_c, L) = 3(2^{L-L_c} + 1)^3 \quad (58a)$$

$$nbdofs_{edge}(L_c, L) = 3(2(2^{L-L_c} + 1)^3 - (2^{L-L_c} + 1)^2) \quad (58b)$$

$$nbdofs_{face}(L_c, L) = 3(4(2^{L-L_c} + 1)^3 - 4(2^{L-L_c} + 1)^2 + (2^{L-L_c} + 1)) \quad (58c)$$

$$nbdofs_{vol}(L_c, L) = 3(8(2^{L-L_c} + 1)^3 - 12(2^{L-L_c} + 1)^2 + 6(2^{L-L_c} + 1) - 1) \quad (58d)$$

Solving a patch with  $N_d$  dofs and a sparse ratio  $SR_p$ , for  $N_L$  iterations using (31) can be expressed as

$$cost_{1\_patch}(N_d, N_L, SR_p) = count_{fact}(N_d, SR_p) + NL \times count_{bf}(N_d, SR) \quad (59)$$

since only one factorization is performed and a backward/forward resolution is done at each two-scale iteration.

The final cost for all patches using (57, 58, 59) will be the following:

$$\begin{aligned} cost_{patch}(L_c, L, N_L, SR_p) = & nbpatch_{corner}(L_c) \times cost_{1\_patch}(nbdo_{fs_{corner}}(L_c, L), N_L, SR_p) + \\ & nbpatch_{edge}(L_c) \times cost_{1\_patch}(nbdo_{fs_{edge}}(L_c, L), N_L, SR_p) + \\ & nbpatch_{face}(L_c) \times cost_{1\_patch}(nbdo_{fs_{face}}(L_c, L), N_L, SR_p) + \\ & nbpatch_{vol}(L_c) \times cost_{1\_patch}(nbdo_{fs_{vol}}(L_c, L), N_L, SR_p) \end{aligned} \quad (60)$$

## H Static scheduling

The scheduling algorithm, formalized in the algorithms H.8, H.9 and H.10, consists in arbitrarily selecting a vertex for  $\mathcal{S}$  by ascending order of process.

**Algorithm H.8** Sequencing algorithm: Let  $\mathcal{P}$  be the set of process identifiers (starting at 0) and  $nbpid = card(\mathcal{P})$ . This algorithm is executed on each process  $pid \in \mathcal{P}$  containing patches either local (entirely defined in  $pid$ ) or distributed (on  $pid$  and other processes). In this algorithm,  $nbs$  is the maximum number of sequences for all processes in  $\mathcal{P}$ ,  $nbe$  is the maximum number of enlarged sequences for all processes in  $\mathcal{P}$ ,  $mxwg$  is the maximum weight of all distributed patches of all process with an identifier greater than  $pid$  (given by the algorithm H.11),  $mxwl$  is the maximum weight of all selected patches of all processes with an identifier less than  $pid$ ,  $M$  is a matrix storing per column each  $\mathcal{S}$  as a set of colors for all sequences, and PICK\_FIRST, PICK, COMPUTE\_WG are procedures described respectively in the algorithms H.9, H.10, H.11. See A for other conventions.

---

```

Create  $\mathcal{D}$  and  $\mathcal{L}$  sets of distributed and local patches sorted in decreasing weight order
Create  $\mathcal{D}_o$  and  $\mathcal{L}_o$  empty sets that will store, in sequence ordering, distributed and local patches
Create color vector col of size  $nbpid - pid$ 
 $nbs \leftarrow card(\mathcal{D})$ 
 $nbs \leftarrow \max_{i \in \mathcal{P}} nbs_i$ 
 $sid \leftarrow 1$ 
 $nbe \leftarrow nbs$ 
repeat
   $nbs \leftarrow nbe$ 
  while  $sid \leq nbs$  do
     $mxwg \leftarrow COMPUTE\_WG(\mathcal{D}, pid)$ 
    if  $pid = 0$  then
       $(mxwl, \mathcal{D}, \mathcal{L}, \mathcal{D}_o, \mathcal{L}_o, \mathbf{col}) \leftarrow PICK\_FIRST(\mathcal{D}, \mathcal{L}, \mathcal{D}_o, \mathcal{L}_o, \mathbf{col}, pid, mxwg)$ 
    end if
    if  $pid > 0$  then
      Receive from  $pid - 1$  col and  $mxwl$ 
      if  $\mathbf{col}[0] < 0$  then
         $(mxwl, \mathcal{D}, \mathcal{L}, \mathcal{D}_o, \mathcal{L}_o, \mathbf{col}) \leftarrow PICK(\mathcal{D}, \mathcal{L}, \mathcal{D}_o, \mathcal{L}_o, \mathbf{col}, pid, mxwg, mxwl)$ 
      else
         $patch_s \leftarrow \text{pick in } \mathcal{D} \text{ the patch with identifier} = \mathbf{col}[0]$ 
         $\mathcal{D}_o \leftarrow \mathcal{D}_o \cup patch_s$ 
         $\mathcal{D} \leftarrow \mathcal{D} \setminus patch_s$ 
      end if
    end if
    if  $pid < nbpid - 1$  then
      Send to  $pid + 1$  last  $nbpid - 1 - pid$  components of col and  $mxwl$ 
    end if
    Store col as the new last column of  $M$ 
     $sid \leftarrow sid + 1$ 
  end while
   $nbe \leftarrow nbe + card(\mathcal{D})$ 
   $nbe \leftarrow \max_{i \in \mathcal{P}} nbe_i$ 
until  $nbs < nbe$ 
 $\mathcal{L}_o \leftarrow \mathcal{L}_o \cup \mathcal{L}$ 
Create communicators based on colored sequence of  $M$ 

```

---

**Algorithm H.9** Pick first algorithm: On  $pid = 0$  the choice of the candidate is independent of the choice made in the other processes. First try in  $\mathcal{D}$  then in  $\mathcal{L}$ . If both are empty, this process does not participate in the current sequence. See the algorithm H.8 for the notation.

---

```

function PICK_FIRST( $\mathcal{D}, \mathcal{L}, \mathcal{D}_o, \mathcal{L}_o, \mathbf{col}, pid, mxwg$ )
   $\mathbf{col} \leftarrow -1$ 
  if  $\mathcal{D} \neq \emptyset$  then
     $patch_s \leftarrow$  pick out first patch in  $\mathcal{D}$ 
     $\mathcal{A}_s \leftarrow \{n, n \in \mathcal{P}, n \geq pid, n \text{ participate to } patch_s\}$ 
     $\forall l \in \mathcal{A}_s \mathbf{col}[l - pid] \leftarrow patch_s \text{ Identifier}$ 
     $\mathcal{D}_o \leftarrow \mathcal{D}_o \cup patch_s$ 
     $\mathcal{D} \leftarrow \mathcal{D} \setminus patch_s$ 
  else if  $\mathcal{L} \neq \emptyset$  then
     $patch_s \leftarrow$  the first patch  $s$  in  $\mathcal{L}$  with  $weight_s < mxwg$ 
    if  $patch_s = \emptyset$  then
       $patch_s \leftarrow$  pick out last patch in  $\mathcal{L}$ 
    end if
     $\mathbf{col}[0] \leftarrow patch_s \text{ Identifier}$ 
     $\mathcal{L}_o \leftarrow \mathcal{L}_o \cup patch_s$ 
     $\mathcal{L} \leftarrow \mathcal{L} \setminus patch_s$ 
  else
     $patch_s \leftarrow \emptyset$ 
     $\mathbf{col}[0] \leftarrow -1$ 
  end if
   $mxwl \leftarrow weight_{patch_s}$ 
  return  $mxwl, \mathcal{D}, \mathcal{L}, \mathcal{D}_o, \mathcal{L}_o, \mathbf{col}$ 
end function

```

---

**Algorithm H.10** Pick algorithm: First, try in  $\mathcal{D}$ . The choice of the candidate depends on the choices made by all the processes having an identifier  $< pid$ . If no candidate is available, try in  $\mathcal{L}$  respecting a certain condition on the weights. If no candidate is found, this process do not participate in the current sequence. See algorithm H.8 for the notation.

---

```

procedure PICK( $\mathcal{D}, \mathcal{L}, \mathcal{D}_o, \mathcal{L}_o, \mathbf{col}, pid, mxwg, mxwl$ )
   $patch_s \leftarrow \emptyset$ 
  if  $\mathcal{D} \neq \emptyset$  then
     $patch_s \leftarrow$  the first patch  $s$ , if any, in  $\mathcal{D}$  not already selected in  $\mathbf{col}$ 
    if  $patch_s \neq \emptyset$  then
       $\mathcal{A}_s \leftarrow \{n, n \in \mathcal{P}, n \geq pid, n \text{ participate to } patch_s\}$ 
       $\forall l \in \mathcal{A}_s \mathbf{col}[l - pid] \leftarrow patch_s \text{ Identifier}$ 
       $\mathcal{D}_o \leftarrow \mathcal{D}_o \cup patch_s$ 
       $\mathcal{D} \leftarrow \mathcal{D} \setminus patch_s$ 
    end if
  end if
  if  $patch_s = \emptyset$  and  $\mathcal{L} \neq \emptyset$  then
     $crit \leftarrow \max(mxwg, mxwl)$ 
     $patch_s \leftarrow$  the first patch  $s$  in  $\mathcal{L}$  with  $weight_s < crit$ 
    if  $patch_s = \emptyset$  then
       $patch_s \leftarrow$  pick out last patch in  $\mathcal{L}$ 
    end if
     $\mathbf{col}[0] \leftarrow patch_s \text{ identifier}$ 
     $\mathcal{L}_o \leftarrow \mathcal{L}_o \cup patch_s$ 
     $\mathcal{L} \leftarrow \mathcal{L} \setminus patch_s$ 
  else
     $patch_s \leftarrow \emptyset$ 
     $\mathbf{col}[0] \leftarrow -1$ 
  end if
   $mxwl \leftarrow \max(mxwl, weight_{patch_s})$ 
  return  $mxwl, \mathcal{D}, \mathcal{L}, \mathcal{D}_o, \mathcal{L}_o, \mathbf{col}$ 
end procedure

```

---

A color is imposed on the distributed vertex with the highest weight in the lowest process (see figure 6c-j for illustration). In the algorithms H.9 and H.10 this color is the identifier of the selected patch. All its adjacent vertices are frozen to avoid choosing one of them for a new color (it corresponds to fill  $\mathbf{col}$  by a color in algorithm H.9 and H.10). Then, if a vertex remains uncolored and unfrozen, it can be assigned a new color by choosing again the one with the highest weight in the lowest process. It will freeze its own set of vertices. The selection continues until all vertices of the graph have a color or are frozen. The set of colored vertices in  $\mathcal{S}$  can be used directly to create a colored MPI communicator<sup>11</sup>. During selection, the lowest process may not have a distributed vertex available. In this case, a local patch with an appropriate weight is chosen if it is present, otherwise this process will not participate in this sequence.

At each sequence construction, two weights,  $mxwl$  and  $mxwg$  (in the algorithm H.8), are exchanged between the processes respectively, from the lowest identifier to the highest identifier and in reverse direction. The  $mxwg$  weight is the maximum weight of all distributed patches stored in all processes whose process identifier is greater than the current one. It is obtained with the algorithm H.11. It is used directly in the algorithm H.9 when a local patch has to be select (i.e. when all the distributed patches of process 0 have been consumed): the selected local patch must have a weight lower than  $mxwg$  in order not to introduce an imbalance with respect to the weight of the remaining distributed patches on all the other processes that will potentially be selected when the remaining sequence is selected. In the algorithm H.10,  $mxwg$  is used in conjunction with  $mxwl$  which corresponds to the maximum weight of all selected patches in all processes whose identifier is less than the current one. In this algorithm, again when it comes to selecting a local patch, the one whose weight is lower than  $\max(mxwg, mxwl)$  is selected. Thus, the selected local patch will have a cost lower than the worst cost between the already selected patches and those that will be potentially selected.

<sup>11</sup>with MPI.Comm.split

**Algorithm H.11** Compute the maximum weight of all distributed patches of all process whose identifier is greater than  $pid$ . See algorithm H.8 for the notation.

---

**procedure** COMPUTE\_WG( $\mathcal{D}, pid$ )

$mxwg \leftarrow 0$

**if**  $pid < nbpid - 1$  **then**

$mxwg \leftarrow mxwg_{pid+1}$  ▷

**end if**

$mxwg \leftarrow \max(mxwg, \max_{k \in \mathcal{D}}(weight_k))$

**if**  $pid > 0$  **then**

$mxwg_{pid-1} \leftarrow mxwg$  ▷

**end if**

**return**  $mxwg$

**end procedure**

---

## I Computational condition

This work was performed by using HPC resources of the Centrale Nantes Supercomputing Center ICI-CNSC on the cluster Liger (France). It is an INTEL-based computer composed of 252 nodes, with 24 cores (2 x 12 cores Xeon E5-2680v3 at 2.5GHz) per node. Those nodes use a Gpfs network drive for I/O and 128GB of memory. The software used on this platform are eXlibris 2018 (<https://git.gem.ec-nantes.fr/explore>), the GCC 9.2 compiler, OpenMPI 4.03, Mumps 5.4.1, Intel MKL Scalapack, ParMetis 4.0.3, Intel MKL lapack, Intel MKL blas. All Intel software comes from the parallel studio 2020 suites. The integers are compiled with a 4 bytes precision.

## J Micro structure plan definition

The equations of the 64 planes are given below:

$$\begin{aligned}
 &0.8609265 \times x + 0.1956651 \times y + 0.4695963 \times z - 1.748384 = 0 & 0.7195847 \times x + 0.5102510 \times y + 0.4710009 \times z - 2.943090 = 0 \\
 &0.5688037 \times x + 0.06691808 \times y + 0.8197465 \times z - 1.924178 = 0 & 0.1071920 \times x + 0.6029550 \times y + 0.7905410 \times z - 1.271770 = 0 \\
 &0.7416569 \times x + 0.2076639 \times y + 0.6378250 \times z - 2.580966 = 0 & 0.4863807 \times x + 0.4607817 \times y + 0.7423705 \times z - 1.215735 = 0 \\
 &0.2568314 \times x + 0.9470659 \times y + 0.1926236 \times z - 1.424000 = 0 & 0.7151591 \times x + 0.3916348 \times y + 0.5789384 \times z - 1.921521 = 0 \\
 &0.1054744 \times x + 0.9844276 \times y + 0.1406325 \times z - 1.712618 = 0 & 0.6326948 \times x + 0.2613305 \times y + 0.7289744 \times z - 1.181465 = 0 \\
 &0.2716518 \times x + 0.9055059 \times y + 0.3259821 \times z - 1.135105 = 0 & 0.6398444 \times x + 0.3745431 \times y + 0.6710563 \times z - 2.180073 = 0 \\
 &0.5836437 \times x + 0.5275241 \times y + 0.6173154 \times z - 2.052645 = 0 & 0.5684090 \times x + 0.1764028 \times y + 0.8036127 \times z - 1.657721 = 0 \\
 &0.8197048 \times x + 0.1024631 \times y + 0.5635471 \times z - 2.360125 = 0 & 0.1274946 \times x + 0.7139698 \times y + 0.6884709 \times z - 2.370968 = 0 \\
 &0.7305503 \times x + 0.1398926 \times y + 0.6683758 \times z - 0.9220794 = 0 & 0.4882044 \times x + 0.5858453 \times y + 0.6468708 \times z - 0.5461269 = 0 \\
 &0.7241275 \times x + 0.5738369 \times y + 0.3825579 \times z - 2.412523 = 0 & 0.3979635 \times x + 0.3684848 \times y + 0.8401452 \times z - 1.930610 = 0 \\
 &0.8650248 \times x + 0.1441708 \times y + 0.4805693 \times z - 1.795212 = 0 & 0.8572357 \times x + 0.4653565 \times y + 0.2204320 \times z - 1.902939 = 0 \\
 &0.8669178 \times x + 0.1284323 \times y + 0.4816210 \times z - 2.635038 = 0 & 0.1543033 \times x + 0.7715167 \times y + 0.6172134 \times z - 1.961483 = 0 \\
 &0.4793697 \times x + 0.7989495 \times y + 0.3631589 \times z - 1.759905 = 0 & 0.1659080 \times x + 0.2156804 \times y + 0.9622663 \times z - 0.6748800 = 0 \\
 &0.2468854 \times x + 0.7715167 \times y + 0.5863527 \times z - 0.6423204 = 0 & 0.5649452 \times x + 0.6013933 \times y + 0.5649452 \times z - 1.464101 = 0 \\
 &0.4231527 \times x + 0.8711968 \times y + 0.2489134 \times z - 1.657172 = 0 & 0.6388813 \times x + 0.5525460 \times y + 0.5352789 \times z - 1.462725 = 0 \\
 &0.6333450 \times x + 0.4446890 \times y + 0.6333450 \times z - 2.730715 = 0 & 0.2433962 \times x + 0.2920754 \times y + 0.9249055 \times z - 2.773892 = 0 \\
 &0.3298492 \times x + 0.7985822 \times y + 0.5034540 \times z - 2.098559 = 0 & 0.1632993 \times x + 0.4082483 \times y + 0.8981462 \times z - 2.001109 = 0 \\
 &0.5423839 \times x + 0.6693248 \times y + 0.5077637 \times z - 0.9228155 = 0 & 0.6018227 \times x + 0.5249942 \times y + 0.6018227 \times z - 1.695434 = 0 \\
 &0.9093977 \times x + 0.3247849 \times y + 0.2598279 \times z - 2.058806 = 0 & 0.8230470 \times x + 0.5534282 \times y + 0.1277142 \times z - 0.7484869 = 0 \\
 &0.4433384 \times x + 0.1313595 \times y + 0.8866768 \times z - 0.8443746 = 0 & 0.6734445 \times x + 0.6884099 \times y + 0.2693778 \times z - 1.324568 = 0 \\
 &0.2972254 \times x + 0.9145396 \times y + 0.2743619 \times z - 2.464607 = 0 & 0.7218661 \times x + 0.3925938 \times y + 0.5698943 \times z - 2.207026 = 0 \\
 &0.5392394 \times x + 0.6564654 \times y + 0.5275168 \times z - 2.088212 = 0 & 0.3743731 \times x + 0.06606583 \times y + 0.9249217 \times z - 1.333261 = 0 \\
 &0.1427762 \times x + 0.1665723 \times y + 0.9756376 \times z - 0.5186730 = 0 & 0.4939317 \times x + 0.2798946 \times y + 0.8232196 \times z - 1.744109 = 0 \\
 &0.7648147 \times x + 0.07114555 \times y + 0.6403100 \times z - 1.913092 = 0 & 0.8026276 \times x + 0.2390806 \times y + 0.5464699 \times z - 2.138411 = 0 \\
 &0.7220829 \times x + 0.6804243 \times y + 0.1249759 \times z - 1.493591 = 0 & 0.5806682 \times x + 0.5806682 \times y + 0.5706566 \times z - 1.237695 = 0 \\
 &0.8945864 \times x + 0.4388537 \times y + 0.08439495 \times z - 1.095704 = 0 & 0.3212124 \times x + 0.4534764 \times y + 0.8313734 \times z - 1.009433 = 0 \\
 &0.9747546 \times x + 0.05415304 \times y + 0.2166121 \times z - 1.855889 = 0 & 0.5572679 \times x + 0.6868651 \times y + 0.4665499 \times z - 2.181626 = 0 \\
 &0.4943023 \times x + 0.8687737 \times y + 0.02995771 \times z - 0.7418343 = 0 & 0.4652615 \times x + 0.6203487 \times y + 0.6314263 \times z - 1.781062 = 0 \\
 &0.3647265 \times x + 0.4103173 \times y + 0.8358315 \times z - 0.9762100 = 0 & 0.5807795 \times x + 0.5915347 \times y + 0.5592691 \times z - 1.467443 = 0 \\
 &0.9473874 \times x + 0.2368468 \times y + 0.2153153 \times z - 1.995499 = 0 & 0.9486833 \times x + 0.3162278 \times y - 1.061239 = 0 \\
 &0.8602915 \times y + 0.5098024 \times z - 0.3024251 = 0 & 0.9363292 \times x + 0.3511234 \times z - 0.9363292 = 0 \\
 &0.9805807 \times x + 0.1961161 \times z - 1.668649 = 0 & 0.1240347 \times y + 0.9922779 \times z - 0.9292094 = 0
 \end{aligned}$$



## K Pull-out damage computation

The damage field is computed using level-set technologies where the closest distance to the surfaces given by (61) is interpreted, after scaling, as a damage between  $[0, 1]$ . The conical envelope where the damage is calculated (non-zero) is defined by the surface given by the following series of equations:

$$\begin{aligned} (x^2 + z^2) \cdot (\cos \theta)^2 - (y - o_1)^2 (\sin \theta)^2 &= 0 \\ (x^2 + z^2) \cdot (\cos \theta)^2 - (y - o_2)^2 (\sin \theta)^2 &= 0 \\ y + 469.00 &= 0 \\ y - h &= 0 \end{aligned} \quad (61)$$

with

- $\theta = 35^\circ$  is the angle at the apex between the axes  $\vec{e}_y$  and the generating line of the lateral surface.
- $o_1 = -545.08$  and  $o_2 = -531.31$  are  $y$  coordinates of the two apices.
- $h$  is the parameter that controls the stage of disk damage.

The envelope of the conic is then any point  $P$  such that:

$$P(x, y, z) \in \text{conic envelope if } \begin{cases} (x^2 + z^2) \cdot (\cos \theta)^2 < (y - o_1)^2 (\sin \theta)^2 \\ (x^2 + z^2) \cdot (\cos \theta)^2 > (y - o_2)^2 (\sin \theta)^2 \\ -469. < y \\ y < h \end{cases} \quad (62)$$

Note that using planes to stop the conical envelope is a simple and convenient way to obtain a bounded region of easily adjustable size. But for sure, it gives, a completely unrealistic shape of the damage front.

## L Domain decomposition resolution algorithm

The domain decomposition method used, given by the algorithm L.12, is a distributed non-overlapping Schur complement method. Each process holds a domain that is condensed on the process boundary (using the incomplete  $LDL'$  MUMPS factorization). The global boundary problem (i.e. the global Schur complement problem) is solved with a distributed preconditionned (block Jacobi) conjugate gradient given by the algorithm L.13. This distributed version of the conjugate gradient works only with local contributions and communicates mainly when computing the scalar product. The block Jacobi preconditioner simply uses the factorization of the global boundary matrix diagonal block owned by the current process. For a given process, this diagonal block is arbitrary chosen as its local boundary dofs, excluding all dofs present in any process whose identifier is less than that of the current process. Communication only occurs at the time of the construction of the diagonal block, when all the contributions of the other processes are added to the process that owns the block. The factorization of this block is then local to each process. This arbitrary choice, easy to implement, induces that some processes (at least the last one) may not have a diagonal block to treat, which induces some imbalance in the preconditioning task. Note that this choice ensures that the diagonal block can always be factorized as long as the global matrix is not ill-conditioned.

**Algorithm L.12** Block Jacobi preconditionned iterative parallel domain decomposition algorithm: The CONJGRAD procedure is given in the algorithm L.13

---

```

 $S_{bb} \leftarrow A_{bb} - A_{bl} \cdot A_{ll}^{-1} \cdot A_{lb}$ 
 $B_b \leftarrow B_b - A_{bl} \cdot A_{ll}^{-1} \cdot B_l$ 
 $M_{jj} \leftarrow \bigcup_{\forall p \in \mathcal{P} \text{ with } t_p = b_p \cap j \neq \emptyset} S_{t_p t_p}$ 
Factorize  $M_{jj}$  to form the block Jacobi preconditionner
initialize a null vector  $X_s^0$  (or use a previously computed one)
 $(X_s, crit) \leftarrow \text{CONJGRAD}(X_s^0, S_{bb}, B_b, M_{jj}^{-1}, \epsilon)$ 
 $X_b \leftarrow X_{s \cap b}$ 
 $X_l \leftarrow A_{ll}^{-1} \cdot (B_l - A_{lb} \cdot X_b)$ 

```

---

**Algorithm L.13** Parallel conjugate gradient algorithm.

---

```

procedure CONJGRAD( $X_s^0, S_{bb}, B_b, M_{jj}^{-1}, \epsilon$ )
 $X_s \leftarrow X_s^0$ 
 $R_s \leftarrow B_b$ 
 $stop \leftarrow R_s \cdot R_s \times \epsilon^2$ 
 $SP_s \leftarrow S_{bb} \cdot X_{s \cap b}$ 
 $R_s \leftarrow R_s - SP_s$ 
 $Z_s \leftarrow M_{jj}^{-1} \cdot R_{s \cap j}$ 
 $res_o \leftarrow R_s \cdot Z_s$ 
 $P_s \leftarrow Z_s$ 
 $alt \leftarrow 0$ 
repeat
 $res_n \leftarrow res_o$ 
 $SP_s \leftarrow S_{bb} \cdot P_{s \cap b}$ 
 $\alpha \leftarrow \frac{res_n}{P_s \cdot SP_s}$ 
 $X_s \leftarrow X_s + \alpha \times P_s$ 
 $R_s \leftarrow R_s - \alpha \times SP_s$ 
 $crit^2 \leftarrow R_s \cdot R_s$ 
if  $crit^2 \geq stop$  then
 $Z_s \leftarrow M_{jj}^{-1} \cdot R_{s \cap j}$ 
 $res_o \leftarrow R_s \cdot Z_s$ 
 $\beta \leftarrow \frac{res_o}{res_n}$ 
 $P_s \leftarrow Z_s + \beta \times P_s$ 
 $iter \leftarrow iter + 1$ 
else
 $alt \leftarrow 1$ 
end if
until  $alt = 1$  or  $iter > iter_{max}$ 
 $crit \leftarrow \epsilon \cdot \sqrt{\frac{crit^2}{stop}}$ 
return  $X_s, crit$ 
end procedure

```

---

In the algorithm L.12 and L.13 let  $\mathcal{P}$  be the set of process identifiers (starting at 0) and  $nbpid = \text{card}(\mathcal{P})$ . These algorithms are executed on each process  $pid \in \mathcal{P}$  with:

- $K$  the set of dofs of the domain held by the process  $pid$ ,  $K = I \cup b$ ,  $I \cap b = \emptyset$
- $I$  the set of dofs eliminated by condensation in the  $pid$  process
- $b$  the set of boundary dofs of the domain  $pid$  (i.e. the Schur complement dofs)
- $s$  the set of all domain boundary dofs,  $s = \bigcup_{p \in \mathcal{P}} b_p$
- $j$  the set of boundary dofs owned by the  $pid$  process:  $j = b \setminus \left( \bigcup_{p=0, pid-1} b_p \right)$

The following applies for these sets:

- $\forall p \in \mathcal{P}$  and  $\forall q \in \mathcal{P}, p \neq q$  then  $j_p \cap j_q = \emptyset$
- $\forall p \in \mathcal{P}$  and  $\forall q \in \mathcal{P}, p \neq q$  then  $b_p \cap b_q \neq \emptyset$  if  $p$  and  $q$  are connected by at least one mesh node
- for  $pid = 0$   $j = b$
- for  $pid = nbid - 1$   $j = \emptyset$
- $j$  can also be  $\emptyset$  for any process  $p \in \mathcal{P} \setminus (nbpid - 1)$  if the domain  $p$  is surrounded by domains of lower process identifier

## M Mumps block low-rank resolution

The block low-rank (BLR) feature has been introduced in Mumps based on [1]. We choose to activated it with the automatic choice of the BLR option by the library (ICNTL(35)=1 see Mumps 5.4.1 Users' guide ). The BLR factor-

ization variant is the default (ICNTL(36)=0, UFSC variant). The dropping parameter used during BLR compression (CNTL(7)), is chosen to be identical to residual threshold  $\varepsilon$  of the algorithms 1 and L.12. This choice is guided by the fact that the dropping factor and residual error are expected to be strongly related, as shown in [15]. To enforce the condition on the residual error, the BLR resolution is followed by a parallel preconditioned conjugate gradient resolution (algorithm L.13) using both the factorization (as a preconditioner) and the solution (as a starting point) of the low-rank resolution (algorithm M.14). This second resolution is supposed to iterate very little to just force the

---

**Algorithm M.14** Block low-rank algorithm: the CONJGRAD procedure is given in the algorithm L.13. Here  $\tilde{\cdot}$  represent the approximate factorization and the solution of the low-rank resolution.

---

$(\tilde{\mathbf{A}}_{rr}^{-1}, \tilde{\mathbf{X}}_r) \leftarrow \text{Mumps BLR resolution of } \mathbf{A}_{rr} \cdot \mathbf{X}_r = \mathbf{B}_r$	▷
$(\mathbf{X}_r, \text{crit}) \leftarrow \text{CONJGRAD}(\tilde{\mathbf{X}}_r, \mathbf{A}_{rr}, \mathbf{B}_r, \tilde{\mathbf{A}}_{rr}^{-1}, \varepsilon)$	▷

---

residual error to be less than  $\varepsilon$ .